Università Politecnica delle Marche

Doctoral School of Information Engineering

Curriculum: Biomedical, Electronics and Telecommunication Engineering

Modelling and Experimental Characterization of new Microwave Microscopy Techniques for Quantitative Measurements

Advisor:

Prof. Marco Farina

Dissertation of:

Gianluca Fabi

Table of Contents

List of Figures

List of Tables

List of Acronyms

SNR Signal-to-noise ratio.

AFM Atomic Force Microscopy.

CPW Coplanar waveguide.

EFM Electrostatic Force Microscopy.

FeRAM Ferroelectric random access memories.

HfZrO Hafnium Zirconium Oxide.

iSMM inverted Scanning Microwave Microscope.

NFSMM Near-field Scanning Microwave Microscopy.

PFM Piezoresponce Force Microscopy.

PZT lead zirconate titanate.

SMM Scanning Microwave Microscopy.

SNOM Near-field Scanning Optical Microscopy.

SPM Scanning Probe Microscopy.

STM Scanning Tunneling Microscopy.

VNA Vector Network Analyzer.

Abstract

The **Near-field Scanning Microwave Microscopy** (NFSMM or simply SMM) employs the near-field interaction between a probe (source) and a sample to image and characterize materials with atomic resolution. In these systems, the probe excites the sample with microwave frequencies and generates a near-field focused in an extremely small area of the material surface. The microscope measures the local properties of the sample by collecting the response signal originated from this interaction, and the probe dimension mainly determines the resolution, rather than the excitation wavelength. Moreover, the SMM senses not only surface structures, but also electromagnetic properties up to a few micrometres below the sample surface, due to the microwave penetration.

Despite the intriguing features and possible applications of the technique, the SMM presents some **limitations** summarized below:

- limited bandwidth and sensitivity;
- high number of parasitic components;
- hypersensitivity to sample topography; As a consequence, many electromagnetic properties of the sample (beyond the sample topography) can be mostly invisible in SMM data, because the topographic contribution dominates and masks these effects.
- incompatibility with the lossy liquid environment, such as inside saline solutions. This makes the application of SMM in bio-compatible environments highly challenging because live biological material is generally stored inside physiological solutions to survive.

As a consequence, SMM is mainly limited to studies of semiconductor materials

or inorganic surfaces, and it presents many difficulties for the analysis of non-flat and soft samples such as a living biological cell. In this context, the present manuscript illustrates some **innovative technical solutions**, in particular

1. a new technique for the real-time removal of unwanted topographic effects in SMM images. This method enabled us to reveal electromagnetic features of the material, that were hidden in the original data due to the hypersensitivity to sample topography;

2. a new microscope configuration called inverted Scanning Microwave Microscope. This setup has higher bandwidth and reduced parasitic components with respect to existing conventional SMM systems, it enables the local quantitative characterization of sample properties, and it is compatible with the physiological environment used to preserve live biological material.

With this in mind, the present dissertation reports the main experimental results of the developed instruments and methodologies, illustrates their theoretical aspects, and discusses the range of applications of the proposed techniques, including the future directions of the research.

Acknowledgements

This work was supported by the US Army Research Office under Grant W911NF-17-1-0090.

Introduzione

Il **Microscopio a Scansione a Microonde in Campo-vicino** (NFSMM o semplicemente SMM) utilizza l'interazione di campo-vicino tra una sonda (sorgente) ed il campione per l'imaging e la caratterizzazione di materiali con risoluzione atomica. La sonda eccita il campione con un segnale a microonde e genera un campo evanescente focalizzato in un'area estremamente piccola del materiale. Il microscopio misura le proprietà del campione catturando il segnale di risposta generato da questa interazione, con una risoluzione determinata principalmente dalla dimensione della punta piuttosto che dalla lunghezza d'onda di eccitazione. Inoltre l'SMM misura non solo strutture superficiali, ma anche proprietà elettromagnetiche fino ad alcuni micrometri sotto la superfice del campione, grazie alla profondità di penetrazione delle microonde.

Nonostante le interessanti caratteristiche e possibili applicazioni della tecnica, l'SMM presenta alcune **limitazioni** schematizzate di seguito:

- banda e sensibilità limitata;
- elevato numero di elementi parassiti;
- ipersensibilità alla topografia del campione. Di conseguenza, molte proprietà elettromagnetiche del campione (oltre alla topografia) possono essere per la maggior parte invisibili nei dati acquisiti, poichè il contributo della topografia domina e nasconde questi effetti;
- incompatibilità di utilizzo della tecnica in ambienti liquidi con perdite, come ad esempio all'interno di soluzioni saline. Questo rende l'utilizzo della tecnica estremamente complicata per applicazioni bio-compatibili, poichè il materiale biologico vivo è generalmente preservato all'interno di soluzioni fisiologiche per sopravvivere.

Di conseguenza, l'SMM è ampiamente utilizzato nello studio dei materiali semiconduttori o superfici inorganiche, ma presenta molte difficoltà per l'analisi di materiali rugosi e morbidi, come ad esempio cellule biologiche vive. In questo contesto, il presente manoscritto illustra alcune **soluzioni tecniche innovative**, in particolare:

1. una nuova tecnica per la rimozione in tempo reale di effetti topografici indesiderati nelle immagini SMM. Il metodo ci ha permesso di rivelare proprietà elettromagnetiche dei materiali analizzati che erano inizialmente nascoste nei dati originali per via della ipersensibilità alla topografia del campione;

2. una nuova configurazione di microscopia chiamata microscopio a microonde invertito. Questo strumento presenta una banda migliorata e minor effetti parassiti rispetto a sistemi SMM convenzionali, permette l'analisi quantitativa delle proprietà elettromagnetiche dei campioni, ed è compatibile con l'ambiente fisiologico utilizzato per preservare materiale biologico vivo.

In quest'ottica, il presente documento riporta i principali risultati sperimentali delle metodologie e degli strumenti sviluppati, illustra i loro aspetti teorici e descrive il range di applicazioni delle tecniche proposte, inclusa una discussione sulle direzioni future della ricerca.

Ringraziamenti

Questa ricerca è stata finanziata da "US Army Research Office" tramite il finanziamento W911NF-17-1-0090.

Chapter 1

Context, Objectives and the Scanning Microwave Microscopy

Table of contents

Section 1

Introduction, objectives, and organization of the dissertation

Looking at the main historical events in modern microscopy that determined the success of Scanning Probe Microscopy (SPM), the invention of the Scanning Tunnelling Microscope (STM) in 1981 played a cornerstone role [1]. In any SPM, a probe acquires variations of some physical/chemical parameters arising from the interaction between an *ad-hoc* probe and the sample [2]. The STM is based on the tunnelling current between a conductive probe (sharp tip) and a biased sample, providing imaging of conductive samples with atomic resolution. Due to the

paramount importance of their invention, G. Binnig and E. Rohrer were awarded the Nobel Prize in physics in 1986. A few years later Binning *et al.* proposed the Atomic Force Microscope (AFM) [3], based on the interaction force between a probe with a flexible cantilever and a sample; this made possible the analysis of insulating samples also.

Later, the quantitative analysis of material properties with SPMs have become of increasing interest: many other configurations were invented, such as the Near-field Scanning Microwave Microscopy (NFSMM) or simply Scanning Microwave Microscopy (SMM), based on the near-field interaction between a probe and the sample. In the SMM a probe generates an evanescent/near field that locally perturbs small portions of the sample, much smaller than the excitation wavelength. [4–9]. *Ad-hoc* probes, such as a sharp conductive tip, create the localized field, which decays exponentially from the probe itself (source) [10]. The probe acts as an "antenna" of the system to transmit and receive the microwave signal. The radiation locally interacts with the sample (incident signal), and then is collected back (reflected signal) by the same antenna; a Vector Network Analyzer (VNA) [11] generates and records the microwave radiation. In other words, the presence of the sample modifies the reflected wave at the VNA port level, and this signal generally senses both geometrical and electrical properties of the material.

SMM provides advanced sample characterization and possibilities, such as local dielectric permittivity and conductivity study of samples [12, 13], electric field distributions [14], thermometry, [15], and sub-surface analysis [16, 17]. Nowadays, SMMs are mainly employed to semiconductor materials analysis [18, 19], electronic devices study [20, 21], and surface science [22], but the technique is very limited in the biomedical field [23–29]. This mostly because the microscope probe is often incompatible with the presence of lossy saline solutions or live biological material. Notable SMM studies also include the analysis of two-dimensional materials [30–32], superconductive devices [33, 34] and ferroelectric samples [35, 36].

From a practical point of view, common SMMs combine a microwave signal and an AFM/STM with its feedback circuit to keep the probe at a fixed distance from the sample [15, 37, 38], allowing a direct and non-invasive mapping of complex impedance at nanometric resolution. Many modern SMM configurations and systems exist, including commercial versions [7, 39, 40] and the references [41–44] describe the state-of-the-art of SMM instrumentation.

Main limitations of modern Scanning Microwave Microscopes

SMMs generally suffer from the presence of some parasitic components. In AFM-based SMM, classical "hardware" way to reduce these unwanted interactions consists of shielding and/or shrinking the probe cantilever [45–47] to lower the cantilever to ground capacitance [48] or to long and slender probe to elevate the cantilever farther from the sample. However, even if these precautions reduce parasitic elements, their contribution in the SMM data may be the most significant anyway; this especially for samples with tiny intrinsic properties variations, or in liquid solutions typical of a physiological environment, in which the presence of the medium increases the cantilever capacitance. Furthermore, shielded probes are nowadays very limited in the market, available only for specific SMM brands, and generally narrowband.

To remove parasitic interactions, a second approach relies on calibration methods [40, 49–53] and is usually combined with the usage of *ad-hoc* SMM probes and systems. De-embedding procedures enable the full characterization of electrical sample properties [48], but they are generally very complex and subject to errors since they require additional measurements, instrumentation, and post-processing.

Even with those precautions, an unavoidable and generally undesired effect always affects SMM data: the so-called topography crosstalk. This contribution is generated by the vertical movement of the probe, needed to follow the sample surface, that modifies the probe-sample local impedance. In other words, when the sample intrinsic properties (such as electrical conductivity or permittivity) remain the same from one pixel to the other, the SMM signal may change anyway due to the modified probe-ground distance [54]. This means that variations caused by electromagnetic, chemical, mechanical, and geometrical properties are generally mixed in the same image [12]. Thus, the interpretation of SMM data could be tricky and counterintuitive both for raw and calibrated quantities [48].

STM-based SMMs have similar limitations to AFM-based ones; however, the analysis of materials and structures inside a conductive liquid environment is extremely challenging for STM, because the tip immersion creates a direct electrical path between the biased probe and the liquid. As a result, the current between the liquid and probe hides the much lower electron tunnelling contribution, which becomes undetectable. This makes AFM-based techniques preferable in a biocompatible approach.

Objectives of the dissertation

The mentioned open problems motivate the study of new technical solutions addressed during this research, which has the following two main objectives:

- reduce the hypersensitivity to sample topography for the analysis of biological materials as well as rough inorganic samples and surfaces. Ch. 3 addresses this topic and describes a new technique for the real-time removal of topographic effects in microwave images;
- the development of a new microscope configuration compatible with the physiological environment, which has low parasitic components, improved bandwidth, and that provides quantitative electromagnetic analyses of materials, as described in Ch. 4 and 5.

Besides the results obtained during this research, Ch. 1 provides the main idea and concepts behind the SMM, includes a brief historical review, and introduces to the state-of-the-art of the technique. Additionally, Ch. 2 describes the probe-sample motion and its effect on microwave imaging and includes a brief description of the topography crosstalk. Finally, at the end of the document we illustrate the general conclusion of the work, the list of publications related to this dissertation, and Sec. A provides an appendix for a brief review of the microwave networks representation.

Section 2

The Near-field Scanning Microwave Microscope

2.1 History of the technique

Resolution of an ideal, classical optical microscope is limited by diffraction and this limit (known as the Abbe's limit) is on the order of the wavelength λ of the probing radiation [42]. If the the size and properties of the sample vary on a shorter length scale, the electromagnetic response of the material is averaged over higher scales (according to λ), and many details of the sample are lost. This makes extremely challenging to resolve details with sub-wavelength dimensions with far-field systems, *i.e.* when the probe-sample distance is much larger than both λ and the source size, as shown in Fig. 1.1 (a). As a consequence, smaller and smaller wavelengths have been historically used to increase the resolution of those microscopes.

A paradigm shift of the diffraction limit consists of the usage of the near-field, rather than the far-field. In this case, *ad-hoc* sensing elements, commonly called

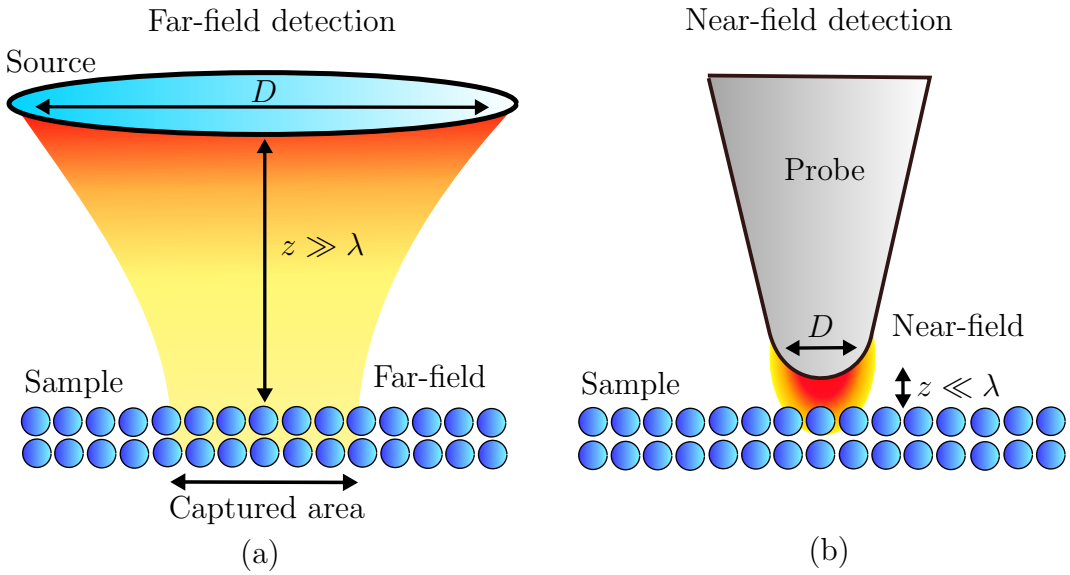

Figure 1.1

(a) In far-field systems, the source focuses the entire area of the sample simultaneously and is positioned at a distance z much higher than the excitation wavelength λ. (b) In the near-field detection, an element with size $D \ll \lambda$ generates the near-field at a distance z much lower than λ; here the system captures the points of the sample one by one, by scanning the probe in the entire sample area.

probes, generate an extremely localized near-field distribution. Near-field probes are created by elements of spatial dimension D positioned at a probe-sample distance z much shorter than the excitation wavelength, as illustrated in Fig. 1.1 (b). In these conditions, the local field distribution interacting with the sample depends mainly on the spatial dimensions D of the source, rather than the excitation wavelength. This way, sample features with spatial size far less than the probing wavelength can be resolved. Historically, Edward H. Synge firstly proposed the implementation of a near-field probe in 1928 [4]. He suggested building the probe by creating a sub-wavelength aperture in an opaque barrier positioned in proximity of the sample to obtain a near-field interaction. In this way, an image could be obtained by scanning the aperture back and forth. However, the technological limitations of that historical period prevented Synge from implementing the concept.

The first experimental works in SMM emerged during the late 1960s and early 1970s. During these years, Bryant and Gunn used a probe-based system for characterizing the local resistivity of a semiconductor crystal obtaining a spatial resolution of ~ 1 mm [5]. They employed a sharp probe integrated with a bridge-based impedance detector, and the electrical length of the probe signal path was chosen equal to an integer number of $\lambda/2$ at the excitation frequency of 450 MHz: this created a

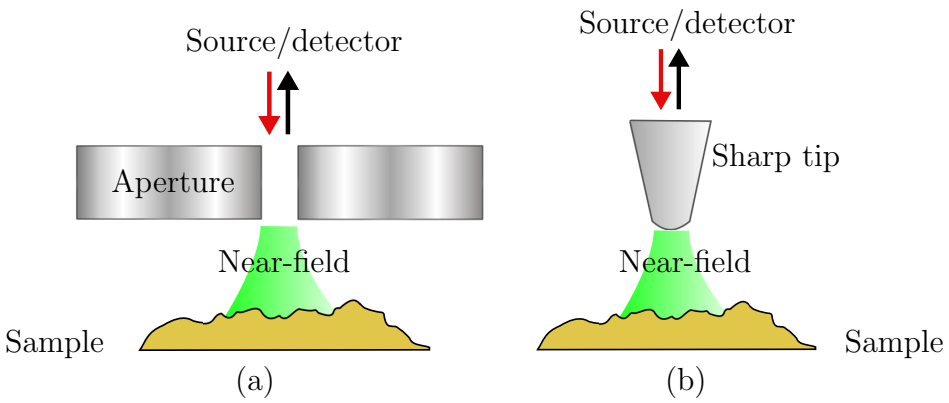

Figure 1.2

(a) In an aperture-based probe, an incident (microwave) radiation hits a sub-wavelength aperture and generates a near-field with a size comparable with the aperture dimension. (b) In an aperture-less probe, a microwave signal travels through a sharp tip that focuses the near-field on the sample. The sample is always positioned in contact or in close proximity to the probe.

resonant circuit enhancing the microscope sensitivity. Later, Ash and Nicholls build an aperture-based system capable to resolve the local permittivity of dielectrics with 0.5 mm spatial resolution [6]. They employed a 10 GHz resonator with a sub-wavelength aperture (1.5 mm in diameter) arranged above a dielectric sample and measured shifts in the quality factor and resonant frequency of the resonator as a function of the local dielectric constant. In more recent years, worldwide scientists reported many kinds of SMM implementations [41,44]. Among them, a sub-family of these systems combine a vacuum STM with the microwave characterization [15,37] reaching microwave resolution down to the atomic scale [8]. Other designs integrate the Atomic Force Microscopy with SMM [39,40], including commercial versions [7,55], enabling the study of fully insulating samples.

2.2 Microwave probes and the near-field concept

Generally, a SMM may employ two types of probes to generate the near-field: aperture-based and aperture-less probes. The Synge's original near-field microscope relied upon an aperture in an opaque screen placed very close to the sample surface [4]. As shown in Fig. 1.2 (a), the aperture has a sub-wavelength dimension and focuses the incident radiation on the sample, generating a near-field distribution with size directly related to the aperture dimension. Later, scientists understood that a microwave signal path terminating in a sharp and conducting point, such as a sharp tip, may be used as an aperture-free probe, generally called aperture-less probes and the most popular nowadays. Again, if the tip has sub-wavelength electrical

dimensions it may be used as a field-focusing element.

The SMM probe is typically connected to a microwave detection system, such as a waveguide used to transfer the radiation from/to a source/detector. During operation, the probe is scanned over the sample surface (either in contact or in close proximity of the sample) and the electromagnetic response is constantly monitored by the detection apparatus. The electromagnetic field generated by the antenna (with size D smaller than the excitation wavelength λ) can be differentiated in three zones with respect to the distance z from the source [10]

- the far-field region with $D \ll \lambda \ll z$;
- the near-field zone, usually defined by $D \ll z \ll \lambda$, but the condition $D \leq z \ll \lambda$ is the interesting one for SMM applications;
- the intermediate field zone comprised between the near and the far-field region.

In the far-field zone, outgoing propagating waves are present and characterized by the in-phase electric and magnetic field (orthogonal to the distance z) [56]. Instead, in the near-field zone, the electric and magnetic field distributions strongly depend on the antenna geometry and the surrounding environment. The fields have a static behaviour while oscillating harmonically and are no more transverse [56]. Near-fields with exponential radial attenuation not related to dissipation mechanisms are usually referred as evanescent fields and are generated by the scattering of electromagnetic radiation [11]. For instance, phenomena such as the total internal reflection in optical waveguides [57–59] or the electromagnetic scattering in cutoff waveguides [11, 60] generate evanescent fields.

Despite the exponential decay (with length scale determined by the characteristic size of the antenna), evanescent fields do not carry energy away. In fact, reactive energy (electric and/or magnetic) is stored in close proximity to the probe by the near-zone. The perturbation of the field due to the presence of a sample causes the variation of the electromagnetic response in the microwave detection system. The probing field acts as a cloud interacting and penetrating the sample with size mainly determined by the probe dimension, as shown in Fig. 1.3 that illustrates the simulated potential distribution of an aperture-less conical probe with a rounded apex. Many solutions have been proposed to create an appropriate localized near-field interaction: probe designs include metal-coated nanowire probes [62], microfabricated coaxial probes [63], atomic force-based probes converted for microwave use [64], or probes sculpted with a focus ion beam [65]. Note also that the sample physical properties

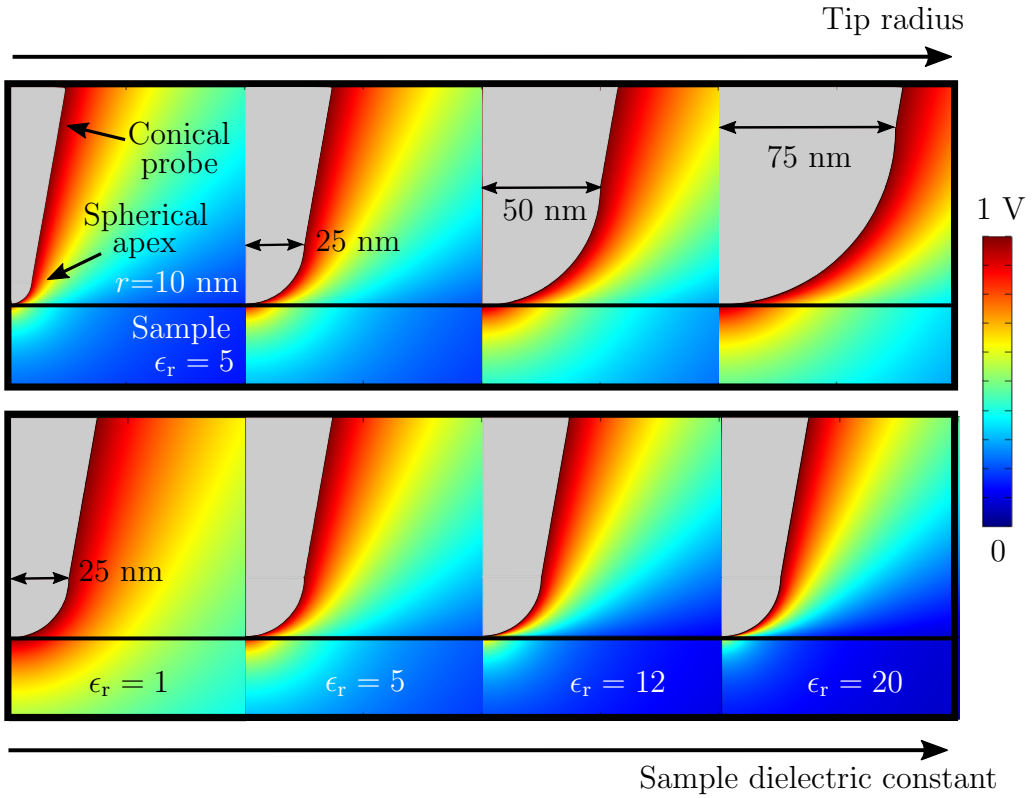

Figure 1.3

COMSOL Multiphysics® [61] simulation of the tip-sample electric potential distribution by varying the tip-radius r and the sample dielectric constant ϵ_r at 4.7 GHz frequency. The numerical model approximates the tip as a conductive cone with a spherical apex, and only half of the geometry is represented. The field focusing effect of the tip decreases with r and increases with ϵ_r.

partially determine the spatial resolution: the high concentration of the field below the tip for high permittivity materials is an example.

In a SMM the tip focuses the field in a single spatial point at a time, corresponding to one pixel of the final image. During a complete scan, the tip travels along the sample surface in a defined area named scan area. First, the tip moves along a line (line scan), and a processing unit records the response of the system. After the line is completed, the probe comes back to the initial point and steps in the subsequent line. The process continues until the microscope records the whole scan area. This image acquisition method is different in far-field systems, in which all points of the sample (within the field) can be imaged simultaneously. On the other hand, in near-field systems single measurements are performed at each pixel of the image, and despite the gain in resolution, they generally require additional instrumentation and longer acquisition time.

Section 3

The operating frequency

3.1 Sensitivity analysis

We call sensitivity the ability of the microscope to sense and differentiate specific sample properties and this property depends on many parameters, primarily from the microscope design and instrumentation, but also on some operating parameters such as the excitation frequency. The sensitivity is commonly quantified as the Signal-to-noise ratio (SNR) of the microscope and generally determines the quality of the measurement. The final SNR is also influenced by many external elements and environmental conditions: they include electromagnetic noise, mechanical vibrations, temperature, parasitic elements, sample properties, and more.

From the design point of view, the SMM instrumentation often includes microwave resonators to enhance the SNR: by integrating a resonant structure [66–68], the SNR is improved by a factor Q; however, the operating frequency is generally limited to a preselected f_0, or in some cases to its harmonic multiples. In a resonant configuration the sample is seen as the load of the microwave resonator: its presence perturbs both Q and f_0, in a quantity that depends on the local sample electromagnetic properties and tip-sample geometry (including their distance). Tunable resonant structures also exist, but with some compromises in terms of the resonator's Q, and consequently SNR.

SMMs without the inclusion of a resonant structure also exist and are generally easy to integrate into an existing SPM, because they only require the inclusion of a microwave signal path with sufficiently low losses, as depicted in Fig. 1.4 (a). Here, microwave cables, connectors, and *ad-hoc* circuitry connect the probe with a microwave source/detector such as a Vector Network Analyzer (VNA) [11], which generates and records the microwave radiation. When a microwave system is integrated into these pre-existing structures, the reflection coefficient, commonly indicated as S_{11} (see Sec. A for a brief review of microwave networks representation) generally depends on frequency. In fact, the many interfaces in the microwave path generate an impedance mismatch: they include cables, connectors, adaptors or even the signal transitions between the waveguide, tip, and load. Fig. 1.4 (b) shows that the sum of these effects generates some sharp minima of the reflection coefficient at certain frequencies. These minima can be seen as the natural resonance frequencies of the system and resemble those of a truly resonant microscope.

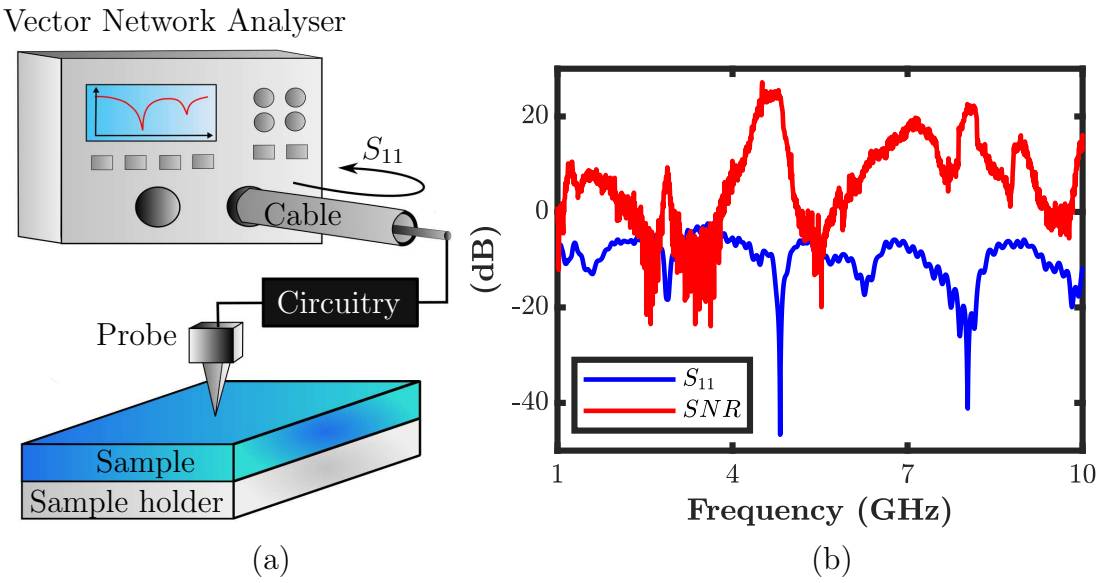

Figure 1.4

(a) Scanning Microwave Microscope scheme: a Vector Network Analyser (VNA) injects the microwave signal through a coaxial cable coupled with the probe. When the signal reaches the sample is reflected to the VNA (S_{11}), bringing some information on sample properties. (b) Example of a microscope complex Signal-to-noise ratio (SNR) in the band between 1 and 10 GHz employing a 12Pt400A Rocky Mountain Nanotechnology [64] atomic-force tip. The optimum sensitivity exceeds 20 dB in a specific frequency band corresponding to a reflection coefficient (S_{11}) minimum around 4.8 GHz.

In non-resonant structures, the minima occur at frequencies at which the microwave circuit is well-matched to the source impedance and is not a real resonance. In operating conditions, *i.e.* when performing the scan, any variation of the local sample impedance will provoke a change in the shape and value of the local reflection minimum. The amount of this variation will depend on the sensitivity of the microscope to the sample local impedance. Generally, multiple minima of reflection coefficient may be used as operating frequencies [69] but the sensitivity may significantly vary between them. Non-resonant microscopes have similar features, working principle, and limitations of resonant SMMs, including the generally narrowband behaviour.

Practically speaking, the microscope user must select the frequency f_0 (or the frequency band for broadband measurements) that maximizes the SNR to capture data without excessive noise. A practical approach to choose a suitable frequency point consists of measuring the SNR defined as

$$SNR = 20 \log \left[\frac{\overline{S_{11}(z=0)} - \overline{S_{11}(z=3\ \mu\text{m})}}{\sigma[S_{11}(z=0)]} \right] \tag{1.1}$$

expressed in dB, in which $S_{11}(z = 0)$ and $S_{11}(z = 3\ \mu\text{m})$ are measured reflection coefficients with the probe contacting the sample (or very close) and lifted 3 μm in the air, respectively. Each measurement is repeated a certain number of times (such as 500) and arithmetic averaged ($\overline{S_{11}}$) to reduce noise, with σ as the standard deviation. The S_{11} term in Eq. 1.1 refers either to the complex value of the reflection coefficient or to the single amplitude and phase term.

In aperture-less probes (the most interesting type for us), the tip effective radius r indicates the tip features with the lower dimension that directly interacts with the sample, and it generally defines the SMM spatial resolution [41]. However, the tip-sample capacitance should remain sufficiently high to get a good SNR ratio and the tip radius cannot be reduced indefinitely, but arbitrarily increasing r will compromise the spatial resolution. Thus, a trade-off between SNR and spatial resolution exists.

3.2 Some advantages of microwave frequencies

As Fig. 1.5 shows, despite the much longer wavelength λ of microwave frequencies than that of the optical ones, the SMM has many advantages over techniques that employ optical radiations, such as the Near-field Scanning Optical Microscopy (SNOM) [44, 70]. First, SMM is less invasive because the energy of microwave photons is of the order of 10 μeV. On the contrary, optical photons have much greater energy around 1 eV. Optical radiation interaction with materials strongly depends on the wavelength because of mechanisms such as lattice dynamics and quantum phenomena [71], thus optical properties of matter are often hard to get from near-field interactions. On the contrary, microwave radiation interacts with materials in a more classical way [72–75]. This simplifies measurements and data interpretation. Moreover, SMM is generally sensitive to optically opaque materials [76] or to the dielectric permittivity of frequencies relevant to most electronic and biological functions. It also allows spectroscopy over many decades of frequencies from the same microwave source, and broadband SMM is desirable because

- it provides information at relevant frequencies;
- it allows time-gated filtering of unwanted signals through post-measurement data processing [50];
- it enables microwave tomography [16].

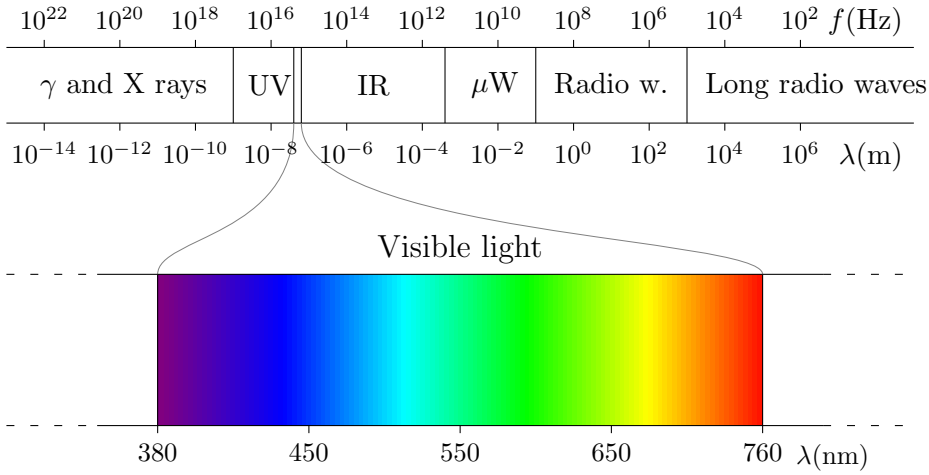

Figure 1.5

Electromagnetic spectrum with indication of frequency f, wavelength $\lambda = c/f$ and corresponding bands. From Planck's radiation law $E = hf$, in which E is the energy of the radiation and h is the Plank's constant, the energy of the microwave radiation corresponds to around 10 μeV. On the other hand, optical photons have an energy of around 1 eV.

Section 4

A circuital view of the microscope

4.1 Microwave representation of a reflection mode microscope

Due to the complex nature of most microwave microscopes, simplified equivalent circuits facilitate the understanding and the study of those systems. They also provide the mathematical foundation of calibration algorithms needed for the quantitative characterization of samples.

In a SMM, generally a VNA port is electrically coupled to the microscope probe through the usage of *ad-hoc* microwave circuitry. In the case of a traditional reflection mode microscope (see again Fig. 1.4), the VNA measures only the reflection coefficient S_{11} and one VNA port is connected. Fig. 1.6 (a) shows a simple block diagram of a traditional SMM. Here, the admittance Y indicates the probe-sample local interaction, meaning the near-field interaction that takes place below an arbitrary reference plane along the probe, as indicated in Fig. 1.6 (b); Y depends on the sample electromagnetic properties as well as on the probe-sample geometry, such as the sample thickness or probe dimensions. The scattering matrix $\overline{\overline{\boldsymbol{S}^{\mathrm{e}}}}$ models all the other effects not strictly related to the probe-sample local interaction, including the presence of lossy cables, connectors, radiating fields, and more. Those quantities do not change during a single measurement and existing error-box correction methods

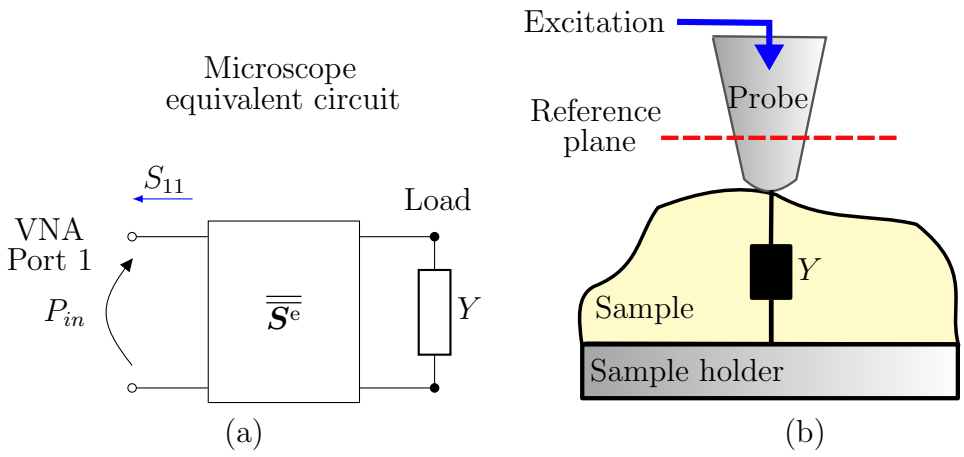

Figure 1.6

(a) Block scheme of a reflection mode Scanning Microwave Microscope. The scattering matrix $\overline{\overline{S}}^{e}$ indicates the error network due to the presence of cables, connectors, and other non-local effects. Y indicates the tip-sample local admittance and models the probe-sample interaction that occurs below an arbitrary reference plane along the probe. (b) Probe-sample geometry with an indication of the reference plane.

can be applied to remove their effects.

4.2 Calibration of measurements

The calibration process indicates the removal of undesired effects due to the additional microwave circuitry of the microscope (cables, connectors, adaptors, etc.) or due to the elements that surround the near-field zone and may influence the response of the system. The calibration also allows us to retrieve the local tip-sample admittance measurement at the nanometric scale, which is the first step to conduct quantitative sample characterizations [49]. Some already existing procedures perform the calibration without using any additional reference sample, and are advantageous because of their ease of use and accuracy: this section will provide the general idea behind these procedures, as well as the general foundation of the calibration algorithm developed for our new microscope configuration of Ch. 4.

The calibration process requires a set of known well-characterized loads, called "standards" [49]. However, the definition of these loads in SMM presents many difficulties, because the microwave probe interacts with the sample as well as with the sample support and whatever is nearby. This means that the insertion of a special calibration sample [39] to obtain the standards is not a trivial issue, because its presence affects the electromagnetic boundary conditions, and even nanometric changes in the boundary have a relevant impact on the measurement. The general idea

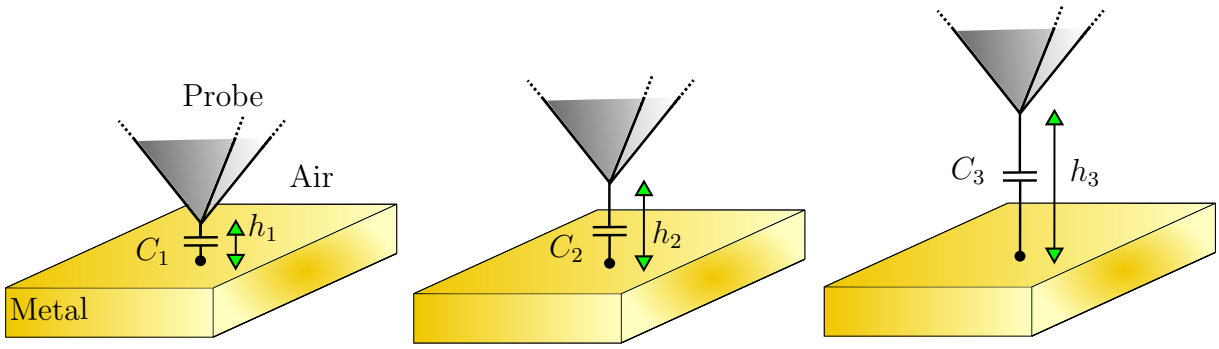

Figure 1.7

Capacitance standards (C_i) and probe-substrate distance quotes (h_i) for the calibration of the Scanning Microwave Microscope.

of [49] is to exploit the distance between the SMM probe and the sample conductive support as a known quantity to generate a set of the known loads, corresponding to the tip-to-ground capacitances. This enables the in-situ SMM calibration without the usage of any calibration sample.

This approach requires the definition of the boundary between the measuring and measured parts or in terms of scattering parameters the reference plane of the port. They respectively indicate what includes the error network of Fig. 1.6 (a), and what is the effect to be measured *i.e.* the informative part of the electromagnetic field situated below the microwave tip. In particular, the "reference plane" of Fig. 1.6 (b) indicates the plane where the probe can be considered to have a specific well defined, geometrical feature, such as when we approximate the tip end as a conductive cone with a spherical apex (see again Fig. 1.3). Different geometrical approximations of the probe are possible, according to the probe used and the degree of accuracy in the representation.

Assumed the error box reciprocal, in a single port measurement three known loads are sufficient to recover the complete matrix. Fig. 1.7 shows that they correspond to the capacitances of the conductive probe at three different distances from a metal plane. Thus, a metallic area of the sample must accessible during the measurement. The precise positioning of the tip-sample distance is generally performed using a distance-following mechanism, *i.e.* by integrating the SMM into existing microscope configurations, such as the Scanning Tunnelling Microscopy or the Atomic Force Microscopy, as detailed in the next chapter.

Chapter 2

The Probe-Sample Motion and its Effect on Microwave Images

Table of contents

Section 1
Introduction

Due to the intrinsic nature of the near-field, the Scanning Microwave Microscope (SMM) provides a non-destructive sample characterization, because it also measures without contacting the probe and the sample. However, to assure a sufficient probe-sample interaction, the sensing element must be kept extremely close to the sample surface. Moreover, SMM senses the local electrical admittance Y of the tip-sample

system that depends both on the electromagnetic and geometrical properties of the probe and sample. This means that the tip-sample distance z is a critical parameter during measurements.

Most common SMMs integrate a distance-following mechanism to maintain a constant value of z while scanning the sample, and a SMM is generally coupled with other Scanning Probe Microscopy techniques, such as the Scanning Tunnelling Microscope (STM) or the Atomic Force Microscope (AFM). These systems employ sharp tips as probes, and aperture-less SMMs can be integrated in existing SPMs by inserting a microwave signal path reaching the probe. For instance, STM uses the quantum mechanical tunnelling of electrons from a metal tip to a conductive sample and is a natural platform to integrate a SMM [15, 37, 49]. Similarly, AFM-based SMM employ special AFM probes converted for microwave use allowing the high frequency characterization of materials [7, 39, 40].

The distance-following mechanism performs an additional important task: obtain topological information of the sample, conventionally called topography image. This is important for the interpretation of SMM data or quantitative analyses [40, 76] because the tip-sample admittance depends on the system geometry itself. Moreover, height-dependent SMM measurements also allow in-situ calibration [49] and sensitivity analysis. In this sense, the present chapter describes the most diffused techniques to control the tip-sample distance in a SMM and describes the main unwanted effects during measurements, such as the hypersensitivity to the sample topography. The removal of this effect was a fundamental topic of our research and will be addressed in Ch. 3, which describes a new methodology to overcome this phenomenon.

Section 2

Scanning tunnelling-based Microwave Microscopes

2.1 Apply the quantum tunnelling in microscopy

Ivar Giaever proposed the basic principle of electron tunnelling in 1960 [77]: a potential difference between two metals separated by a thin insulating film generates a current flow, generally called tunnelling current, due to the ability of electrons to penetrate the potential barrier of the film. Based on this principle, the Scanning Tunneling Microscopy (STM) measures the tunnelling current [78] generated between a metal sharp tip (probe), shown in Fig. 2.1 (a), and a conductive sample when an electrical bias is applied between the two [1]. The STM current is extremely sensitive to small variations of the tip-sample distance [79] and this allows to control

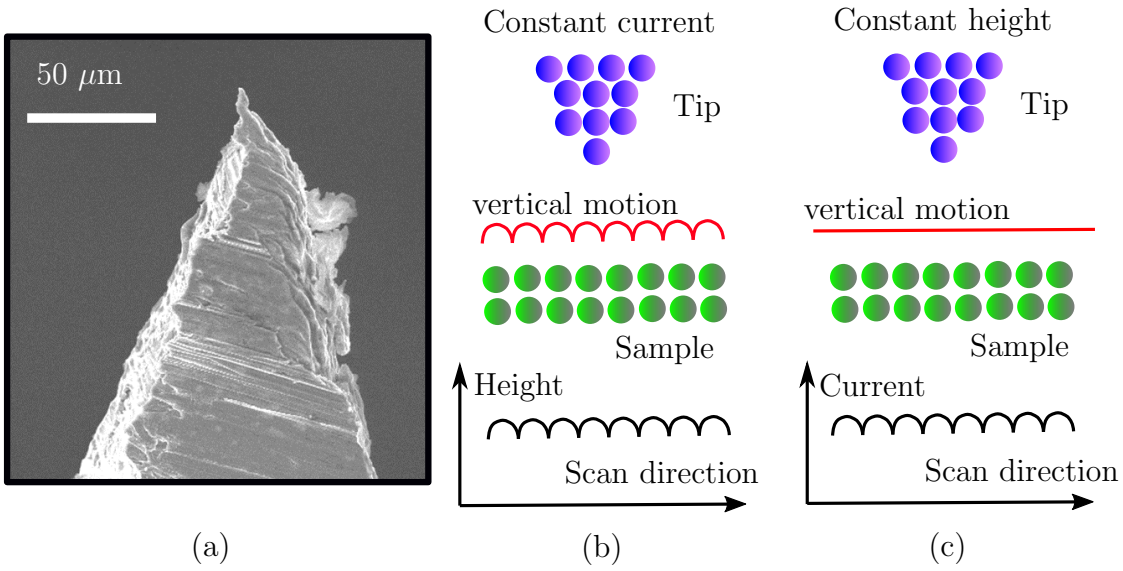

Figure 2.1

(a) Scanning electron microscope image of a Platinum/Iridium Scanning Tunnelling Microscopy (STM) tip made by wire cutting [49]. Operating modes in STM: (b) constant current and (c) constant height mode.

the probe-sample separation with high precision. In particular, the electrons flow exponentially increases with reduced metal separation, and a spacing less than 10 nm allows to measure the current [80]. Additionally, the tunnelling current mainly involves the tip atom that is closest to the sample surface, providing a high lateral resolution down to the atomic scale (highly depending upon tip sharpness, usually made by a platinum or Platinum/Iridium wire to perform in the air). For these reasons, STM is one of the possible methods for being used in the SMM control system to precisely manage the tip-sample separation [15, 37].

Generally, STMs can be used in two operating modes: constant current and constant height mode. In the constant current mode, a feedback circuit continuously adjusts the tip-sample distance to maintain a user-defined current, called setpoint, using piezoelectric actuators. As shown in Fig. 2.1 (b), when the tip scans a sample, an atomic topography variation at the surface changes the tunnelling current due to the variation of the probe-sample distance. The feedback circuit reacts by approaching or retracting the tip (or sample) and brings back the current to the setpoint value. The tip height is mapped by recording the feedback signal as a function of the in-plane position, and this corresponds to the surface topography of the sample (in first approximation, without considering the so-called electronic effects [2]).

In constant height mode instead, the feedback is switched off and the tip scans the

sample at a constant height, as illustrated in Fig. 2.1 (c). Considering a homogeneous sample, surface points with higher height result in an increased tunnelling current due to the reduced tip-sample distance and this provides a map of the sample topography. The data acquisition speed in the constant current mode is advantageous because it is only limited by the current amplifier bandwidth rather than that lower of the feedback loop, but the mode shows several practical issues compared to the constant current mode. First, a fixed height is hard to maintain during a scan over an atomically flat surface, because of effects such as thermal drift, making it preferable for low-temperature measurements. Sample tilt and tip-surface mechanical contacts make the use even more challenging, confining the application to very small and atomically flat surfaces.

2.2 The control system

In an SMM distance-following mechanism such as the STM-based, a control system manages the tip-sample positioning and it also contributes to the final accuracy and speed of the measurement. Fig. 2.2 (a) describes the main block of an SMM control system, also valid for the atomic force-based distance control described in Sec. 3, in which P indicates the physical parameter representing a generic tip-sample interaction mechanism (*e.g.* the tunnelling current in STM). The user selects a reference value of P (set-point), here indicated by P_0 and the feedback system continuously adjusts the value of P to P_0; this if a monotonous and sharp $P(z)$ exists, at least locally, as Fig. 2.2 (b) shows. In other words, the feedback system minimizes the differential signal $\Delta P(t) = P(t) - P_0$, where t represents a certain time instant. To perform this task, ΔP is amplified and sent to a piezoelectric stage that controls z: if the value of P is modified from the set-point, the transducer brings back P to P_0, by keeping ΔP (ideally) equal to zero.

When the tip and sample are far away, to start a measurement the system brings the two elements very close, in an operation commonly called landing. First, a stepper motor with a wide range of motion roughly approaches the two elements; then, piezoelectric transducers closely position the two, by assuring a good near-field interaction between the probe and sample. Piezoelectric materials such as lead zirconate titanate (PZT) change their shape when immersed in an electric field, due to the anisotropic crystal structure (transverse piezoelectric effect) [81]: by applying a control voltage at the terminals of the piezoelectric element, the mutual tip-sample position changes, leading to scanning and positioning operations in the three spatial

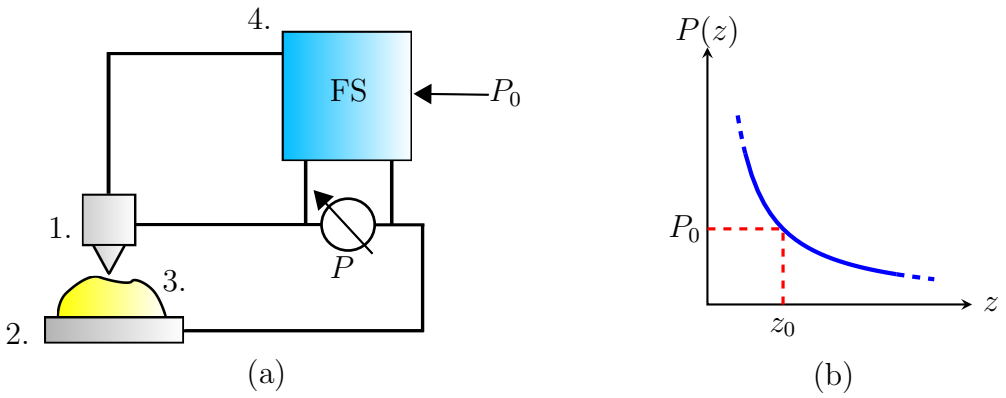

Figure 2.2

Block diagram of the main components of a Scanning Microwave Microscope control system (a). 1. Probe. 2. Piezo actuator. 3. Sample. 4. Feedback system (FS). P indicates the measured tip-sample interaction and P_0 is the user-defined setpoint. (b) $P(z)$ monotonous dependence respect to the tip-sample separation z. The condition $z = z_0$ corresponds to the distance at the setpoint.

dimensions.

2.3 The microwave path

The conductive nature and geometrical properties of STM tips make them directly applicable to SMM systems as aperture-less probes [15, 37, 49]. Usually, a proper integration of the two systems only requires a decoupling circuit for high-frequency signals (SMM) and low-frequency ones (STM) [82]. Fig. 2.3 shows an STM assisted SMM self-made by coupling a commercial Scanning Probe Microscope by NT-MDT (Solver Pro P-47) and a head featuring a high sensitivity current amplifier for STM operation. The STM Pt/Ir probe acts also as the SMM antenna, being capacitively coupled to a Keysight PNA E8361A Vector Network Analyzer (VNA), using a flexible cable. In this way, the system captures a microwave image in terms of reflection coefficient, and a topography image from STM [22].

Due to the intrinsic nature of the distance control mechanism, an STM-based SMM allows studying electrically conductive materials only. Historically, the Atomic Force Microscope (AFM) overcame this limitation with the usage of a force rather than an electric current [3]. Similar to the STM case, AFM-based SMM exists, and the application of the new methodologies and configurations proposed in this research will be presented for AFM-based platforms, despite being fully STM compatible. Thus, the next section presents the AFM technique and discusses its integration in microwave microscopes.

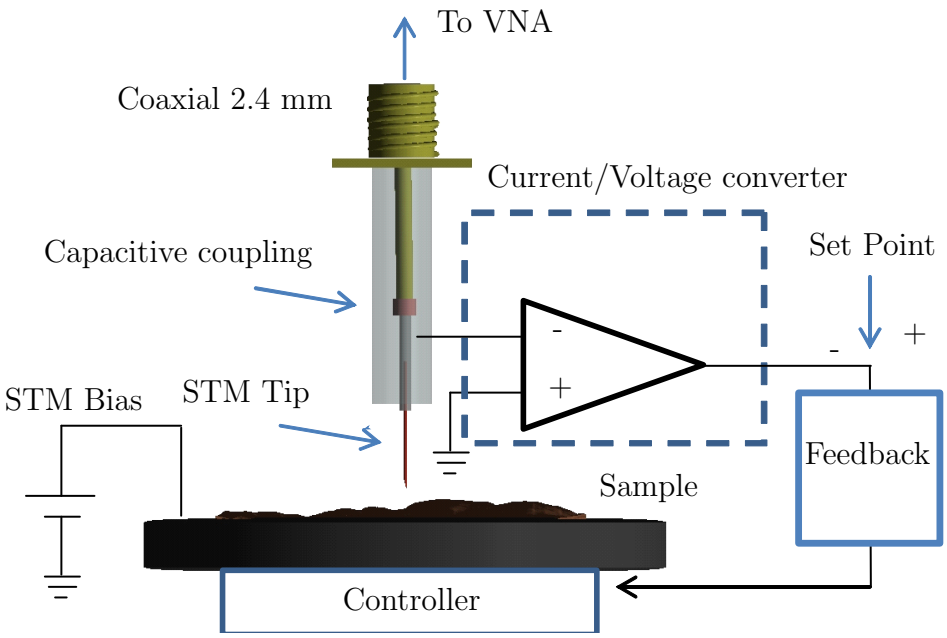

Figure 2.3

Block scheme of a scanning tunnelling-based Microwave Microscope. The Scanning Tunnelling Microscope (STM) controls the tip-sample distance through a feedback system and a controller. The Vector Network Analyser (VNA) injects/detects the microwave signal through a coaxial cable, and a capacitive gap decouples the high and low frequency (STM) signal [82].

Section 3

Atomic force-based Microwave Microscopes

3.1 Working principle of Atomic Force Microscopy

In 1986, Gerd Binnig, Calvin F. Quate and Christopher Herber proposed and implemented the Atomic Force Microscopy (AFM) based on the interacting force between a flexible probe and a sample [3]. Fig. 2.4 illustrates a typical AFM tip-sample geometry, in which an elastic cantilever and a very sharp tip compose the probe [81]. If the tip and sample are sufficiently close to each other, the interactive force between them bends the cantilever and this force is measured by a detection system. In simplified terms, the AFM cantilever behaves as a spring with a spring constant k and has a deflection z proportional to the probe-sample force. Hooke's law relates the force F and the cantilever bending as $F = -kz$, in which the cantilever equilibrium position indicates the zero bending condition. The tip-sample force is evaluated by knowing k and by measuring the cantilever bending.

The system spatial resolution of modern AFMs reaches the atomic scale and

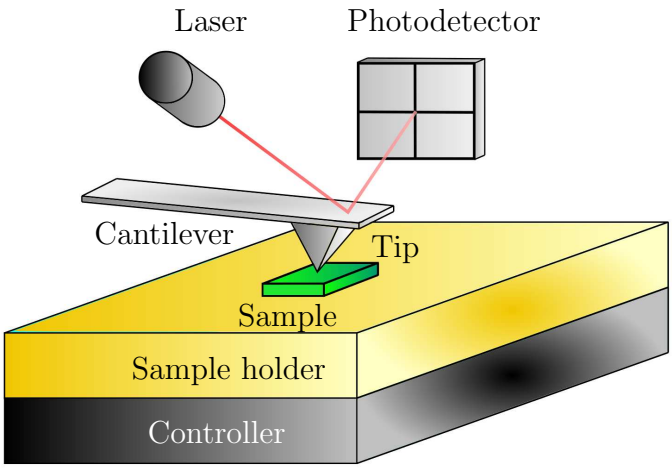

Figure 2.4

(a) Atomic Force Microscope scheme, with an indication of the tip, elastic cantilever, sample, laser-photodetector system, and controller that manages the tip-sample position.

is mainly the product of two factors: the radius of curvature of the tip and the sensitivity of the microscope in detecting the cantilever deviations. Notably, in the original AFM implementation Binning *et al.* employed an STM to measure the AFM cantilever deflection [3], but most modern AFMs integrate an optical system that uses the beam-bounce technique [81]. In this method, a laser spot hits the back surface of the cantilever and the reflected beam points to the centre of a four-quadrant photodiode (see again Fig. 2.4). The cantilever bending causes the shift of the laser spot position on the detector; a cantilever deflection or torsion generates a vertical or lateral shift respectively.

The photodiode output provides an electrical current I proportional to the tip displacement (or to an equivalent physical parameter depending on the operating mode) with respect to the equilibrium position. To maintain the tip-sample distance z to a z_0 preselected value (setpoint), a feedback system keeps I constant by controlling a piezoelectric transducer (scanner), as already described in Sec. 2.2. During the scanning operation, the tip follows the sample surface and the voltage applied on the scanner electrode is recorded as the sample topography.

3.2 Probe-sample interaction mechanism

The total force between the tip and sample surface is composed of long-range and short-range contributions [2]. The van der Waals force belongs to the long-range interactions. This force, here treated as the London dispersion interaction, is a force between atoms/molecules without a permanent dipole moment. It can be seen as

an attracting force between fluctuating electric dipoles spontaneously formed. The van der Waals interaction is isotropic, *i.e.* non-directional, and additive: the atoms in the close proximity of the tip apex play a role in the attractive force, but also those further from the tip contribute in some amount. Ultimately, the sum of all the elementary interactions of tip and sample atoms indicate the total force [81].

Beside long-range forces, the overlap of the tip-sample electrons wave functions of the outermost shell generates short-range interactions. These forces are attractive when the overlap reduces the total energy forming chemical bonds. For instance, between a metal tip and a metal surface, an attractive interaction appears at a low tip-sample distance, similar to a metallic bonding. On the other hand, the repulsion force between the inner electron shells is significant for the tip-sample atoms at closer distances than those in chemical bonds. This interaction is due both to the electrostatic repulsion of the electrons of the closed shells and to the Pauli exclusion principle [2] (two electrons cannot occupy the same state [83, 84]).

The Lennard-Jones potential is a commonly used model potential for the overview of tip-sample surface behaviour and it describes the interaction between two neutral atoms [2]. It includes two terms, describing the attractive (van der Waals) and repulsive interactions, respectively:

$$U_{\mathrm{LJ}} = 4U_0 \left[\left(\frac{z_0}{z} \right)^{12} - \left(\frac{z_0}{z} \right)^{6} \right] \tag{2.1}$$

with U_0 the potential well depth, z the atoms distance, and z_0 the distance in which the potential is zero. The repulsive and attractive terms are proportional to $1/z^{12}$ and $1/z^6$ respectively. Fig. 2.5 displays the behaviour of the Lennard-Jones potential, the attractive and repulsive contributions individually, and the corresponding force $F = -\partial U/\partial z$. The model captures the main features of the probe-surface interaction: it shows a repulsive (positive) force at short distances, a minimum of potential, then an attractive (negative) force at a large distance, and finally a negligible interaction when the tip and sample are far away.

Fig. 2.5 shows that the tip-sample force depends non-monotonously on the tip-sample distance, and in operating conditions, this requires either to use the left or right branch of the curve. In the AFM static mode, a feedback system maintains a constant tip-sample force corresponding to a fixed distance, by modifying the vertical tip position. The recorded point by point tip vertical position corresponds to the surface topography. The contact mode operation indicates measurements carried out

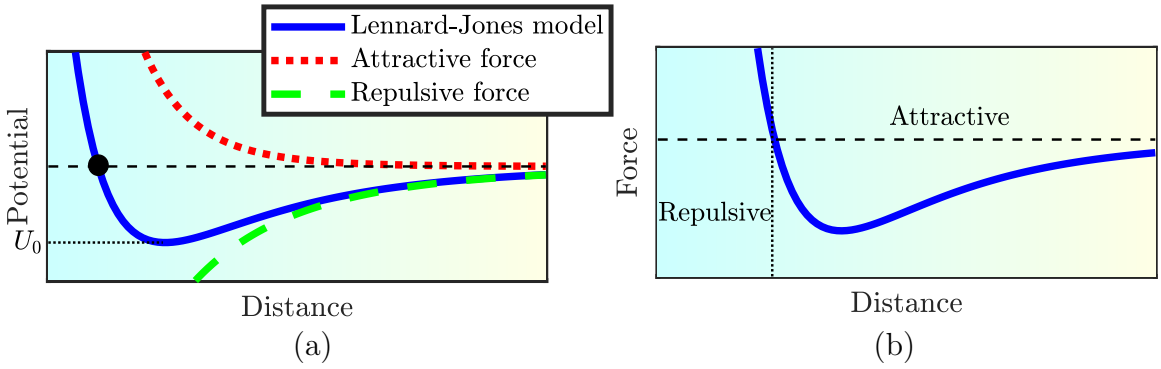

Figure 2.5

(a) The Lennard-Jones potential model that approximates the Atomic Force Microscope tip-sample interaction, with indication of the attractive and repulsive contribution. The distance z_0 indicates the separation at which the potential is zero. (b) Corresponding force $F = -\partial U/\partial z$ with attractive (right) and repulsive (left) interaction region.

in the repulsive force region: the superficial sample atoms are in direct contact with those of the probe apex. This often causes tip or sample breakage and is not always suitable for soft samples such as biological material.

In dynamic or non-contact mode the cantilever is forced to oscillate to a frequency close to its free resonance frequency (free indicates when the probe is far away from the sample). By reducing the tip-sample distance, the tip-sample interaction modifies the cantilever resonance frequency and oscillation amplitude. The AFM optical system detects the amplitude variation and the feedback mechanism uses this signal to regulate the distance. Non-contact mode is particularly useful when imaging soft samples, being less invasive than contact techniques.

3.3 Atomic force-probes for microwave imaging

The integration of a non-resonant SMM into an AFM consists of creating a microwave path from the microwave source/detector to the conductive AFM tip through the use of microwave circuitry [7, 40]. AFM probes converted for SMM use often include solutions to reduce parasitic interactions due to the presence of the cantilever and surrounding elements, such as shielding and/or shrinking the cantilever [45–48] or to long and slender the probe to increase the cantilever-sample distance.

Fig. 2.6 (a) depicts the front side of the commercial Rocky Mountain Nanotechnology 12Pt400A probe, a typical AFM chip for SMM applications. The figure shows the ceramic chip, the platinum tip and cantilever, and the gold pad to couple the probe with the microwave circuitry, and Tab. 2.1 reports the nominal physical parameters of the probe. Fig. 2.6 (b) also illustrates the inner conductor of coaxial

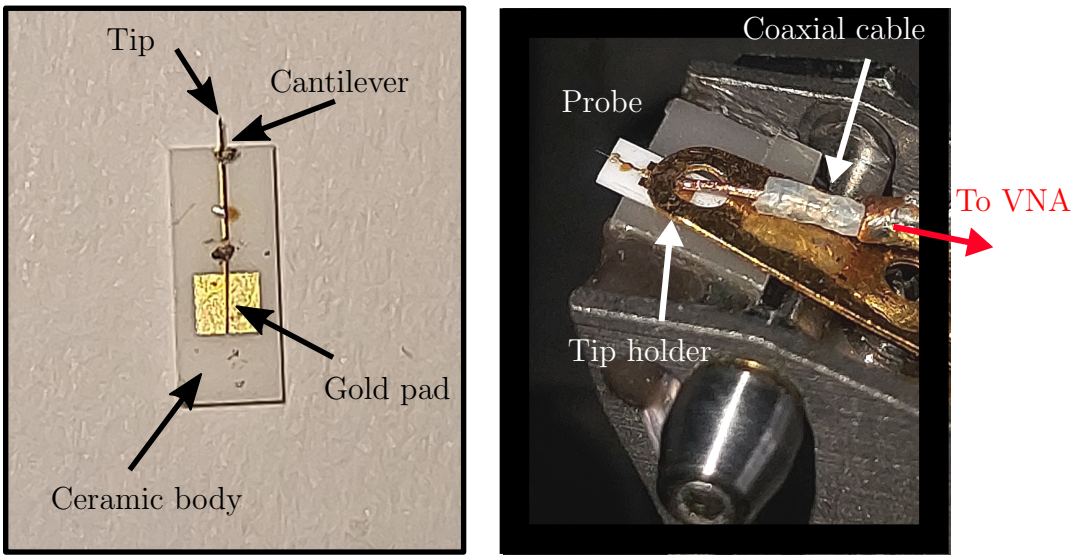

(a) (b)

Figure 2.6

(a) Rocky Mountain Nanotechnology 12Pt400A Atomic Force Microscopy (AFM) tip for contact measurements with a minimum contact force due to the low spring constant. The tip and cantilever are made of platinum and are supported on a standard AFM probe sized ceramic chip, connected to a conductive gold bonding pad with conductive epoxy. The long tip shank length reduces the cantilever parasitic capacitance and couples the microwave excitation into the tip-sample region. (b) Picture of a home-made AFM-based microwave microscope, in which the inner conductor of a coaxial cable contacts the AFM conductive tip for the coupling with a Vectorial Network Analyzer (VNA).

cable, mounted on the AFM head, that couples the probe with a Vector Network Analyzer. This forms a non-resonant SMM that has been used in our research to investigate the ferroelectric structure of a Hafnium Zirconium Oxide sample, as described in Ch. 3.

Table 2.1

Main physical parameters of the 12Pt400A Rocky Mountain Nanotechnology probe depicted in Fig. 2.6. The typical cone angle near the tip apex is around $10 \div 20°$ [17, 18]. For specific analyses, the tip radius is a fitting parameter in electromagnetic models of the SMM, because it may significantly vary from the nominal value and it generally changes with use.

Probe parameter	Nominal value
Tip shank length	80 μm
Cantilever length	400 μm
Cantilever width	60 μm
Spring constant	0.3 N/m
Oscillation frequency	4.5 kHz
Tip radius	less than 20 nm

As a final remark, note that the type of distance-following mechanism chosen for the SMM operation contributes in some amount to the microscope performance: it determines the microwave antenna properties, has an important role in the spatial resolution, and defines the range of applications in terms of sample characteristics. For instance, the analysis of photoconductive samples with an AFM could be problematic: they may be sensitive to the optical illumination of the AFM optical detection system [42]; on the other hand, as already mentioned an STM-based SMM cannot be employed for the study of fully insulating samples.

Section 4

Causes of noise and parasitic effects

4.1 Mechanical instabilities and thermal effects

In a SMM, many unwanted phenomena limit the positioning performance of the control system: they include the non-linearity of the tube scanner, hysteresis of the scanning movement, noise and drift of the voltage supply, and thermal drift of the whole mechanical setup [85]. High-resolution SMM images require protection against disturbances that interfere with the stability of the microscope and a well-designed instrument includes several additional subsystems than those discussed in previous paragraphs.

First, mechanical stability and vibrational isolation are fundamental prerequisites to achieve good quality images. For this reason, the tip holder, sample holder, and actuators should be as rigid as possible to increase the mechanical eigenfrequency of the instrument [85]. Building vibrations can be attenuated by placing the microscope head on a vibration-insulating platform and elastic suspensions, as shown in Fig. 2.7. Moreover, protective enclosures of many kinds allow the reduction of acoustic noises that can produce oscillations.

Good stability of the tip position above the sample surface should be always achieved in SMMs. A temperature variation or the warming up of SMM elements could heavily provoke tip instabilities during operation due to thermo-elastic deformations of microscope elements; thus, measurements should be carried out once the system warm-up is completed. Sometimes, thermo-regulation of SPM heads and temperature compensating devices are employed in SMM systems to reduce the thermal drift [81]. Generally, mostly SMM scans with a long acquisition time could suffer from thermal deformation, and the scan speed should be sufficiently high to reduce the impact of thermal effects.

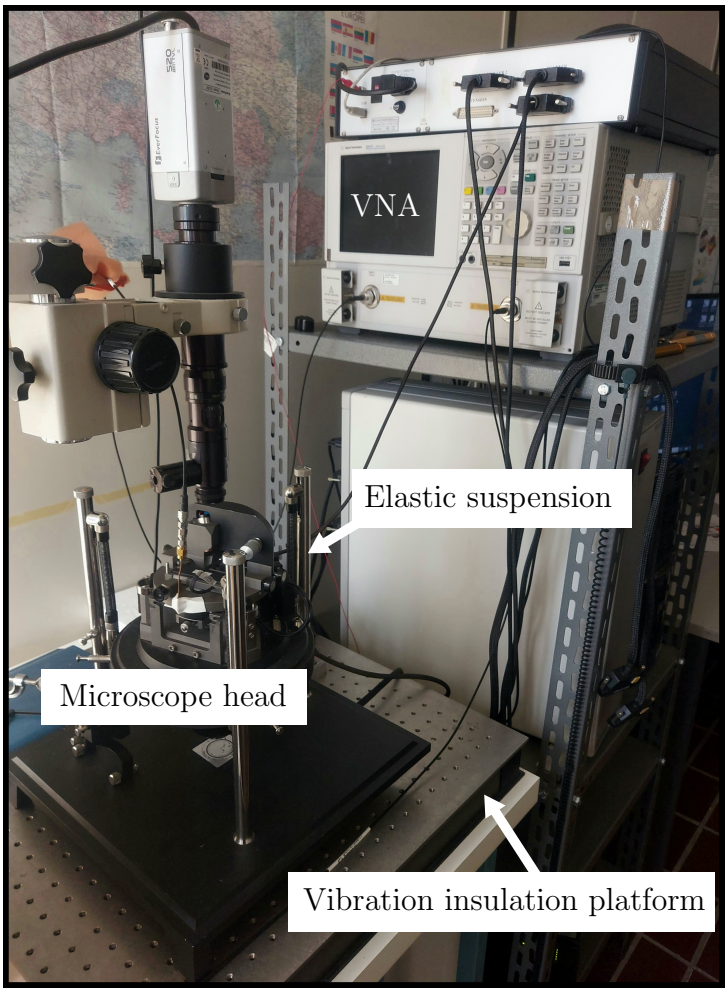

Figure 2.7

A Scanning Microwave Microscope made of a commercial Atomic Force Microscope head by NT-MDT (Solver Pro P-47) [86] coupled with a Keysight PNA E8361A Vector Network Analyzer (VNA). The elastic suspensions and a vibration insulation platform reduce most of the external mechanical vibrations.

Moreover, in a standard SMM operating in reflection mode, it is usually best to move the sample and to keep the probe fixed to its position. This because the probe is usually connected directly to the microwave signal path, incorporating cables or other elements that are sensitive to bending or other mechanical stress. The motion of the microwave network may induce instabilities in the microscope response and should be avoided. This will be no more valid in our new configuration presented in Ch. 4, because the microwave path is incorporated in a fixed sample holder and only the probe moves.

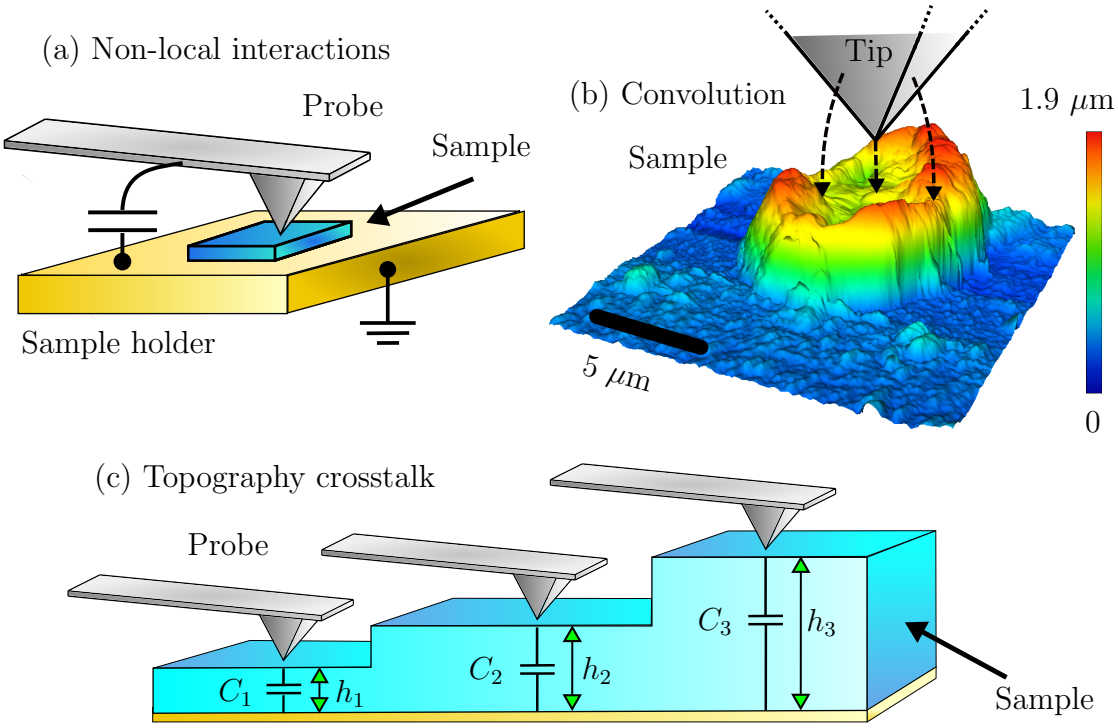

Figure 2.8

Main topographic artefacts in Scanning Microwave Microscopy: (a) non-local interactions, (b) convolution due to the finite spatial size of the probe near-field, and (b) topography crosstalk provoked by the tip-sample vertical movement needed to follow the sample topography.

4.2 Sources of artefacts in microwave images

Besides thermal and mechanical effects, electromagnetic interferences of various sources may corrupt captured data, thus the SMM instrumentation is often completely or partially integrated inside electromagnetic shields or absorbers to reduce electromagnetic noise [7]. However, parasitic effects caused by the same microscope structure and instrumentation also play a great role in the performance. These phenomena cause artefacts in the microwave image, *i.e.* data variations caused by effects not directly related sample local electromagnetic properties, thus mostly undesirable. Three main sources of artefacts can be identified and are represented in Fig. 2.8:

- non-local interactions;
- convolution due to the finite spatial size of the near-field;
- topography crosstalk provoked by the tip (or sample) vertical motion.

First, non-local interactions between the probe and sample modify the captured data: for instance in an AFM-based SMM, the presence of the probe cantilever generates an unwanted capacitance mostly independent on local sample properties, as indicated in Fig. 2.8 (a). Techniques to reduce unwanted interactions mainly rely on probe design (such as probe shielding) [45–47] and calibration of measurements [40, 49–53].

Moreover, a SMM captures not-only the response of a single spatial point of the sample, but senses electromagnetic properties around a certain volume close to the probe, due to the finite extension of the near-field. This effect, generally called convolution, depends on the probe dimensions, selected frequency, as well as sample properties. Full shielded probes lower the probe fringing field and reduce convolution, but they are very limited in the market [45]; moreover, a small antenna size enhances localized measurements, despite it generally lowers the Signal-to-noise ratio [41].

Unavoidable unwanted effects also exist, such as the so-called topography crosstalk, generated by the vertical probe motion during the scanning operation. This changes the tip-sample local impedance, independently on the sample electromagnetic properties variations and is generally unwanted. Techniques to reduce topographic effects have been proposed [87, 88], but these methods require additional measurements and cannot be used in real-time for the immediate visualization of sample properties in the instrument screen. During our research we addressed this open problem, and our new technical solution will be extensively discussed in the next chapter.

Chapter 3

Real-time Removal of Topographic Artefacts in Scanning Microwave Microscopy

Table of contents

Section 1

Introduction

Near-field Scanning Microwave Microscopy (SMM) employs microwave radiation to image and characterize samples down to the atomic scale, including soft biological structures or inorganic materials, such as ferroelectric films. However, SMM generally also senses the sample topography; hypersensitivity to topography becomes problematic with additional parasitic contributions and may partially or

completely mask non-topographic sample features in the data, such as contrast in electrical conductivity or permittivity. This chapter describes a simple and effective procedure to remove unwanted parasitic effects from SMM images. Differently from existing procedures [87, 88], the method is applicable either in post-processing or in real-time, *i.e.* during the scanning operation. This allows the immediate visualization of non-topographic sample features in the instrument screen. As a proof of concept, Hafnium Zirconium Oxide (HfZrO) ferroelectric film with high surface roughness is studied; unwanted contributions were removed from SMM data, providing a clear map of the sample ferroelectric structure that was originally hidden. We tested the method on ferroelectric samples, since a different known technique, the Piezoresponce Force Microscopy (PFM), may provide independent information about ferroelectric domains to be used for validation purposes.

A ferroelectric material presents two or more thermodynamically equivalent switchable polarization states-that is an intriguing feature for electronic applications such as high-density data storage and nonvolatile random access memories (FeRAM) [89]. PFM [89] allows the study of domain structures, domain switching, or local hysteresis behaviour of ferroelectric materials: an electrically biased tip induces a piezoelectric superficial strain (vertical, horizontal or a combination of the two) that is constantly monitored during the scan by means of the AFM probe. Different strain variations correspond to a change in the polarization orientation. In contact mode, a contrast in the microscope image appears when a difference in electrochemical, mechanical or piezoelectric property is present in opposite ferroelectric domains. PFM performs a non-destructive and high-resolution analysis of ferroelectric domains over large areas. Thus, the experimental results of SMM data obtained with the developed method is comparable to the experimental results of PFM technique in terms of visualization of ferroelectric features of the sample.

Section 2
Experimental setup and sample preparation

The insulating nature of the HfZrO ferroelectric sample characterized in this study requires the usage of an AFM-based SMM. We purposely developed an AFM-based system, represented in Fig. 3.1; it includes a commercial SPM by NT-MDT (Solver Pro P-47) coupled with a Keysight PNA E8361A Vector Network Analyzer (maximum frequency of 67 GHz). A flexible coaxial cable connects the AFM conductive tip to the VNA port, directly contacting the integrated gold pad of the tip operating

in contact mode (the Rocky Mountain Nanotechnology 12Pt400B for the single frequency image of Sec. 4.2 and the 12Pt400A model for the time-domain analysis of Sec. 4.3). The use of different tip models provided an additional evidence of the experimental reproducibility of our technique. Finally, an electromagnetic shield made by conductive tape is positioned between the tip cantilever and the sample to reduce non-local field interactions and improve the Signal-to-noise ratio (SNR). Note that this implementation is far from optimal, featuring large parasitic components, when compared to SMM that we implemented in other papers (*e.g.* the STM based SMM [22] or inverted SMM [24]); nonetheless it provides an ideal test-bed for the proposed procedure, that allows remarkable images in spite of the evident limits of the microscope.

Fig. 3.1 shows the analyzed ferroelectric sample made by 6 nm thick HfZrO growth by Atomic Layer Deposition on $Pt/SiO_2/Si$ substrate. A conductive wire contacts the top layer of the sample to perform the Piezoresponse Force Microscopy analysis; the capacitive coupling between the conductive wire and Pt layer revealed to be sufficient for the HfZrO excitation, without directly contact the two. Fig. 3.1 also shows the AFM topography of a 20×20 μm area of the sample; as it will appear later, the μm order thickness variation highly contributes to the collected S_{11} signal change. Ferroelectric properties and the hard rugosity make the sample ideal for our purpose of disentangling topographic and non-topographic properties.

Section 3

Theoretical background

3.1 Analytical analysis

In most cases, acquired SMM data depends both on geometrical features of the sample (such as topography) and material properties (such as dielectric constant, conductivity, and magnetic permeability) [10]. If we indicate with $\overline{\overline{\boldsymbol{S}}}$ the scattering matrix of the network, the geometrical features by a vector $\boldsymbol{h}$, and the material properties by a vector $\boldsymbol{p}$, we will get a typical dependence

$$\overline{\overline{\boldsymbol{S}}}(f, \boldsymbol{h}, \boldsymbol{p}) \tag{3.1}$$

where f indicates the frequency.

Changes in geometrical and material features will be often both very small around

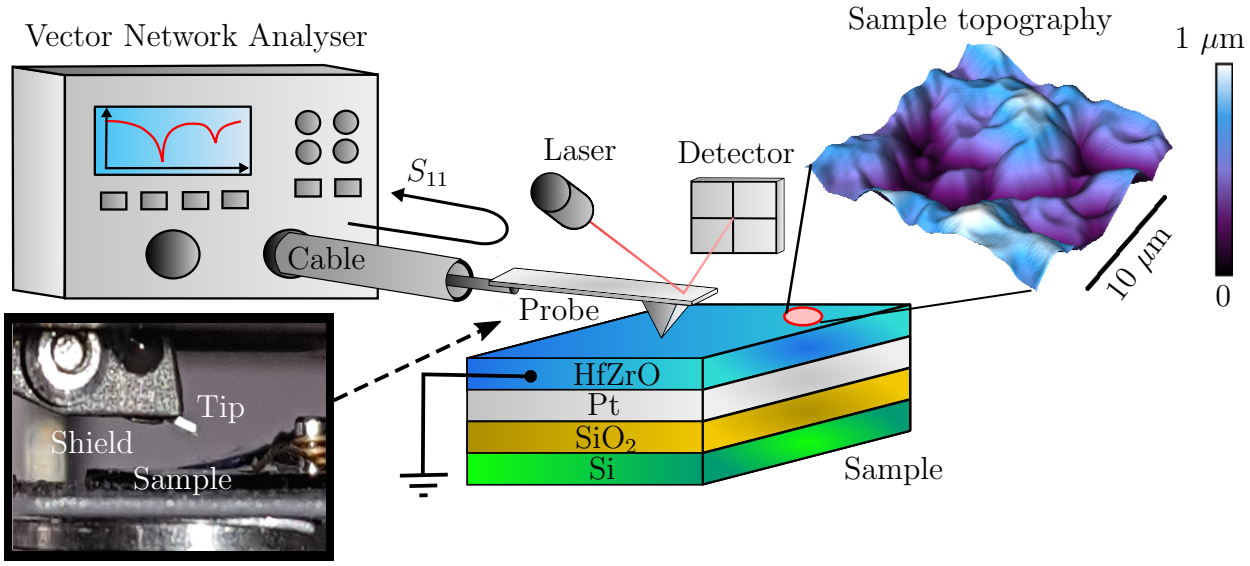

Figure 3.1

Scanning Microwave Microscope (SMM) experimental setup with representation of the Hafnium Zirconium Oxide (HfZrO) ferroelectric sample. A VNA injects and collects the microwave signal (S_{11}) through an Atomic Force Microscope (AFM) conductive tip, controlled by a laser-photodetector system. The inner conductor of a flexible coaxial cable physically contacts the AFM probe to electrically couple the tip with the VNA. Inset (left) shows a horizontal picture of the setup, in which an electromagnetic shield made by conductive tape is positioned between the tip and the sample; its purpose is to reduce the tip-sample non-local interactions, mainly due to the presence of the cantilever. The sample is composed by 6 nm thick HfZrO growth by Atomic Layer Deposition on $Pt/SiO_2/Si$ substrate. Inset (right) shows a sample topography area of 20×20 μm indicating a micrometer order rugosity.

macroscopic properties. For example, during the landing procedure of the probe, when the latter approaches the sample, there will be large changes in the whole $\overline{\overline{\boldsymbol{S}}}$ matrix; but during the scan, the values of $\overline{\overline{\boldsymbol{S}}}$ will be mostly stable and tiny variations of a fraction of dB provide the desired information both about changes in topography or material composition. Hence, after landing, all elements of the $\overline{\overline{\boldsymbol{S}}}$ matrix can be linearized with respect to geometrical and topographical features:

$$\overline{\overline{\boldsymbol{S}}}(f,\boldsymbol{h},\boldsymbol{p}) \sim \overline{\overline{\boldsymbol{S}}}(f,\boldsymbol{h_o},\boldsymbol{p_o}) + \nabla_h\overline{\overline{\boldsymbol{S}}}\cdot(\boldsymbol{h}-\boldsymbol{h_o}) + \nabla_p\overline{\overline{\boldsymbol{S}}}\cdot(\boldsymbol{p}-\boldsymbol{p_o}) \tag{3.2}$$

in which ∇_h and ∇_p respectively indicate the gradient of each element of $\overline{\overline{\boldsymbol{S}}}$ with respect to the vector $\boldsymbol{h}$ and $\boldsymbol{p}$. Note that hypothesis underlying the linearization performed in Eq. 3.2 could potentially not be satisfied in high-Q resonant or interferometry-based SMM where the sensitivity can be very high, leading to high variations of $\overline{\overline{\boldsymbol{S}}}$ with respect to the background.

The analysis becomes formally simplified when only considering the reflection coefficient S_{11} indicated by the generic parameter S, the only geometrical factor is the topography $h(x, y)$, and the only material variation is the electrical conductivity $\sigma(x, y)$. In this case, Eq. 3.2 becomes simply

$$S(f, x, y, h, \sigma) \sim S(f, x, y, h_0, \sigma_0) + \left.\frac{\partial S}{\partial h}\right|_{h=h_0} (h - h_0) + \left.\frac{\partial S}{\partial \sigma}\right|_{\sigma=\sigma_0} (\sigma - \sigma_0) \qquad (3.3)$$

e.g.

$$S(f, x, y, h, \sigma) - S(f, x, y, h_0, \sigma_0) \triangleq \Delta S = \left.\frac{\partial S}{\partial h}\right|_{h=h_0} (h - h_0) + \left.\frac{\partial S}{\partial \sigma}\right|_{\sigma=\sigma_0} (\sigma - \sigma_0) \quad (3.4)$$

where ΔS indicates the corrected $S(f, x, y)$ image (*e.g.* correction for plane tilt or deformation by polynomial fitting, as usually done in correcting images in Scanning Probe Microscopy [81]).

Note that S is still a complex quantity, whereas SMM images are always about either magnitude, phase, real part or imaginary part of S. This ambiguity is removed if we process data in time-domain, where S is real. Correction is usually performed at image level (hence not in the whole complex S in case of frequency-domain). In the following, to avoid the burden of a heavy notation, from here the symbol S will also refer to a real quantity (real, imaginary, phase, magnitude, or time-domain version of S). Of course, if for example we are working on function "magnitude of S", $\partial S/\partial h$ will be -without lack of generality- the derivative of the "magnitude of S" with respect to the topography h. Note that $(h - h_0)$ can be considered as a corrected topography $\Delta h(x, y)$.

The first term in the right-hand of Eq. 3.4 is what we generally call topography crosstalk, *i.e.* a phenomenon giving a replica of what seen *e.g.* by AFM or STM in the microwave image. When $\Delta h(x, y)$, or its multiplicative coefficient, is large such as *e.g.* in the rough surface of HfZrO sample in Fig. 3.1, and in particular with AFM-based microwave microscopes (owing to the contribution of the cantilever capacitance), this contribution may even dominate in 3.4, hiding completely the second term. In some cases, in a certain spatial area only topographic variations appear, hence $(\sigma - \sigma_0) = 0$, in some other only variations in material properties are present, *i.e.* $(h - h_0) = 0$ and in most cases they are combined.

If we define

$$h_{\mathrm{M}} = \mathrm{Max}(h - h_0) = \mathrm{Max}(\Delta h) \tag{3.5}$$

we will have

$$h^* = \frac{\Delta h}{h_{\mathrm{M}}} \tag{3.6}$$

and Eq. 3.6 defines a normalized topography, conventionally ranging between $\{0, 1\}$.

Dividing 3.3 by the term $\left.\frac{\partial S}{\partial h}\right|_{h=h_0} h_{\mathrm{M}}$ results in

$$S^* = h^* + \frac{\left.\frac{\partial S}{\partial \sigma}\right|_{\sigma=\sigma_0}}{\left.\frac{\partial S}{\partial h}\right|_{h=h_0} h_{\mathrm{M}}}(\sigma - \sigma_0) = h^* + \alpha(\sigma - \sigma_0) \tag{3.7}$$

where

$$\alpha = \frac{\left.\frac{\partial S}{\partial \sigma}\right|_{\sigma=\sigma_0}}{\left.\frac{\partial S}{\partial h}\right|_{h=h_0} h_{\mathrm{M}}} \tag{3.8}$$

and

$$S^* = \frac{\Delta S}{\left.\frac{\partial S}{\partial h}\right|_{h=h_0} h_{\mathrm{M}}} \tag{3.9}$$

Therefore, the quantity

$$S^* - h^* = \alpha(\sigma - \sigma_0) \tag{3.10}$$

provides an image highlighting contrast in sample conductivity and mostly independent on topography.

From a practical point of view, the first step is to correct the S image (*e.g.* magnitude image by polynomial fitting) as well as the topography. Then h is normalized between 0 and 1, and the corrected S image is normalized dividing it by $\left.\frac{\partial S}{\partial h}\right|_{h=h_0} h_{\mathrm{M}}$. At this point the two images are subtracted.

To normalize the S image we should be able to evaluate $\left.\frac{\partial S}{\partial h}\right|_{h=h_0} h_{\mathrm{M}}$: this can be rigorously done, since the numerical evaluation of $\left.\frac{\partial S}{\partial h}\right|_{h=h_0}$ can be performed in a way similar to the acquisition of S at different distances [41] involved in the calibration, but keeping the probe close to the landing conditions. As a consideration,

the quantity $\left.\frac{\partial S}{\partial h}\right|_{h=h_0} h_{\mathrm{M}}$ is a number independent of the position (x, y), being the result of the movement of the probe with respect to ground when the material of the sample is removed in Eq. 3.4, *i.e.* $(\sigma - \sigma_0) = 0$.

The analysis simplifies in the case where

$$\left.\frac{\partial S}{\partial h}\right|_{h=h_0} (h - h_0) \gg \left.\frac{\partial S}{\partial \sigma}\right|_{\sigma=\sigma_0} (\sigma - \sigma_0). \tag{3.11}$$

This holds either if the sensitivity to the topography is larger than to the material change or if its topography changes, weighted by the microscopic sensitivity, are more significant than material changes. In this context, how precisely we capture the topography directly influences how accurately we measure the material property: in principle we can reach atomic resolution with modern configurations [8]. Condition 3.11 may happen when using AFM-based approaches, especially because of the large stray capacitance between the body of the AFM cantilever and the sample. If equation 3.11 holds, it will be simply necessary to normalize ΔS to his maximum S_{M} since

$$S \sim \left.\frac{\partial S}{\partial h}\right|_{h=h_0} h_{\mathrm{M}} \tag{3.12}$$

so that

$$S^* = \frac{\Delta S}{S_{\mathrm{M}}} \tag{3.13}$$

Note that S^* is again a quantity ranging between $\{0, 1\}$. The above simplification can for example even hold when the sample is quite flat but at the same time variations in material properties are very small, like in the polarization domains of ferroelectric materials. Basically, every time a very large impact of topography crosstalk is present, approximation 3.12 applies. Moreover, while here we are focusing on imaging, with some care, the same line of reasoning can be used to provide quantitative data, namely in the framework of an alternative calibration technique. In the most general case, we should deal with expression 3.2.

To summarize, the steps involved in the topography cross-talk correction are schematized in the following flowchart and are:

1. Correct the S image and topography image for possible tilt or deformation;

2. Normalize the S image and topography image between $0, 1$. As detailed later, the normalization performs either in-line, *i.e.* considering each scan line with

its own maximum and minimum, or in-plane, *i.e.* accounting for the maximum and minimum of the whole image;

3. Subtract the normalized S and topography images.

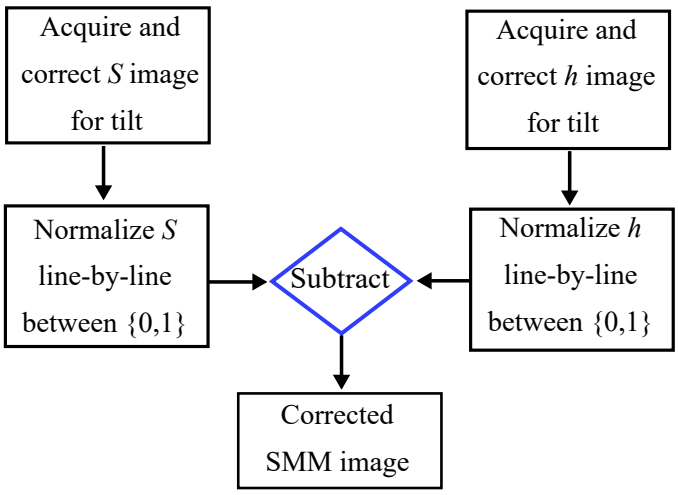

An underlying assumption is that the topography $h(x, y)$ is correctly detected, as happens when using AFM with a closed feedback loop, enforcing a constant deflection/force during the scan. Of course, still there will be the usual sources of artefacts in AFM, such as the convolution with the probe shape. However, the general sources of artefacts in scanning probe microscopy are beyond the scope of this work, since we are interested in disentangling the information coming from movements of the AFM probe and the electromagnetic properties.

3.2 Simulation results

The RF Module of COMSOL® Multiphysics is employed to entirely reproduce the SMM scanning operation and to numerically validate the proposed procedure. A three-dimensional model shown in Fig. 3.2 reproduces the microscope setup, including the conductive AFM tip, sample, VNA, and sample holder. A lumped port (connected to the cantilever) illuminates the sample and collects the reflected signal. The tip electrically contacts the sample as in the AFM contact mode operation of our experiments.

The horizontal and vertical movement of the probe reproduces the sample scan operation. Fig. 3.2 (b) shows the simulated sample made of six joined silicon pads with variable electrical conductivity and thickness, mixing topographic and electrical properties variation. Fig. 3.3 (c) provides a close view of the tip-sample geometry with

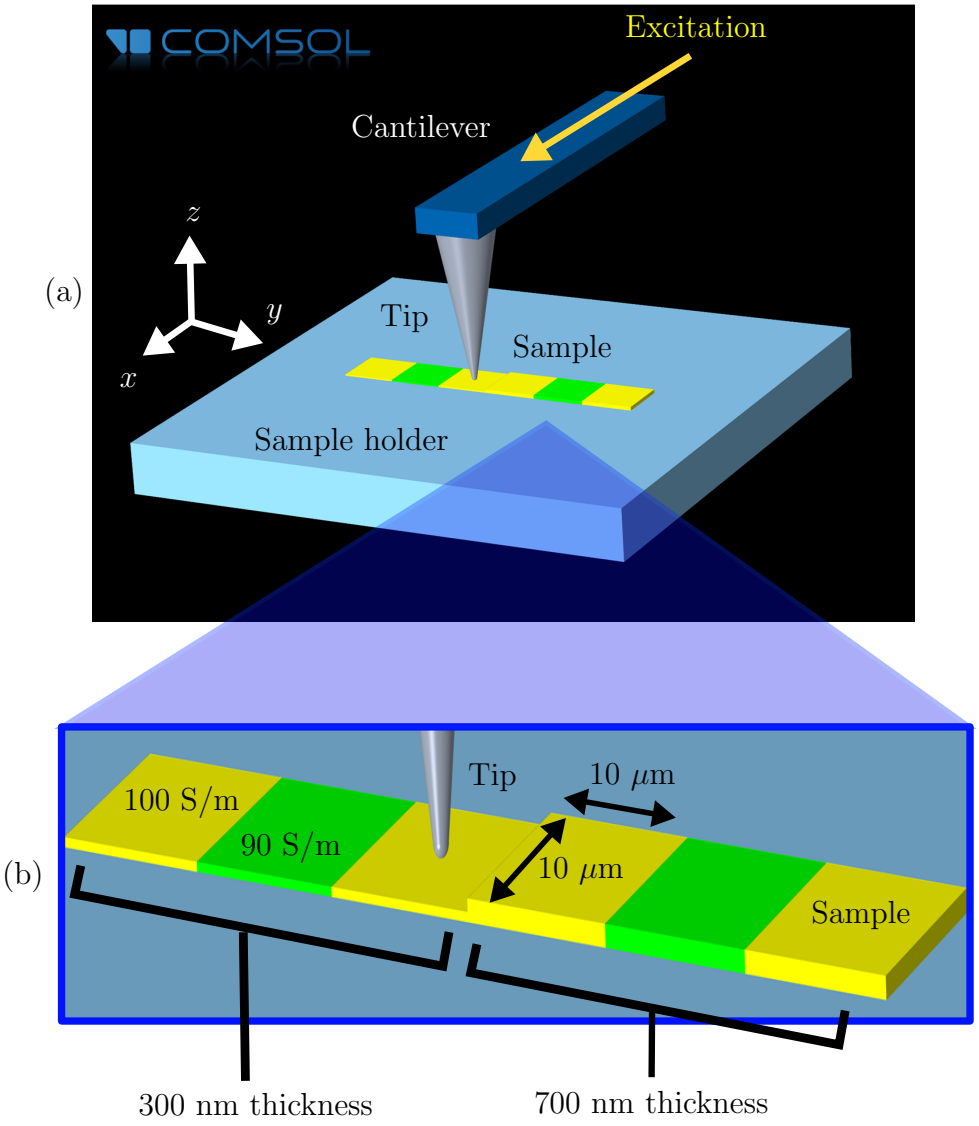

Figure 3.2

Three-dimensional COMSOL® Multiphysics (RF Module) model of the Scanning Microwave Microscope, including the tip (formed by the cantilever, cone, and point-ball apex), sample, excitation port, and sample holder. (b) Simulated sample geometry composed of silicon bricks with an electrical relative permittivity of 11.68 and conductivity of respectively 100 S/m (yellow pads) and 90 S/m (green pads). Left and right bricks are respectively 300 nm and 700 nm thick with lateral dimensions of 10×10 μm.

an indication of probe trajectory during operation, electric potential distribution, and electric field lines obtained with the simulator. Moreover, Fig. 3.3 (b) illustrates the sample profile h and the simulated scanning operation. The probe scans along the y-axis in contact with the sample. For each tip position, the reflection parameter at 4.5 GHz is recorded and drawn in Fig. 3.3 (c). As expected, the S_{11} contrast amplitude ($\Delta|S_{11}|$) highlights two contributions mixed in the line scan: one corresponds to

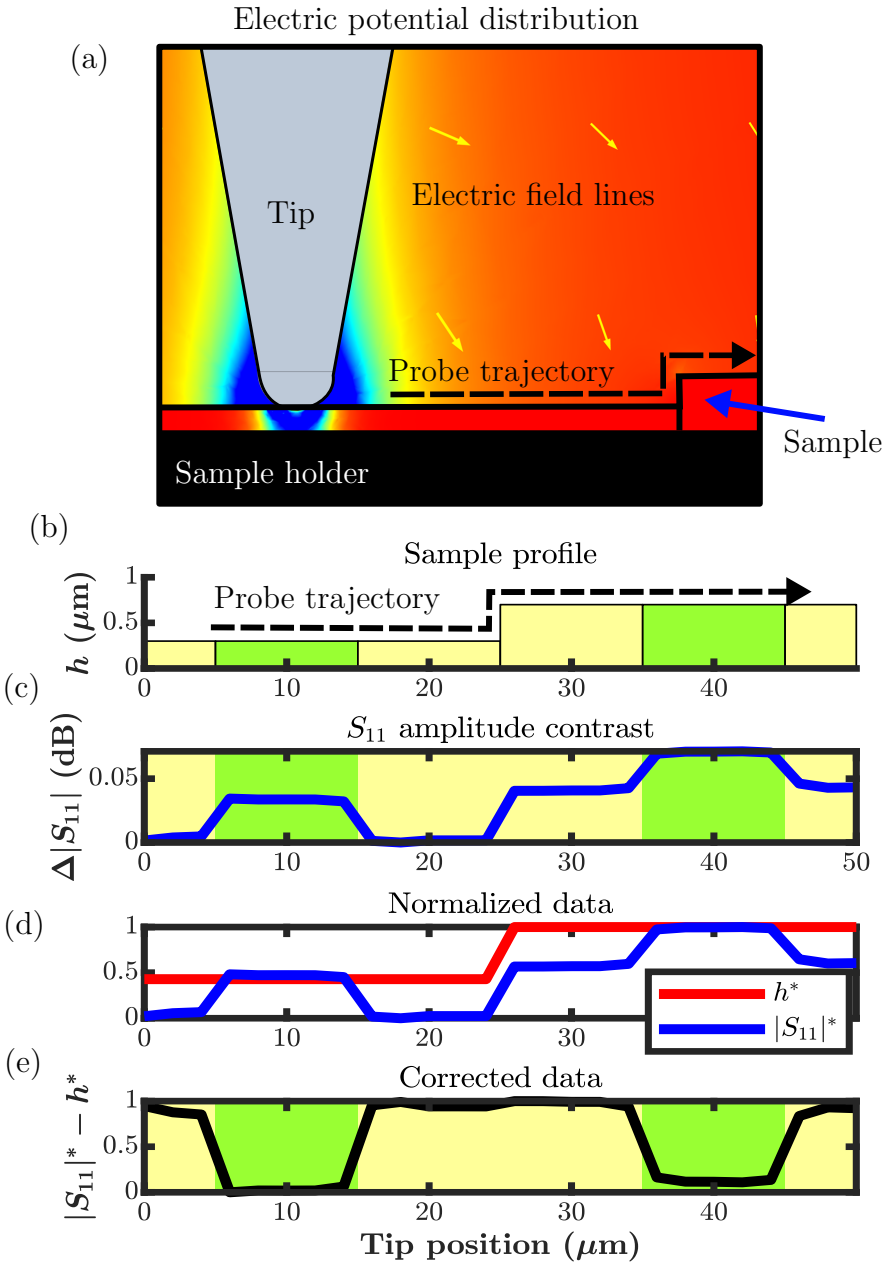

Figure 3.3

(a) Cross-section of simulated electric potential distribution and electric field lines (at 4.5 GHz) nearby the tip, modelled as a truncated cone with spherical apex. The tip radius is 500 nm, the contact radius 50 nm and the half cone angle 10°. COMSOL® simulation of scanning operation with (b) representation of sample profile h and probe trajectory. Yellow and green regions indicate silicon with a conductivity of respectively 100 S/m and 90 S/m. (c) Amplitude of reflection coefficient contrast ($\Delta|S_{11}|$) with indication of material (M) and topography (T) contributions. (d) Normalized topography and S_{11} amplitude in the interval $\{0, 1\}$. (e) Normalized difference $\Delta|S_{11}|^* - h^*$ indicating a contrast mainly due to the sample conductivity change.

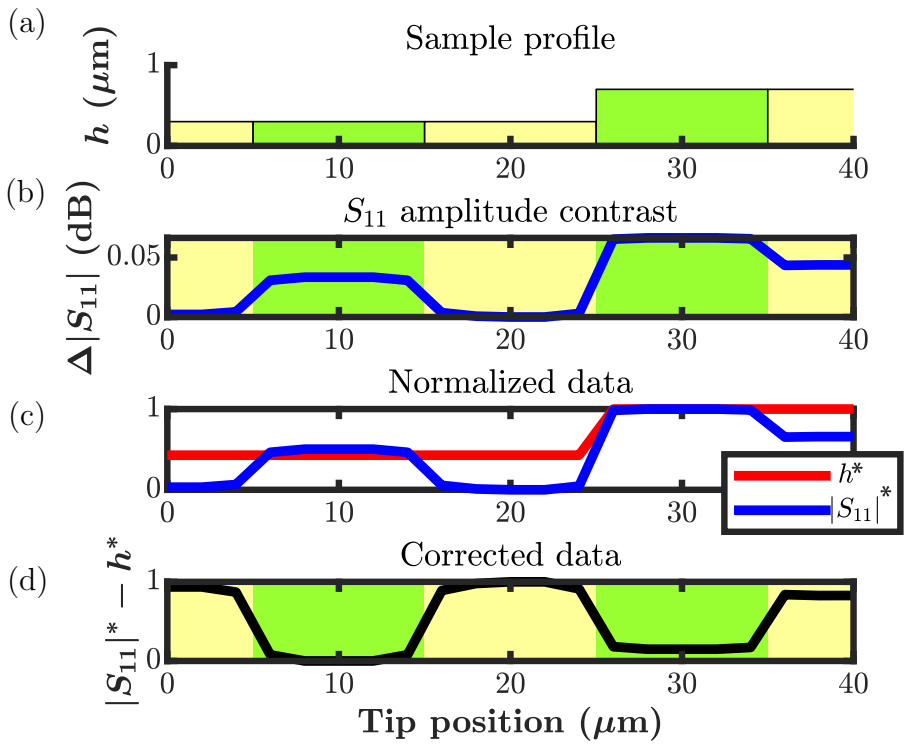

Figure 3.4

Simulation of a scanning operation for the case of simultaneous topography and material property variation. (a) Representation of sample profile h and electrical conductivity regions of respectively 100 S/m (yellow) and 90 S/m (green). (b) Amplitude of reflection coefficient contrast ($\Delta|S_{11}|$) with only material (M) contribution, and simultaneous topography and material (T+M) contributions. (c) Normalized topography h^* and $|S_{11}|^*$ amplitude. (d) Corrected $|S_{11}|^* - h^*$ indicating variations mainly due to electrical conductivity changes.

material properties change (indicated with M), and one to the topographic sample variation (T). Note that the so-called convolution effect generates the sloped profile shapes of $\Delta|S_{11}|$, arising from the finite spatial size of the near-field around the tip apex. Here this is evident due to the large tip radius of 500 nm.

To remove the topographic effect from the recorded data, both h and $\Delta|S_{11}|$ are normalized in the interval $\{0, 1\}$, as shown in Fig. 3.3 (d). The two contributions are then subtracted and the resulting $\Delta|S_{11}|^* - h^*$ (again normalized) is shown in Fig. 3.3 (e): the material contrast dominates the corrected signal and the variation corresponding to the topography change (absolute height difference of 500 nm) is now negligible. In this case there was no need to correct h and $\Delta|S_{11}|$ for tilt because the sample is flat. Of course, in case of plane removal correction to the original data, the results would be identical to those in Fig. 3.3.

Fig. 3.3 describes the scenario of a large step in the sample topography in a region

with no material contrast; however, abrupt changes in topography and material properties may appear simultaneously. Fig. 3.4 reproduces this case and considers a different electrical conductivity distribution of the sample than the one of Fig. 3.3: here the topography change (at the position of 25 μm) also corresponds to a material variation, as depicted in Fig. 3.4 (a). Throughout the same correction steps of Fig. 3.3, the procedure removes the effect of topography from the S_{11} contrast amplitude ($\Delta|S_{11}|$), shown in Fig. 3.4 (b), and again the corrected data of Fig. 3.4 (d) indicate a contrast mainly due to electrical conductivity variations.

Section 4

Experimental results

4.1 Microscope sensitivity

The microscope firstly required the verification of microwave imaging capabilities: the optimum working frequency maximizes the Signal-to-noise ratio (SNR) defined as in equation 1.1. From Fig. 3.5, since the S_{11} phase ($\angle S_{11}$) has the maximum SNR (higher than 20 dB at 4.5 GHz), it is selected for the subsequent single frequency imaging. The result of Fig. 3.5 refers to the setup employing the 12Pt400B Rocky Mountain Nanotechnology tip; very similar behaviour is obtained with the 12Pt400A model, with optimum frequency around 4.8 GHz already shown in Fig. 1.4.

4.2 Single frequency imaging of ferroelectric domain walls

The developed method applies directly on the raw S parameter (corrected for tilt or deformation), either in amplitude or phase coefficient. For convenience, all the quantities shown in this paragraph are normalized in the interval $\{0, 1\}$. The original unit of measure is radians for the S_{11} phase and meters for topography, and after normalization, both are represented by pure numbers. The normalization process is performed line by line, *i.e.* normalizing each line separately (S_{M} and h_{M} are chosen within the specific line) along the mechanical scanning direction during the image acquisition (x-axis): by ordinately joining the processed lines, the two-dimensional image is composed [81].

Fig. 3.6 (a) and (b) respectively show the normalized AFM topography h^* of the HfZrO sample and the simultaneously acquired normalized phase of reflection coefficient $\angle S^*$ at 4.5 GHz (20×20 μm image size and 256×256 pixels). Both data are corrected for a plane tilt with a first-order (linear) correction. The correlation

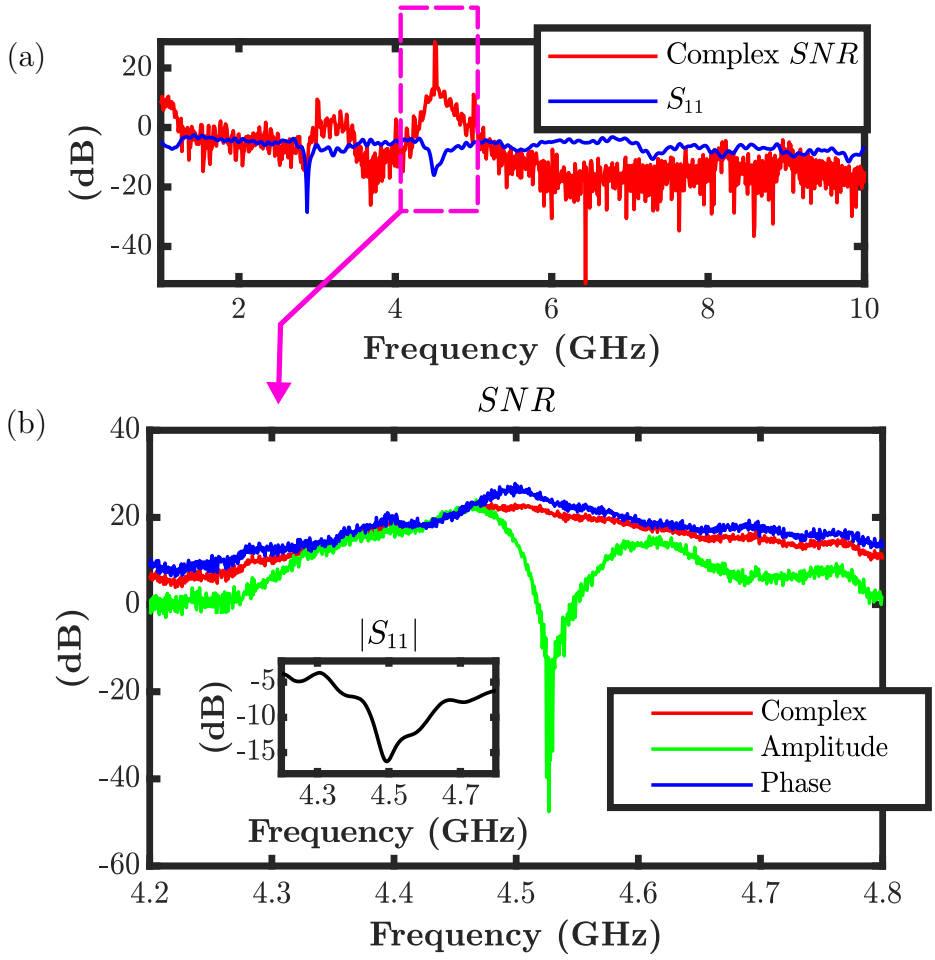

Figure 3.5

(a) Microscope complex sensitivity with the 12Pt400B Rocky Mountain Nanotechnology tip. The Signal-to-noise ratio (SNR) peaks around 20 dB in correspondence of a reflection minimum (S_{11}) at 4.5 GHz. (b) Complex, amplitude and phase SNR in the band 4.2-4.8 GHz. The S_{11} phase maximizes the SNR in the whole band. Inset: $|S_{11}|$ minimum around -16.5 dB at 4.5 GHz.

between topography and SMM data is evident, and at first sight the two images seem almost identical. The cross-section profiles of the two data in Fig. 3.6 (c) highlight the common trend: the topography crosstalk dominates the SMM data and masks the non-topographic effects.

The in-plane normalization is an alternative of the single line one. In this case, S_{M} and h_{M} are selected within the whole scan, and they normalize the entire images: this approach is computationally faster, but we must consider that the presence of external interferences, noise, or any signal fluctuation over time generates further contrasts between pixels [90]. Practically, this provokes a deformation in the two-dimensional scan (additional to that due to sample tilt or bending) and is more

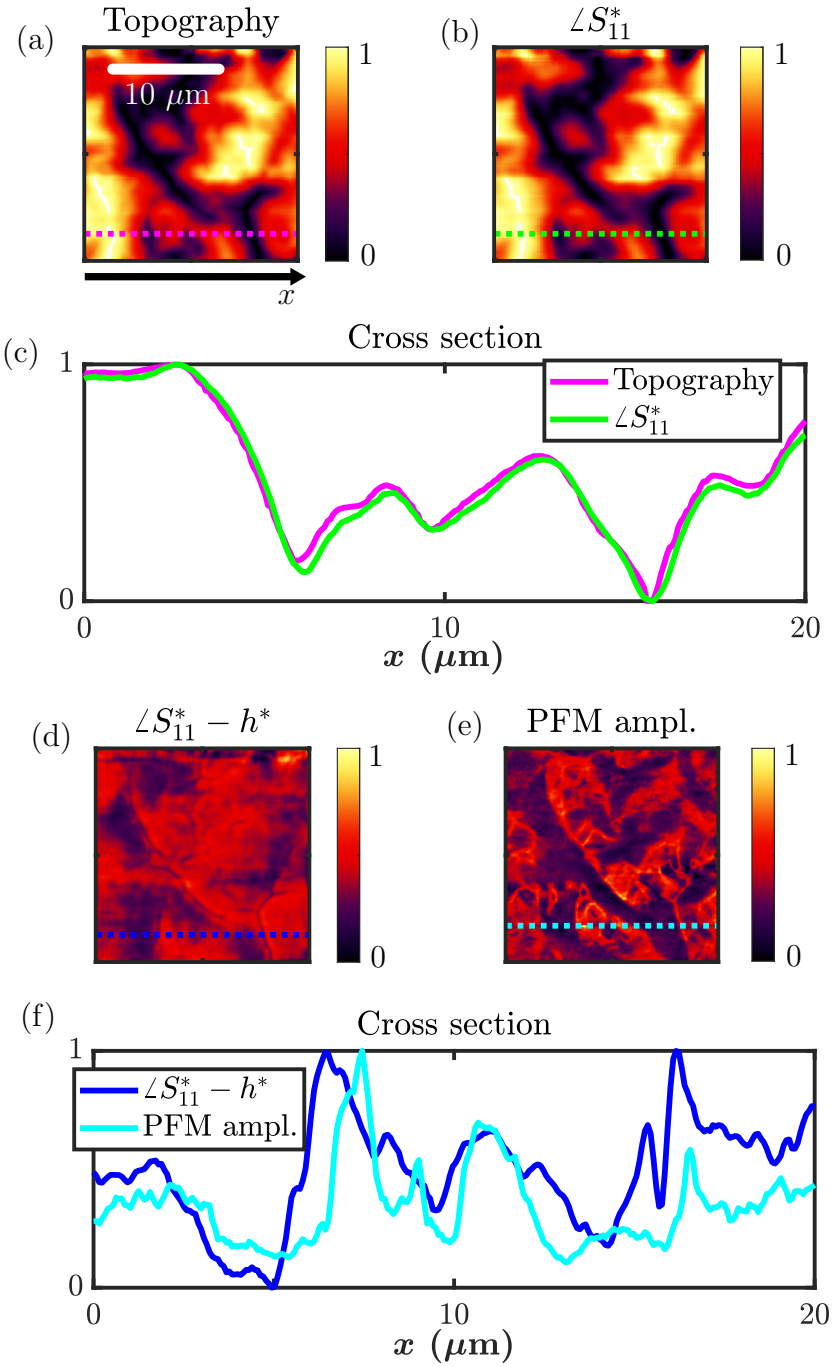

Figure 3.6

(a) Atomic Force Microscopy (AFM) normalized topography h^* of HfZrO sample. (b) Simultaneously acquired normalized phase of reflection coefficient $\angle S^*$ at 4.5 GHz: the high correlation between topography and S parameter indicates the dominance of crosstalk and parasitic contributions in the data. (c) h^* and $\angle S^*$ cross-sections along the dotted lines of Fig. (a) and (b). (d) Corrected phase of reflection coefficient $\angle S^* - h^*$ normalized in the interval $\{0, 1\}$ revealing the presence of ferroelectric domains and domain walls. (e) Piezoresponse Force Microscopy (PFM) amplitude image of the sample; scanning area slightly shifted than Fig. (a), (b), and (d). PFM confirms the presence of a ferroelectric structure with the same shape as the one obtained with the Scanning Microwave Microscope (SMM). (f) Cross-section of the corrected $\angle S^* - h^*$ data along the dotted line of Fig. (d) comparing the result to the PFM response of Fig. (e). Normalized AFM and SMM data are obtained with the in-line normalization process.

evident for slow acquisitions in which instabilities may become significant. When this happens, the normalization correctly processes some spatial regions, but it badly operates on some others, because the microwave signal changed during the scan.

By normalizing every single line with its own maximum (in-line normalization), the signal fluctuation is only related to that line and does not affect other pixels. Moreover, the entity of signal change is usually lower than those happening during a complete scan due to the much lower acquisition time. Single line normalization is most suitable for single frequency data. Instead, plane normalization is applicable when combining multiple frequency images in time-domain data (as shown in the next paragraph), because the image formation process reduces signal instabilities and noise.

Following the steps of our method, normalized data of Fig. 3.6 (a) and (b) are subtracted and Fig. 3.6 (d) shows the corrected $\angle S^* - h^*$, again in the interval $\{0, 1\}$ and the new data reveals additional elements beyond the sample topography. These features correspond to superficial and sub-surface variation of non-geometrical properties: the smooth behaviour of sample topography is cancelled and replaced by sharp edges and veins, typical of ferroelectric domain walls [35, 36, 89].

Piezoresponse Force Microscopy (PFM) analysis allowed us to validate the visualization of the ferroelectric domain structure and was conducted immediately after SMM, without altering the setup. Fig. 3.6 (e) depicts the captured PFM amplitude response: most of the details, shapes and edges of the domains are common in the two images, showing a clear correlation between corrected SMM and PFM. Finally, the cross-section of Fig. 3.6 (f) shows a detail of some peaks and valleys corresponding to the sample ferroelectric structure, in which a common trend is clearly visible. Note that the SMM and PFM images are slightly spatially shifted, being acquired non-simultaneously, due to the instability of the piezoelectric actuator.

As an important remark, we note that the domain image visualization of SMM and PFM relies on two different fundamental mechanisms: the first depends on the local impedance variations along the sample ferroelectric structure, while the second is given by the piezoelectric induced stress when applying a tip-sample bias and is revealed only by the AFM setup. Hence, we expect that SMM and PFM both reveal non-topographical features, but we do not expect identical images. From our results, this means that HfZrO domain walls show a local impedance change at GHz frequencies with respect to the impedance of the domain itself. This behaviour has been observed in the past for other ferroelectric materials such as PZT films, where domain walls have shown a change in conductivity with respect to the bulk

material [35].

4.3 Time-domain images correction

A possible approach to SMM data processing is to move post-processing steps from the frequency domain to the time domain [50]. In an SMM, near-field and far-field interactions exist simultaneously, and the idea is to disentangle their contributions based on their separation in time. This time separation is used as a filter to remove non-local interactions from the captured images. This reduces the presence of noise and gives a general improvement of the image quality while also allowing alternative calibrations [23]. Of course it needs measurements at a band of frequencies, and usually broadband sensitivity can be difficult to achieve, and time-domain improvement can be heavily reduced in resonant SMM.

Data representations such as the time-domain form [50] commonly show similar dependence and sensitivity to the sample topography such as the single frequency one; this also occurs for other calibrated data forms [42] because the tip-sample admittance depends on the probe-ground distance. Thus, even for de-embedded data of non-flat samples, material properties could be mostly invisible without any further form of correction.

The formation of time-domain data requires the acquisition of a sufficient number of single-frequency images in a predetermined (and sensitive) band of the instrument [50]. Than, the measured frequency-domain responses are linearly combined to a time domain signal $s(t)$

$$s(t) = \sum_{f_i} \mathrm{Re}\{K(f_i)S(f_i)\mathrm{e}^{\mathrm{j}2\pi f_i}\}, \tag{3.14}$$

where f_i indicated the frequency, $S(f)$ is the reflection coefficient as measured in the given frequency band, and $K(f)$ is a weighting function (such as a Kaiser- Bessel windowing function [50], but other windowing functions are possible). For equidistant frequency points within the selected bandwidth, Eq. 3.14 becomes a standard finite inverse Fourier transform. Practically speaking, the process gives a final matrix of images, each one at a certain time instant. The instants corresponding to the microwave signal interaction with the sample bring useful information.

Here, the setup employs the 12Pt400A Rocky Mountain Nanotechnology tip and the optimum band between 4.3 and 5 GHz was selected to image the sample (see again Fig. 1.4 (b) showing the instrument sensitivity), in which 512 frequency points

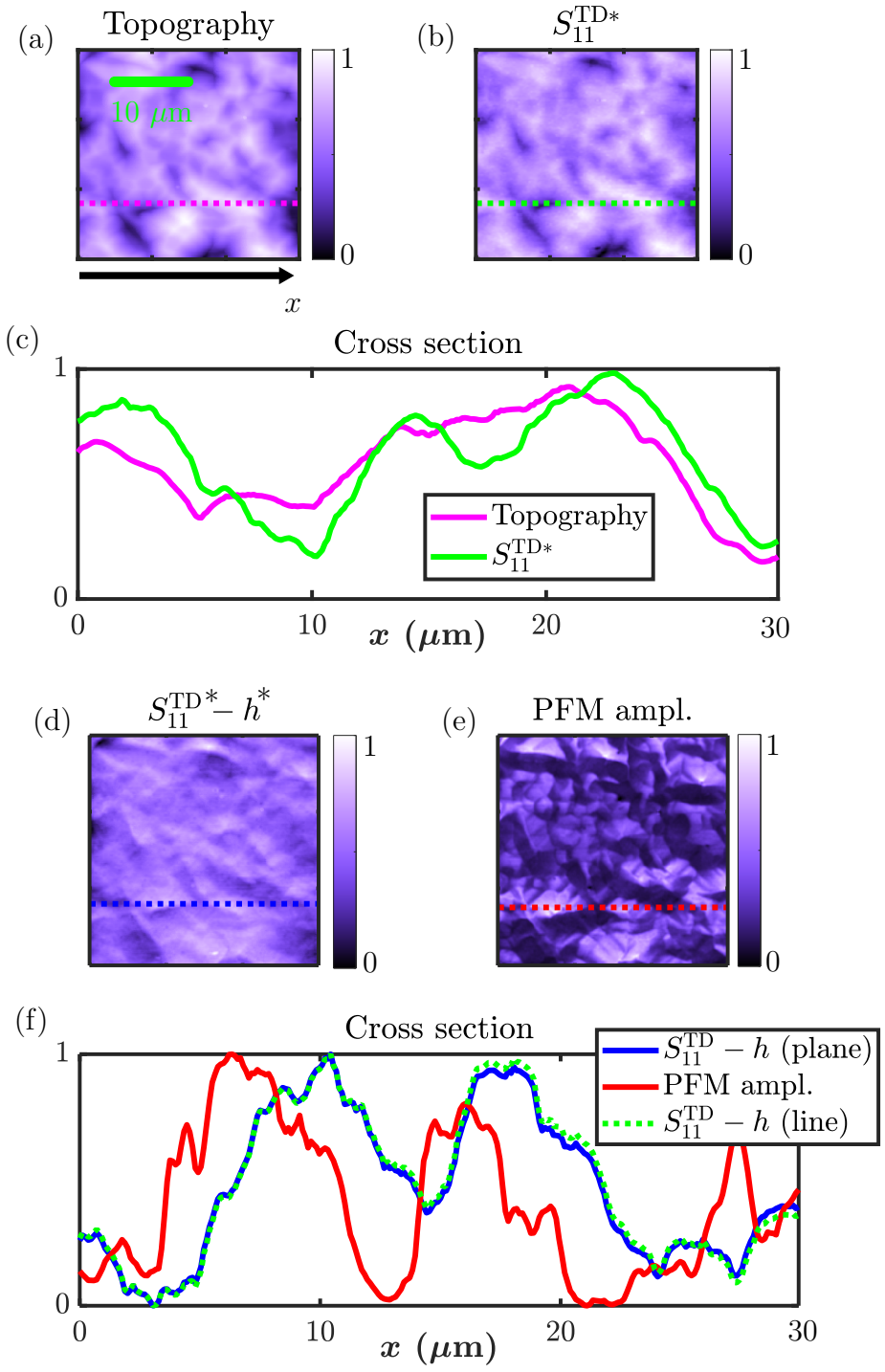

Figure 3.7

(a) In-plane normalized topography h^* of Hafnium Zirconium Oxide (HfZrO) sample. (b) Corresponding in-plane normalized time-domain reflection coefficient S_{11}^{TD*} obtained in the 4.3-5 GHz frequency band, indicating a large correlation with h^*, mainly due to topography crosstalk. (c) Normalized h^* and S_{11}^{TD*} profiles along the dotted lines of Fig. (a) and (b). (d) Corrected $S_{11}^{TD*} - h^*$ data: the now visible sharp edges, hidden in the original S_{11}^{TD*} coefficient, reveal the presence of HfZrO ferroelectric domains. (e) Piezoresponse Force Microscopy (PFM) amplitude response showing the same ferroelectric structure than the Scanning Microwave Microscope (SMM) image. PFM and SMM are conducted separately, resulting in a spatial shift of few microns. (f) Cross-section of corrected $S_{11}^{TD*} - h^*$ with in-plane and in-line (dotted) normalization procedure compared to the PFM response of Fig. (e).

were acquired to form the broadband image with 256×256 pixels each. Note that the resulting parameter in the time-domain process is a real number: there is no need of choosing between amplitude or phase in our correction procedure.

Fig. 3.7 shows the time-domain processed data $S_{11}^{\mathrm{TD}*}$ and the simultaneously acquired HfZrO sample topography (in a different scan area than that of Fig. 3.6). Topography crosstalk is also evident in this case, again masking the contribution of the material, especially in the two-dimensional image. On the other hand, the corrected $S_{11}^{\mathrm{TD}*} - h^*$ of Fig. 3.7 (d) shows the clear evidence of a ferroelectric structure, compared to the PFM amplitude response of Fig. 3.7 (e). Again, sharp edges indicate domain walls and the smooth trend due to sample geometry is removed.

Fig. 3.7 (a) and (b) involve an in-plane normalization: all the 256 scan lines are normalized together between the interval $\{0, 1\}$ with respect to the general maximum S_{M} and h_{M} of the whole two-dimensional image. The applicability is restricted to data that are not corrupted by signal drift over time or excessive noise, such as time-domain images. Fig. 3.7 (f) compares a cross section of the corrected $S_{11}^{\mathrm{TD}*} - h^*$, processed respectively with in-plane and in-line normalization, indicating almost identical results. Single frequency data forming the time-domain image show similar contrast and details as the ones obtained for the first experiment in Fig. 3.6, and the topography-free images provide common features with PFM with quality fully compatible with the one in Fig. 3.6, thus not provided here for the sake of compactness.

The choice between practical real-time analysis (single frequency) or a more advanced and higher quality approach (time-domain) mainly depends on the purpose, use, and requirements of the study. For instance, a stable and fully static sample such as the HfZrO film is excellent for a time-domain study; on the other hand, the faster single frequency acquisition is more suitable for the analysis of a live cell in a liquid environment, extremely subject to superficial detachment and/or mechanical instabilities [25].

Section 5

Conclusion and perspectives

The method proposed in this chapter is a fast and effective tool for a rapid visualization of non-topographic sample properties in Scanning Microwave Microscopy (SMM). It highly reduces parasitic elements from raw or calibrated SMM data: in samples with significant superficial roughness, those components are mainly caused

by the unavoidable topography crosstalk that may be the dominant contribution. In few steps, the protocol cancels this effect and retrieves material related variations of the data.

The protocol stands out for the flexibility and ease of use: it does not require any additional measurement than the standard acquisition of sample topography and S parameter; it only involves simple data processing, including a correction of the image for plane tilt or deformation, data normalization, and difference. The computational time of those operations is negligible with respect to the typical line-scan acquisition time of most common Scanning Probe Microscopes (of the order of seconds or fractions of seconds). This enables the removal of unwanted effects in real-time, *i.e.* during the scanning operation.

The technique has potential applications in the study of a wide variety of inorganic samples (such as multi-layered microelectronic devices or rough surface materials) and organic structures: the latter includes biological cells, in which the external topological features could mask many of the inner sub-elements (such as organelles), mostly unrevealable in uncorrected data.

Chapter 4

The Inverted Scanning Microwave Microscope

Table of contents

Section 1
Introduction

This chapter presents an instrument called an inverted Scanning Microwave Microscope (iSMM), which is capable of performing non-invasive and label-free imaging

and characterization of intracellular structures of a live cell on the nanometre scale, as well as quantitative analysis of inorganic materials. The iSMM not only senses surface structures but also electromagnetic properties below the surface. Conveniently, the iSMM is easily constructed from existing Scanning Probe Microscope (SPM) configurations, such as the Atomic Force Microscope (AFM) or the Scanning Tunnelling Microscope (STM), with a simple metal probe to outperform a traditional SMM in terms of ruggedness, bandwidth, sensitivity, and dynamic range. By contrast, the application of the traditional SMM to date has been limited to mainly surface physics and semiconductor technology because the traditional SMM requires a fragile and expensive probe and is incompatible with saline solutions or live cells.

The chapter is organized as follows: Sec. 2 motivates the iSMM setup and describes the advantages with respect to conventional techniques. Sec. 3 presents some of the obtained imaging results on biological samples, including live cells, showing the image quality obtained. Sec. 4 describes the theoretical model of the system and the calibration of the microscope. Finally, Sec. 5 describes a numerical model that reproduces the complete iSMM operation with a full-wave approach; the simulations validate a calibration algorithm for reflection and transmission-mode measurements. This opens the way to the high-frequency quantitative characterization of a wide variety of samples and surfaces.

Section 2

Motivations and advantages of the setup

2.1 Traditional VS inverted Scanning Microwave Microscope

In principle, one of the most impactful applications of the SMM is in noninvasive, label-free imaging and characterization of live cells, organelles, bacteria and viruses. However, so far there have been only a few reports on the application of SMM in biology, and they are limited to dead or barely surviving sample [13, 50, 91]. This is mainly because the microwave probe is often incompatible with the saline solution necessary to keep a cell alive.

Even if the probe survives the saline solution, it is rendered insensitive by the parasitic interaction between the probe body and the surroundings [10, 46] shown in Fig. 4.1 (a). In fact, because a conducting sample holder is usually used to maximize the reflection of the microwave signal, the parasitic interaction between the probe body and the surroundings can be orders-of-magnitude larger than the intrinsic interaction between the probe tip and the sample. It is even worse when the probe

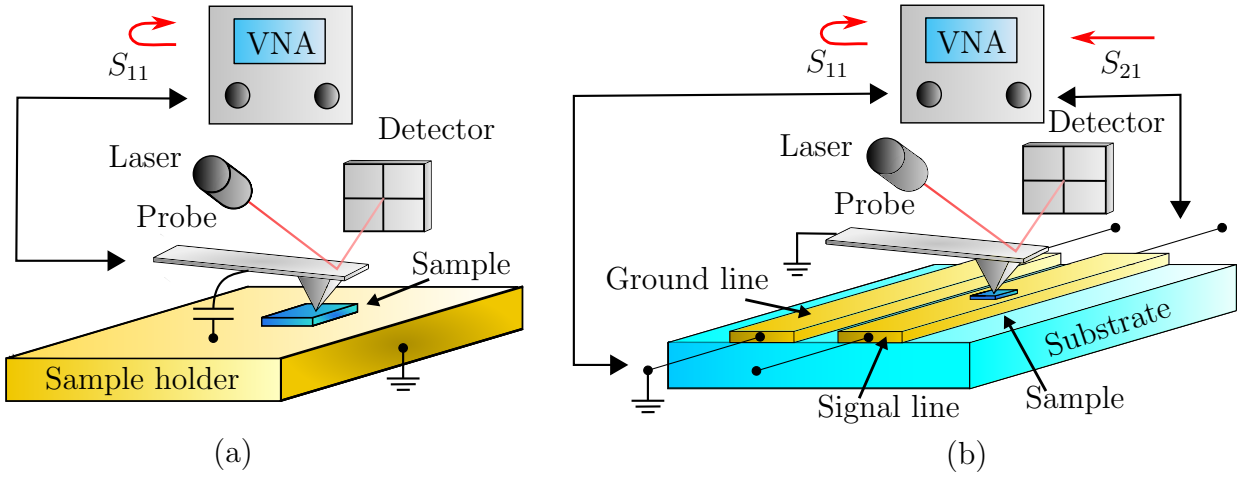

Figure 4.1

(a) Schematics of a traditional Atomic Force Microscopy (AFM)-based Scanning Microwave Microscope and (b) an inverted Scanning Microwave Microscope. In (a), the AFM probe performs a one-port microwave measurement, which suffers from parasitic interaction between the probe body and the surrounding ground. The parasitic interaction increases when the probe is immersed in saline solution. In (b), the input and output ports of a slot line are part of the sample holder and perform a two-port microwave measurement. The parasitic interaction between the probe body and the surroundings is minimized because the probe is grounded like the grounded electrodes of the slot line.

is immersed in the saline solution because the solution has much higher dielectric permittivity than air. Moreover, the usage of resonant circuits to boost the sensitivity of an SMM amidst the parasitic interaction precludes broadband spectroscopy.

Typically, an SMM is modified from an STM or an AFM, as depicted in Fig. 4.1 (a). In either case, the microwave signal is injected through the probe by a microwave generator or a vector network analyzer (VNA), and the signal reflected from the sample is also sensed by the VNA. The ratio of the reflected and injected signals (the reflection coefficient) can be used to determine the spreading resistance or dielectric permittivity of the sample, after proper calibration and analysis. Such a one-port reflection measurement usually has a dynamic range of 40–60 dB.

To minimize the parasitic interaction and to boost the SMM sensitivity without resorting to a resonance circuit, we have proposed a tool called an inverted SMM (iSMM). As shown schematically in Fig. 4.1 (b), in an iSMM, the scanning probe is always grounded, and the microwave signal is injected through a transmission line such as a slot line or a Coplanar waveguide (CPW) as part of the sample holder. For high sensitivity, it is preferable to concentrate the sample on the centre electrode of the CPW or the excited electrode of the slot line. Unlike the traditional SMM probe, the transmission line can have a broadband impedance match over many decades of

frequency [92].

The input and output of the transmission line are connected to the VNA, so that both reflection and transmission coefficients are measured. Such a two-port measurement usually has a dynamic range of 120–140 dB, which makes it easier to sense the tiny perturbation when the probe scans across the sample. According to the reciprocity theory of electromagnetics, the intrinsic interaction between the probe tip and the sample is the same whether the microwave signal is injected through the probe or the sample. However, with the microwave signal injected through the sample and the probe being grounded, the parasitic interaction between the probe body and the surroundings is greatly reduced, because most of the surroundings are grounded in any case.

Thus, compared with a traditional SMM, an iSMM can have a wider dynamic range, higher sensitivity, and a broader bandwidth (by rendering a resonance circuit unnecessary). Additionally, the probe can be a simple, rugged, and bio-compatible metal stylus. Meanwhile, whether the iSMM is modified from an AFM or STM, the original AFM or STM function is intact so that an iSMM image can be obtained simultaneously with an AFM or STM image. However, in an iSMM the size of the sample is now limited to the waveguide dimension. Moreover, the sensitivity depends on the line position, because of the varying electric field across and along the microwave line.

2.2 Experimental setup

The iSMM is based on a Keysight Technologies 7500 AFM and a home-made sapphire sample holder with a built-in slot line, as shown in Fig. 4.2. The sapphire holder is $2.4 \times 2.4 \times 0.03$ cm^3. The slot line is made of 1.2-μm-thick gold with 80-μm-wide lines and a 10-μm-wide gap between the lines. The lines run across the sapphire holder and are terminated in SMA connectors at both ends. The SMA connectors are connected via coaxial cables to the two ports of a 10 MHz–20 GHz Agilent N5230A PNA-L VNA. Both the reflection coefficient S_{11} (S_{22}) and transmission coefficient S_{21} (S_{12}) of the microwave signal are measured by the VNA. The probe, a Rocky Mountain 12Pt400A metal stylus specially designed for SMM applications with 20-nm nominal tip radius is electrically grounded for iSMM. The probe has a spring constant of 0.3 N/m, which is soft enough for contact-mode scanning on most materials.

Note that iSMM is equally effective in minimizing the parasitic interaction whether

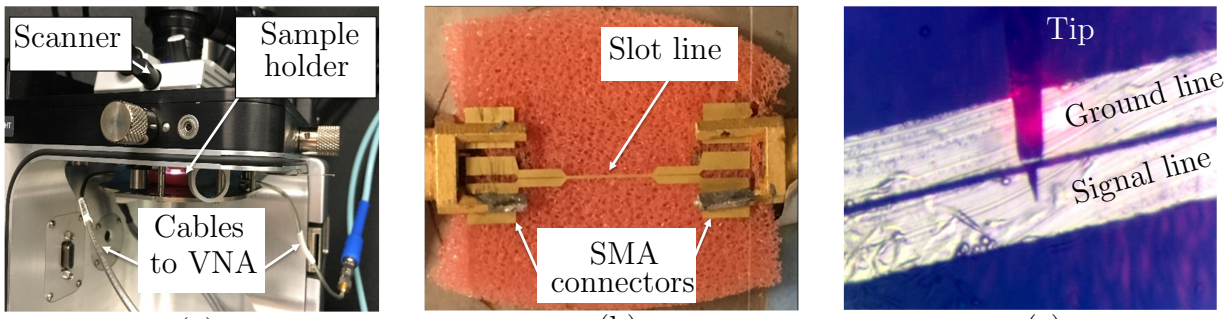

(a) (b) (c)

Figure 4.2

Photograph of the sample chamber of a commercial Atomic Force Microscope retrofitted with a home-made sample holder for inverted Scanning Microwave Microscope (iSMM). (b) Photograph of the sample holder with a built-in slot line terminated in SMA connectors. (c) Micrograph of the iSMM probe scanning across live L6 cells on top of the slot line.

the sample is placed on a slot line as seen in Fig. 4.2 (b,c) or a coplanar waveguide [11]. This is because in the former case we usually approach the sample from the side of the grounded electrode of the slot line, so that the probe body overlaps mainly with the grounded electrode.

Section 3

In-vitro imaging of biological cells

3.1 Cells preparation

To demonstrate the technique, we used an AFM-based iSMM on dried Jurkat human lymphocyte cells and live L6 rat myocyte cells. L6 cells were dispensed onto the sapphire sample holder imprinted with the slot line and cultured in a petri dish for more than 24 hours under 37 °C and 5% CO_2 in DMEM medium containing 10% FBS and 1% penicillin-streptomycin.

For live samples, the sample holder was transferred from the petri dish to the iSMM sample chamber directly. The cells were kept alive in a pool of DMEM medium surrounded by a glue dam. The live cells adhered well to the slot line on the sample holder. For dried samples, the cells were washed by a phosphate-buffered saline solution to decrease salt deposits on the slot line. The cells were then dried in a sterile environment for more than 24 hours. Jurkat cells were similarly prepared except the culture medium was Advanced RPMI 1640 instead of DMEM. Whereas both live and dried L6 cells were probed, only dried Jurkat cells were probed because live Jurkat cells did not adhere to the slot line.

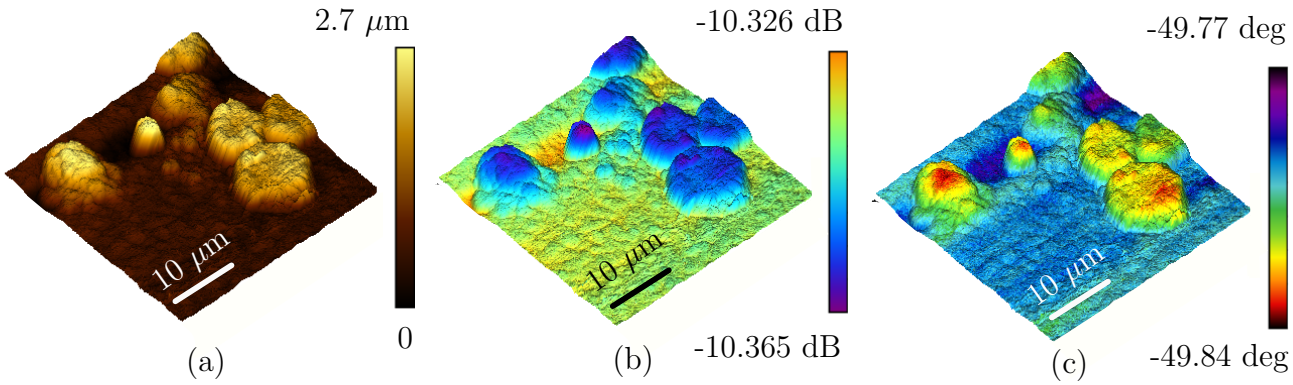

Figure 4.3

Simultaneous (a) Atomic Force Microscopy and (b) amplitude and (c) phase inverted Scanning Microwave Microscopy (iSMM) images of dried Jurkat cells. The iSMM image is based on the reflection coefficient at 4 GHz.

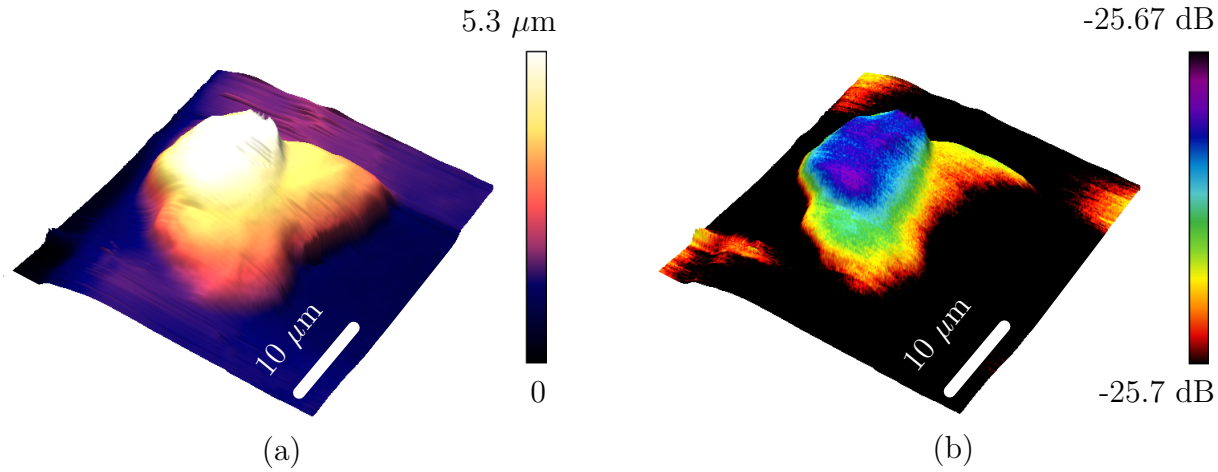

Figure 4.4

Simultaneous (a) Atomic Force Microscopy and (b) inverted Scanning Microwave Microscopy (iSMM) images of a live L6 cell in saline solution. The iSMM image is based on the magnitude of the transmission coefficient at 3.4 GHz.

3.2 A set of experimental results on biological samples

Fig. 4.3 compares the AFM and iSMM reflection images of dried Jurkat cells. It can be seen that the quality of the iSMM image is at least as good as that of the AFM image, both for magnitude and phase coefficients. Moreover, Fig. 4.4 compares the AFM and iSMM transmission images of a live L6 cell in saline solution. The main difference between AFM and iSMM is that iSMM is sensitive to the properties of intracellular structures below the surface. The iSMM image is also among the best quality images formed by the transmission coefficient measured by a two-port SMM [93, 94].

Section 4

Theoretical model of the microscope

The next paragraphs propose an iSMM two-ports equivalent circuit that provides the mathematical foundation of two calibration algorithms, respectively for reflection and transmission measurements, opening the way to the quantitative local electrical characterization of samples. In this context, finite-element simulations provide numerical evidence of the iSMM sensitivity to sample properties variations. Moreover, the model reproduces all imaging and calibration steps, starting from the raw data acquisition up to the extraction of local sample properties, validating the proposed de-embedding techniques.

4.1 Equivalent circuit and calibration of measurements

Fig. 4.5 shows the equivalent circuit of the iSMM. The two ABCD matrices connected to VNA ports 1 and 2 (generally assumed non-symmetrical and non-reciprocal for the sake of generality) represent the input and output error boxes; they embed all the effects related to cables, connectors, VNA, and any non-local tip-sample interactions, including non-ideal probe grounding. Note that no hypothesis is done about the matching of the iSMM transmission line. Error boxes are of course frequency-dependent. The perturbation induced by the grounded probe affects the reflected and transmitted signals at the input and output of the line. Consequently, the equivalent circuit of the tip-sample system is the admittance Y shunting the slot line. Note that the circuit representation of Fig. 4.5, as well as the local admittance of the sample, are independent of the sample position along the line. Strictly speaking, error matrices will generally vary depending on it, hence during a scan. While in small areas of scan this effect is completely negligible, in larger areas it can induce a smooth variation in images, appearing as an artefact similar to plane tilt in AFM and STM images, as we will see in simulations. Those artefacts are corrected as in AFM by subtracting a polynomial fitting curve. Note that even in any standard SMM a similar effect appears as a result of the displacement of the probe or the sample during the scan.

In this model S_{11} and S_{21} are the raw reflection and transmission parameters measured by the VNA. To relate the raw scattering parameters to Y, the full ABCD network between port 1 and 2 of Fig. 4.5 is computed. The product of the three separated ABCD matrices (including the load) gives the total network, being in a

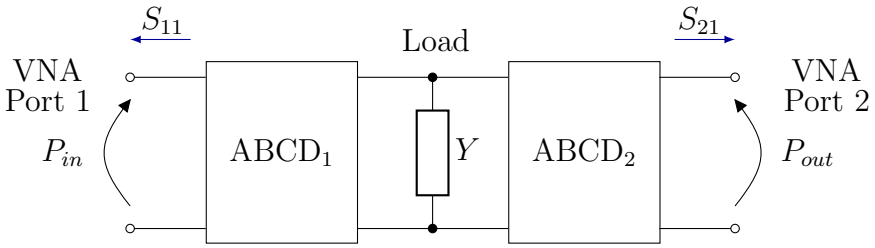

Figure 4.5

Inverted Scanning Microwave Microscope two-port equivalent circuit with an indication of ABCD input (1) and output (2) error matrices and local tip-sample admittance Y.

cascade configuration:

$$\begin{aligned} \text{ABCD} &= \begin{bmatrix} A & B \\ C & D \end{bmatrix} = \begin{bmatrix} A_1 & B_1 \\ C_1 & D_1 \end{bmatrix} \begin{bmatrix} 1 & 0 \\ Y & 1 \end{bmatrix} \begin{bmatrix} A_2 & B_2 \\ C_2 & D_2 \end{bmatrix} = \\ &= \begin{bmatrix} A_1A_2 + B_1C_2 + B_1A_2Y & A_1B_2 + B_1D_2 + B_1B_2Y \\ C_1A_2 + D_1C_2 + D_1A_2Y & C_1B_2 + D_1D_2 + D_1B_2Y \end{bmatrix} \end{aligned} \tag{4.1}$$

Then, existing conversion formulas retrieve the scattering parameters from the total ABCD matrix [11].

Considering the S_{11} case (or similarly S_{22}), the conversion expression gives:

$$S_{11} = \frac{A + By_0 - C/y_0 - D}{A + By_0 + C/y_0 + D} \tag{4.2}$$

where y_0 indicates the VNA reference admittance. With few algebraic manipulations, Eq. 4.2 is rewritten as

$$S_{11} = \frac{\delta + \gamma Y}{\phi + Y} \tag{4.3}$$

where δ, γ and ϕ are a function of input and output error networks only and do not depend on the load. Eq. 4.3 indicates that the reflection parameter depends on Y through three unknown coefficients. Thus, for reflection measurements, the two ABCD matrices reduce into a single error network $\overline{\overline{\boldsymbol{S}^{(e)}}}$ to form a single-port circuit, as already shown in Fig. 1.6. This is independent of the kind of termination for port 2, which can be even reactive, *e.g.* to purposely induce a resonant behavior, providing an additional freedom degree. This implies that calibration methods for the standard reflectometric SMM setups [49] apply to iSMM in the one port configuration without

modification.

On the other hand, transmission mode measurements need a specific calibration approach. The S_{21} parameter (here called T for simplicity) is found with conversion formula from 4.1:

$$S_{21} = T = \frac{2}{A + By_0 + C/y_0 + D} \tag{4.4}$$

Then, terms that include the local admittance Y are grouped and Eq. 4.4 is rewritten as:

$$T = \frac{2}{\alpha + \beta Y} \tag{4.5}$$

where α and β only depend on error networks. At this point, Eq. 4.5 is inverted to retrieve the local admittance:

$$Y = \frac{2/T - \alpha}{\beta} \tag{4.6}$$

Eq. 4.6 shows the transmission mode calibration requires to quantify the coefficients α and β. This is done by measuring T for two known tip-sample loads used as a reference. In particular, if we call T_1 and T_2 the transmission coefficients for the load Y_1 and Y_2, the following linear system holds

$$\begin{cases} T_1 = 2/(\alpha + \beta Y_1) \\ T_2 = 2/(\alpha + \beta Y_2) \end{cases} \tag{4.7}$$

and α and β are found:

$$\begin{cases} \alpha = 2\dfrac{Y_2/T_1 - Y_1/T_2}{Y_2 - Y_1} \\ \beta = \dfrac{2/T_1 - \alpha}{Y_1} \end{cases} \tag{4.8}$$

The known loads Y_1 and Y_2 can be the local tip-sample admittance over a reference conductive plane at two different distances, whose values are inferred by geometrically modeling the tip as a conductive sphere and cone over a metal ground. In our measurements we used directly the gold metal of the transmission line, neglecting associated losses.

To summarize, by acquiring S parameters at different probe-ground distances

(approach curve), calibration coefficients are obtained by the previous equations. Once coefficients are known, S parameters recorded at different distances can be calibrated. Such a step tests the correctness of the calibration since the calibrated curve should follow the expected behavior for the cone+sphere admittance over a ground. If the test is successful, calibration coefficients can be used to retrieve calibrated data also for a complete scan, point-by-point. At this point, regardless we operated in reflection or transmission mode, we have obtained calibrated integral quantities related to the sample, namely conductance and susceptance. Further processing is needed to derive electromagnetic local properties, such as dielectric constant and conductivity, from those integral quantities. Incidentally note that while integral quantities are strongly dependent on the assumed geometrical parameters, derived local properties are not; the latter result to be variational properties with respect to the geometrical parameters. For clarity, the main steps of the complete process are described below:

1. Image acquisition;
2. Approach curve acquisition on top of a highly conductive area;
3. Evaluation of calibration coefficients from the approach curve by representing the tip as a conductive sphere and cone over a metal ground, in such a way that the calibration loads can be found analytically;
4. Calibration of the approach curve and comparison with the analytical tip-sample admittance to verify the success of the calibration;
5. Calibration of the acquired image and extraction of the tip-sample local admittance;
6. Extracting electromagnetic properties of the sample from the calibrated tip-sample admittance using numerical/analytical models.

4.2 The local tip-sample interaction

The shunt admittance Y in the iSMM schematic of Fig. 1.6 models the tip-sample near-field local interaction. Different equivalent circuits of the tip-sample system can be used, and the model to choose mainly depends on the operating mode and degree of accuracy of the representation [13, 17, 30–32, 35, 40]. Fig. 4.6 (a) shows a simple equivalent circuit representing Y for non-contact mode operation, where a homogeneous sample and a conical tip with a spherical apex indicate the geometry.

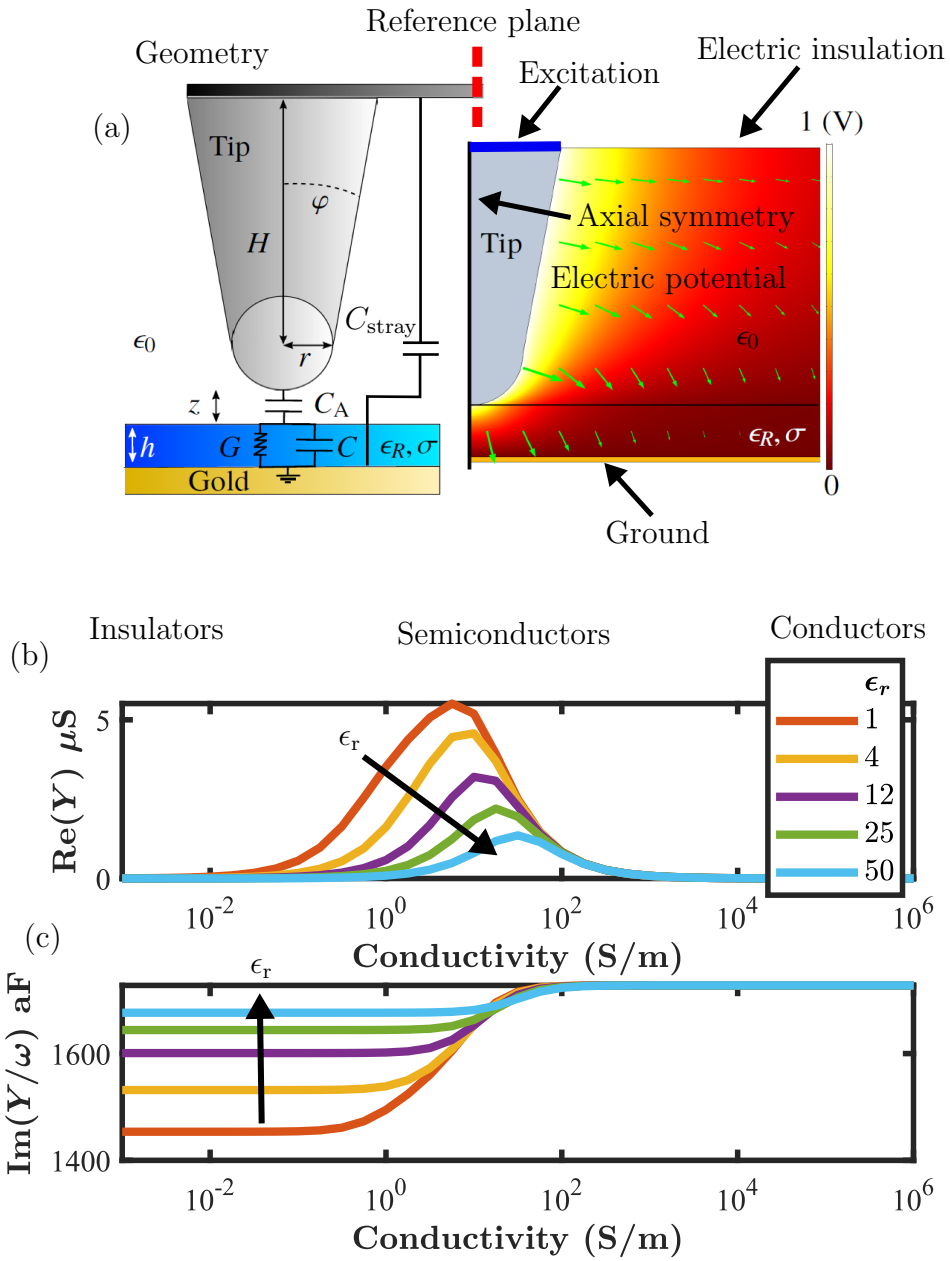

Figure 4.6

Probe-sample geometry with cone height $H = 50$ μm, half cone angle $\varphi = 5°$, tip radius $r = 1$ μm, tip-sample distance $z = 5$ nm, and sample thickness $h = 1$ μm and indication of reference plane. The equivalent circuit is overlaid on the geometry, in which G, C, C_A, and C_{stray} represent respectively the local sample conductance, sample capacitance, air capacitance, and cantilever capacitance. Typical potential and field distributions are beside the geometry. Quantities are computed with a two-dimensional COMSOL® axisymmetric model (AC/DC module), and Fig. (a) indicates the axial-symmetry boundary condition (BC), electric insulation BC at the open boundaries, ground BC below the ground plate, and electrical excitation contact. (b) Simulated Re(Y) and (c) Im(Y)/ω at 8.5 GHz as functions of sample conductivity σ and dielectric constant ϵ_r.

The sample conductance G and capacitance C represent the sample equivalent parameters that depend on local sample conductivity σ and dielectric constant ϵ_r respectively, while C_A is the air capacitance.

Overall, G, C, and C_A compose the tip-sample local admittance Y, and from the series of the air and sample contributions, the real and imaginary part of Y are obtained:

$$\mathrm{Re}(Y) = \frac{\omega^2 G C_A^2}{G^2 + \omega^2 (C + C_A)^2} \tag{4.9}$$

$$\mathrm{Im}(Y/\omega) = \frac{C_A (G^2 + \omega^2 C (C + C_A))}{G^2 + \omega^2 (C + C_A)^2} \tag{4.10}$$

COMSOL® Multiphysics (RF-module) finite-element simulator allows the direct evaluation of $\mathrm{Re}(Y)$ and $\mathrm{Im}(Y)$ as functions σ and ϵ_r. Fig. 4.6 (b) and Fig. 4.6 (c) respectively show the $\mathrm{Re}(Y)$ and $\mathrm{Im}(Y)$ for different combinations of σ and ϵ_r, indicating the microscope sensitivity to the local sample properties change. First, both $\mathrm{Re}(Y)$ and $\mathrm{Im}(Y)$ are independent of ϵ_r if σ is sufficiently high. Moreover, without the sample, as well as when the sample is strongly conductive, C_A dominates Y and $\mathrm{Re}(Y) \approx 0$. In this case, the end part of the tip can be approximated as a point-ball sphere on top of a metallic plane, and the recursive expression in [95] provides the theoretical apex capacitance with a certain tip-metal separation, used to evaluate the capacitance standards for the microscope calibration as already explained in the previous section. Note that in general, the condition $\mathrm{Re}(Y) \approx 0$ will not be valid when the air is replaced by a liquid or a lossy gas.

On the other hand, for contact mode operation, owing to the absence of C_A, results differ since the conical part of the tip interacts in the air with the sample, adding a new set of elements in parallel with the previous ones. It should be stressed that contact mode is not always suitable, because of some additional unwanted effects (*e.g.* interface metal/semiconductor diode-like effects, cross-contamination, wearing phenomena during the scan, etc.).

When modeling the tip-sample system, non-local interactions should be also considered, such as the capacitance between the tip cantilever and the sample, often called stray capacitance C_{stray} shown in Fig. 4.6. To keep in C_{stray} only the part of the capacitance that varies with the cantilever/ground distance, it is defined as a difference with respect to the value assumed in the farther position in the approach curve

$$C_{\mathrm{stray}} = -c_{\mathrm{stray}}(z - z_0) \tag{4.11}$$

where z indicates the tip-ground plane separation, c_{stray} is the capacitance per unit distance [48] and z_0 is a reference position, in our figures $z_0 = 2$ μm. The error matrices of Fig. 4.5 include errors related to the non-local probe-ground coupling, not depending on the z-position of the probe. The cantilever contribution generally dominates the tip-sample interaction when the two are far away, and the only local coupling is not sufficient to represent the tip-sample interaction.

Section 5

Full-wave finite element model of the microscope

5.1 Sensitivity of the microscope

To numerically investigate the iSMM sensitivity to sample electromagnetic properties changes, we have implemented a COMSOL® Multiphysics (RF-module) numerical model, reproducing all the iSMM scanning operations. The three-dimensional model reproduces the iSMM geometry of Fig. 4.1 (b), including the conductive AFM tip (grounded), slot line, and sample. Two lumped ports connected between the signal and ground line excite the waveguide and collect the reflected/transmitted signal. In the experimental setup, slot line and coaxial connectors are capacitively coupled, making the system mismatched with respect to the 50 Ohm line impedance. To mimic this effect in simulations while keeping the computational load low, lumped ports employ an internal impedance different from 50 Ohm (an arbitrary value of 300 Ohm is chosen). "Scattering boundary conditions" are enforced to the exterior boundary in COMSOL®, to avoid reflections from boundaries. Fig. 4.7 shows a full view of the model as well as a profile of the electric field distribution along the slot line.

In the simulation, the horizontal and vertical movement of the tip mimics the iSMM scan operation. To avoid topographic artifacts caused by the z tip position change (topography crosstalk), the tip scans a flat sample with local differences in electrical properties: three square bricks of SiO_2, doped Si and SiO_2 compose the sample (Fig. 4.8 (a)) and the probe travels along the y-axis at a constant distance (5 nm along z-axis) with respect to the sample.

Fig. 4.8 (c) and 4.8 (d) show the transmission and reflection coefficients recorded at each tip position. As expected, a contrast between different material regions appears due to the local physical properties change. From the circuital point of view, the load admittance of Fig. 4.5 changes when the tip moves from SiO_2 to Si and the scattering parameters sense this change. The rounded profile shapes of S_{11} and

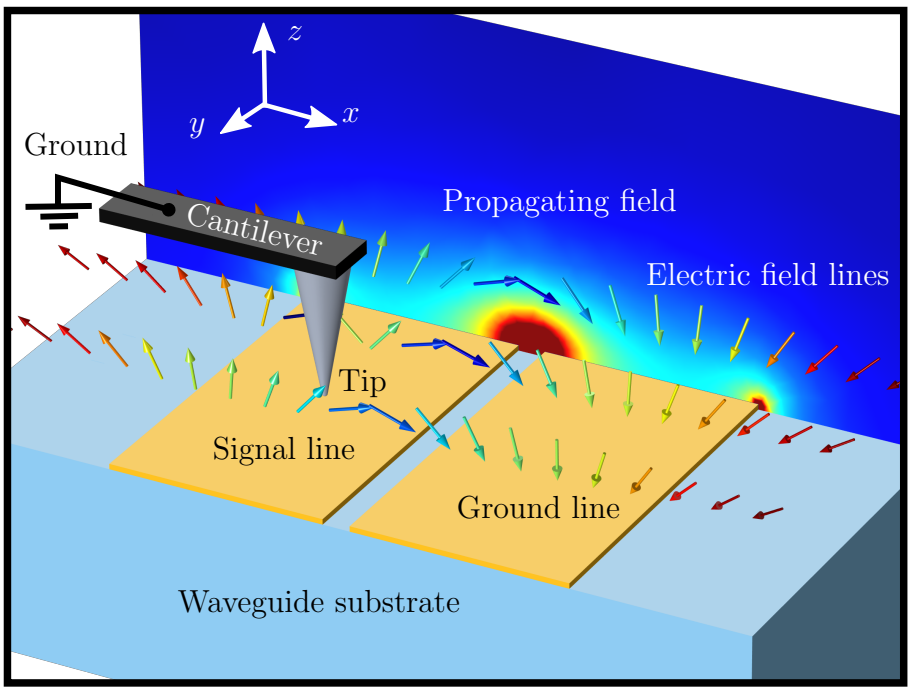

Figure 4.7

Three-dimensional COMSOL® model of inverted Scanning Microwave Microscope, with indication the propagating electric field norm and the electric field lines. The waveguide parameters are the same as experimental setup and the tip geometry is defined according to the values of Fig. 4.6.

S_{21} are caused by the so-called "convolution effect", arising from the finite spatial size of the electromagnetic field cloud around the tip apex; here the phenomenon is particularly evident due to the thick sample and the large tip radius.

The phase of S_{11} in Fig. 4.8 (d) presents an apparent tilt when the tip moves along the y-axis and it is due to the change of the tip position across the line. In fact, the field can be non-uniform in the cross-section due to the structure of the transmission line, and possibly non-uniform along the longitudinal direction if standing waves exist, *i.e.* the transmission line is mismatched. Standard line leveling, as used in AFM, removes the artefact and recovers the correct contrast between regions with the same electrical characteristic. In experimental sessions, the scanning probe microscopy (SPM) software performs this operation in real-time using a first-order correction (commonly called plane removal).

The results of Fig. 4.8 numerically show the ability of iSMM in detecting spatial points of the sample with different electrical properties. Note that the sensitivity of iSMM, now intended as the absolute variation between S parameters measured in points with different electrical properties, depends on many factors: they in-

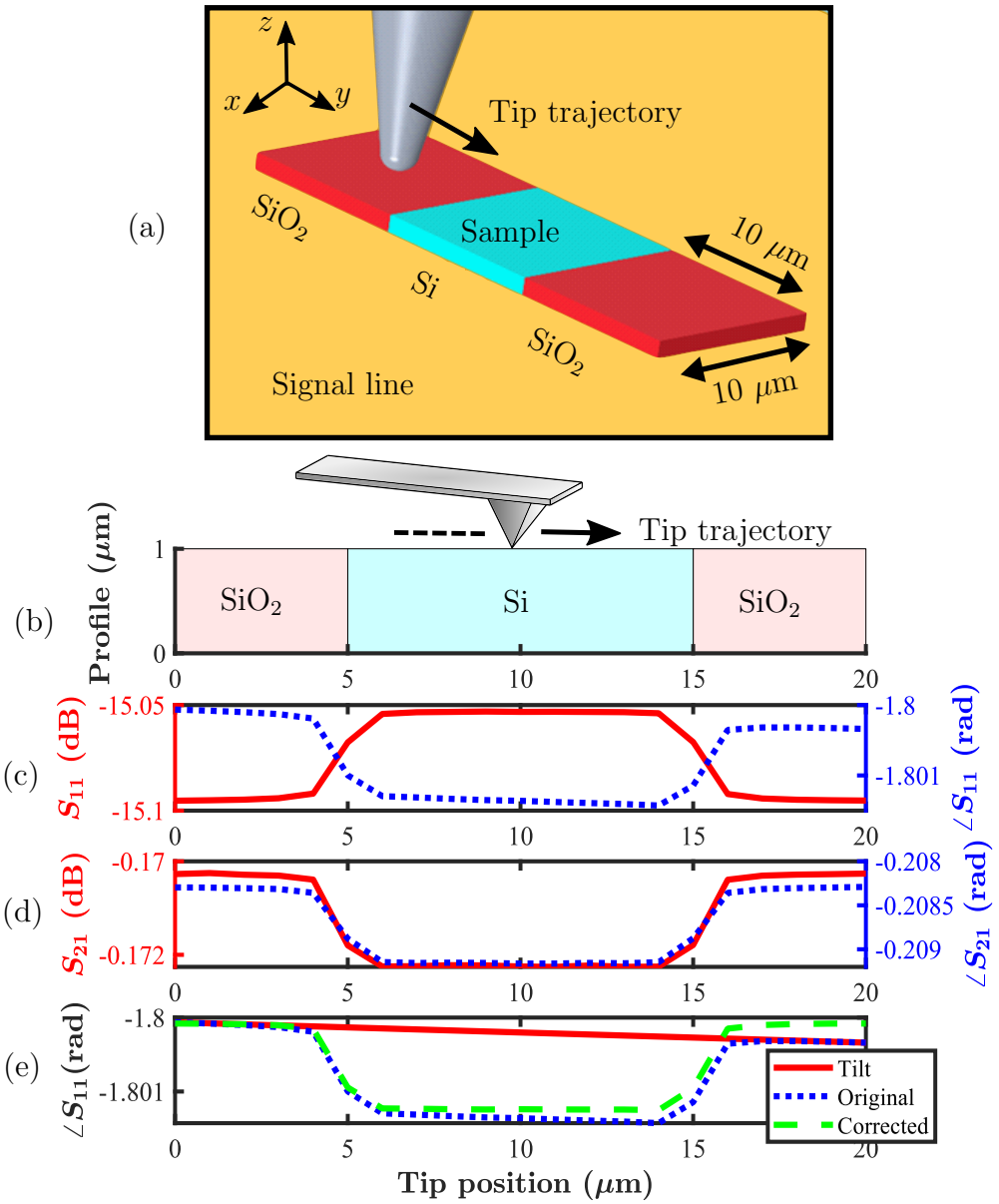

Figure 4.8

(a) COMSOL® geometry of the simulated microscope scanning operation, in which three SiO_2 and doped-Si bricks compose the sample. (b) Height profile of the flat sample with an indication of the material composition. (c) Raw S_{11} and (d) S_{21} parameters (amplitude and phase) collected at the input and output port during the y-scan. (e) Correction of S_{11} phase tilt with a first-order correction and indication of raw and corrected phase, as well as the removed trend. The doped Si has a dielectric constant $\epsilon_r = 11.68$ and a conductivity of $\sigma = 100$ S/m, SiO_2 has $\epsilon_r = 4.2$ and $\sigma = 0$ S/m, and the simulation is performed at 8.5 GHz.

clude operating frequency, sample position on the signal line, and amount of line impedance mismatch with the ports. However, optimizing microwave scanning operating conditions is beyond the scope of this work.

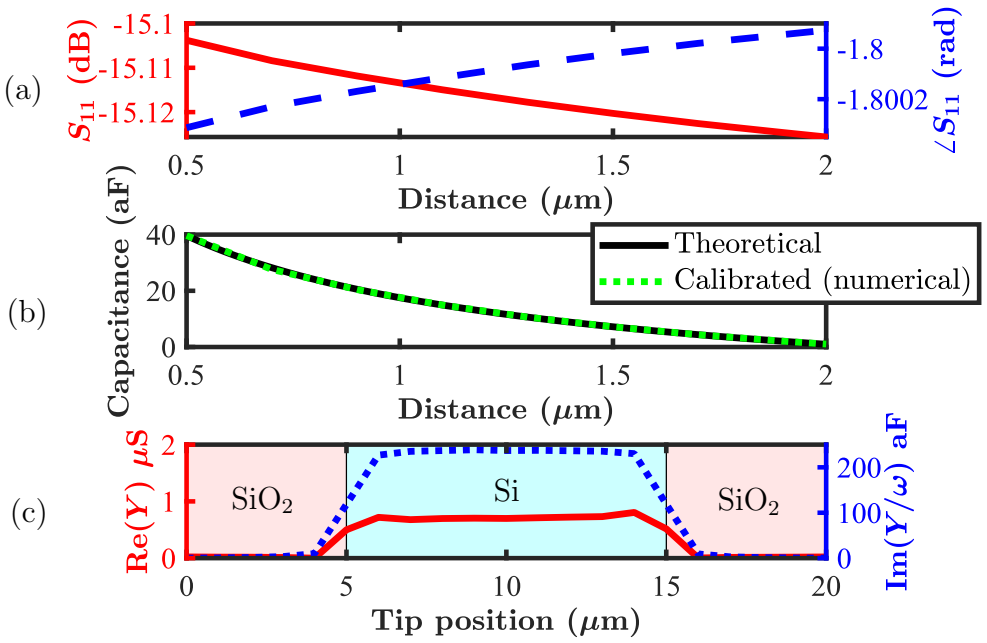

Figure 4.9

(a) Simulated reflection coefficient S_{11} (amplitude and phase) of the inverted Scanning Microwave Microscope approach curve on the bare signal line at 8.5 GHz. (b) Calibrated capacitance approach curve compared to the analytical model. (c) Calibrated real and imaginary part of admittance (contrast) of simulated sample scan across a SiO_2/Si/SiO_2 sample.

5.2 Reflection mode calibration

The simulation model here verifies the concept of iSMM single port calibration already explained in the previous paragraphs. Steps for calibration described in Sec. 4.1 are applied to the numerical raw data. The process starts with the evaluation of the simulated S_{11} approach curve over the bare transmission line, and this value is converted to a capacitance curve, as shown in Fig. 4.9 (a) and (b) [49]. This numerical capacitance is compared to the capacitance calculated by the analytical model, where the probe is approximated by a sphere approaching a ground plane [95] summed to the contribution from the cantilever, again computed analytically [48]. The total theoretical tip-ground capacitance is $C_{\text{cross}} = C_{\text{sphere}} + C_{\text{stray}}$. The analytical model employs the nominal radius of the tip ($r = 1$ μm), while $c_{\text{stray}} = 10^{-11}$ F/m is selected to best fit the calibrated curve obtained numerically.

Note that in this virtual experiment, the direct comparison of the simulated curve with the analytical capacitance is sound, because the in-air conductance is negligible, and the numerical admittance is (almost) purely capacitive. Fig. 4.9 (b) indicates an excellent agreement between the numerical and modeled approach curves across the

entire range of probe-sample distances.

During the process, the error matrix of the reduced equivalent iSMM circuit of Fig. 1.6 (a) is evaluated and used to calibrate the reflection data obtained from the simulated scan. Fig. 4.9 (c) shows the numerical real and imaginary part of the local admittance on the sample obtained after calibration: as expected, the doped-Si region shows higher Re(Y) and Im(Y) because its conductivity and dielectric constant are higher than that of the SiO_2 area. On the other hand, the gradual increase of Y from SiO_2 to Si is due to the aforementioned probe/sample convolution effect.

It is important to note that calibrated data on Si and SiO_2 show the correct contrast even if during the calibration we assume a tip radius that differs from the one used in the simulation. In fact, a tip-radius change during the calibration corresponds to a reference plane shift [49] and calibrated quantities scales accordingly. This may be important when retrieving local admittance values from measurements due to the not perfect knowledge of the (effective) tip-radius, which commonly changes during the operation.

5.3 Transmission mode calibration and sample properties extraction

The numerical model used in the previous section here validates the calibration protocol for transmission mode. In this case, the sample is a single doped Si square brick (depicted in Fig. 4.10) composes the sample, with lateral dimensions of 10×10 μm, 1 μm thickness, and homogeneous electrical properties ($\epsilon_r = 11.68$ and $\sigma = 1$ S/m). The tip scans with a constant tip-sample interaction in non-contact mode, *i.e.* by maintaining a tip-sample distance of 5 nm both on top of the sample and ground line, as described by the tip trajectory in Fig. 4.11 (a) (which also reproduces the sample profile).

Fig. 4.11 (b) illustrates the recorded S_{21} coefficient obtained numerically, in which the blue area represents the sample region and the red areas indicate points in which the tip is on air (5 nm distant from the signal line). Here, the S_{21} contrast between red and blue regions is now due not only to the presence of the sample with defined electrical properties but also to the tip vertical movement (topography crosstalk). Hence, this numerical simulation also accounts for the most common source of artefacts.

The calibration follows the protocol described in Section 4 for the transmission case: Fig. 4.12 (a) depicts the numerical approach curve taken on the bare signal line, and Fig. 4.12 (b) shows the calibrated capacitance values of the simulated curve.

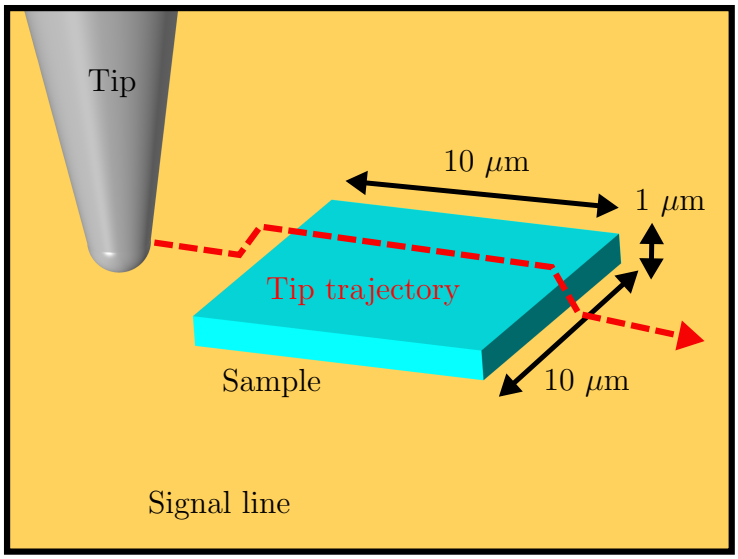

Figure 4.10

Simulated inverted microscope scanning operation with a constant tip-sample interaction (corresponding to a constant tip-sample distance). A doped-Si square brick positioned on the signal line composes the sample, with dimensions of 10×10×1 μm, dielectric constant $\epsilon_r = 11.68$ and electrical conductivity $\sigma = 1$ S/m. The red arrow indicates the tip trajectory that follows the sample profile.

Again, the accordance between the numerical and analytical curves indicates the success of the procedure. The extracted α and β coefficients of Eq. 4.8 are used to calibrate the simulated S_{21} data taken on the sample, and Fig. 4.11 (c,d) show the calibrated admittance. The imaginary part $\mathrm{Im}(Y)/\omega$ indicates a negative contrast between air and sample, due to the increased tip-signal line distance when the tip moves from the air region to the sample area. On the contrary, $\mathrm{Re}(Y)$ shows a positive contrast due to the presence of a sample with non-zero conductivity.

Fig. 4.13 (a) shows a three-dimensional full-wave model of the only tip-sample system (without any slot line) used to verify the results of calibration, including the effect of topography crosstalk. The model is based on COMSOL® AC/DC module that allows the direct extraction of the local tip-sample admittance and employs identical tip and sample parameters used for the iSMM case. However, here the sample is deposited on a simple metal substrate, and the microwave excitation is applied directly on the tip (such as in a reflectometric SMM) that mimics the same scanning operation of Fig. 4.10. Fig. 4.13 (b) reports the obtained $\mathrm{Re}(Y)$ and $\mathrm{Im}(Y)/\omega$, showing the same behaviour of the calibration results of Fig. 4.11 (c,e) for the iSMM case. Basically, standard and inverted SMM provides similar behaviour.

The calibrated admittance Y needs to be processed to extract intrinsic sample electrical parameters because it also depends on the system geometry. In particular,

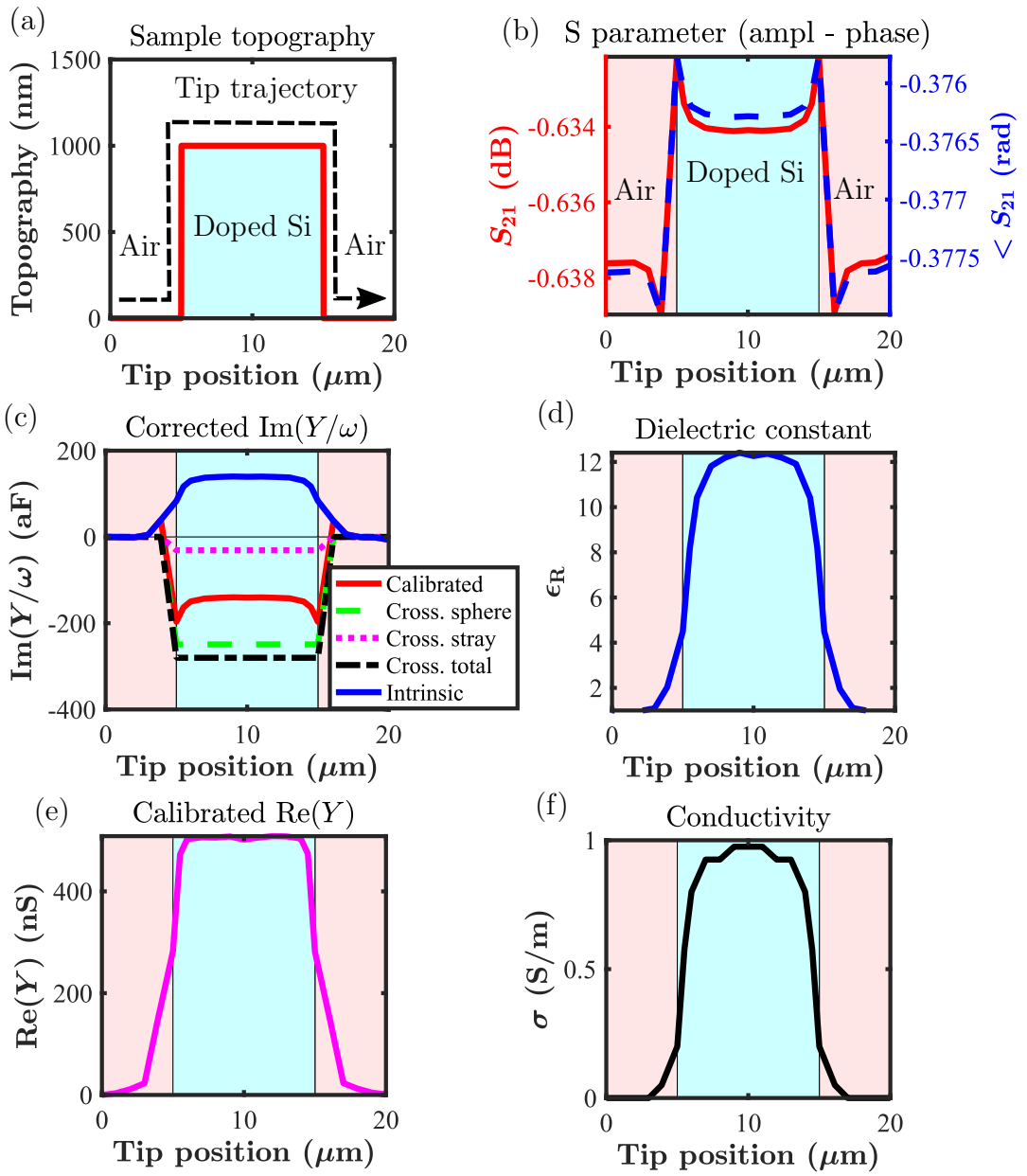

Figure 4.11

(a) Doped-Si ($\epsilon_r = 11.68$ and $\sigma = 1$ S/m) sample profile with indication of the tip-trajectory. (b) Recorded transmission coefficient (amplitude and phase) at 10 GHz. (c) Calibrated $\mathrm{Im}(Y)/\omega$, crosstalk contribution from tip apex and cantilever, total crosstalk, and topography corrected $\mathrm{Im}(Y)/\omega$ (obtained from the difference of calibrated $\mathrm{Im}(Y)/\omega$ and the total crosstalk contribution). (d) Sample dielectric constant obtained from the intrinsic $\mathrm{Im}(Y)/\omega$ with an analytical model. (e) Calibrated $\mathrm{Re}(Y)$ and (f) sample conductivity evaluated from $\mathrm{Re}(Y)$) through a minimization procedure with the two-dimensional COMSOL® model.

the local dielectric constant is derived from the calibrated $\mathrm{Im}(Y)/\omega$ by a proper correction of the topographic effect. The topography crosstalk contribution C_{cross} is defined as the capacitance between the tip and the metal ground when their distance

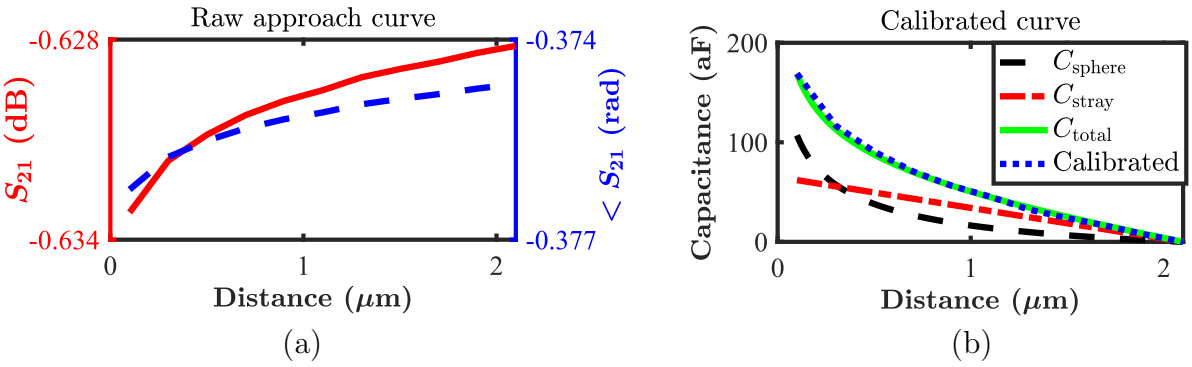

Figure 4.12

(a) Simulated S_{21} amplitude and phase of the approach curve on the bare signal line at 10 GHz. (b) Calibrated capacitance approach curve compared to the analytical model, formed by the tip (sphere) and cantilever (stray) contributions.

corresponds to the sample height. In other words, C_{cross} is the capacitance obtained when the tip scans only on air but with the same topography of the real sample. Following the definition of [48], the sample dielectric constant is obtained from the difference between the calibrated $\text{Im}(Y)/\omega$ and the topography crosstalk contribution C_{cross}:

$$\epsilon_{\text{r}} = \text{e}^{\dfrac{\text{Im}(Y)/\omega - C_{\text{cross}}}{2\pi\epsilon_0 r}} \tag{4.12}$$

Eq. 4.12 applies to poorly conductive materials (corresponding to the left region of Fig. 4.6 (a)), in which the effect of sample conductance is still negligible on the calibrated $\text{Im}(Y)/\omega$ value. In fact, when this effect becomes significant, $\text{Im}(Y)/\omega$ cannot be modelled as a simple capacitor (as shown in Eq. 4.10). Fig. 4.11 (c) shows the intrinsic $\text{Im}(Y)/\omega$, referred as the difference $\text{Im}(Y)/\omega - C_{\text{cross}}$, as well as the crosstalk contributions from apex and cantilever. From the intrinsic value, Eq. 4.12 allows to derive the dielectric constant: the result is shown in Fig. 4.11 (d) and indicates a maximum value around 12 in the sample region, in good agreement with the chosen parameter. Moreover, ϵ_{r} gradually decreases to $\sim$1 in regions outside the sample, *i.e.* where only the air separates the tip and metal electrode.

To extract the sample conductivity we do not have a simple expression; hence the previously described two-dimensional COMSOL® model already shown in Fig. 4.6, can be used to compute the tip-sample $\text{Re}(Y)$ and to compare the results with those obtained in Fig. 4.6 (b,c). This is done through a numerical minimization procedure that automatically searches for the nearest value of conductivity corresponding to the obtained $\text{Re}(Y)$ in a specific spatial point. This way, the point-by-point sample

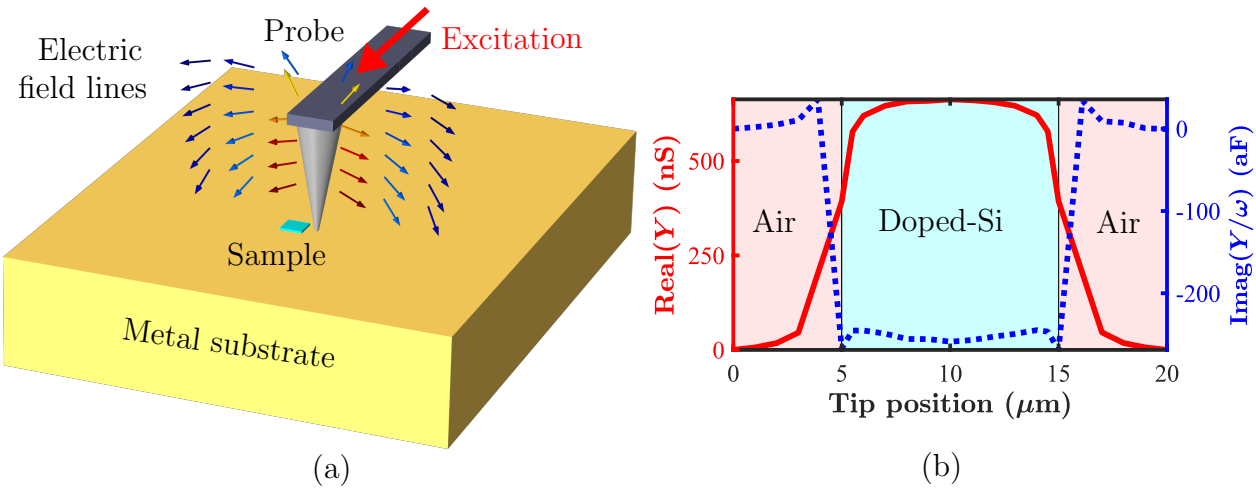

Figure 4.13

(a) Three-dimensional full-wave COMSOL® model (AC/DC module - Electric Currents interface) of the tip-sample system, in which a voltage source excites the tip cantilever, the metal substrate is grounded, and the exterior boundaries of the model employ electric insulation boundary conditions. (b) Tip-sample local admittance in terms of the real part Re(Y) and imaginary part Im(Y)/ω while scanning the sample in contact mode as depicted in Fig. 4.10.

conductivity is mapped similarly to ϵ_r, but using a numerical model. Note that, as clearly visible in Fig. 4.6 (b), Re(Y) depends on ϵ_r in the low conductivity region. This means that to compare the simulated Re(Y) data to those obtained from calibration, the computed ϵ_r must be selected as sample permittivity. This procedure has to be repeated for each spatial point because the permittivity locally changes (as seen from Fig. 4.10). Moreover, due to the non-monotonous behaviour of the Re(Y) with σ, to evaluate σ we have to assume that the sample belongs to the poorly conductive region. On the other hand, for a sample with high conductivity such as metals or semi-metals, the Re(Y) is independent on ϵ_r and there is no need to account for ϵ_r during the minimization procedure.

Fig. 4.11 shows the computed sample conductivity by comparing the calibrated Re(Y) values with those directly estimated from the two-dimensional COMSOL® model of Fig. 4.6 (a). The results show that $\sigma \approx 1$ S/m at the centre of the sample, again in good agreement with the selected value. An important point is that the estimation of the dielectric constant and conductivity is mostly insensitive to the radius assumed for the tip. This happens since we introduce a systematic error in the whole procedure corresponding to a reference plane shift [49], and all the calibrated quantities involved in the process scale accordingly. While integral properties like bipole admittance will be affected by the choice, the resulting material properties

are only weakly dependent on it.

Section 6

Conclusion

In conclusion, we have experimentally demonstrated the iSMM for imaging and characterization on the nanometre scale, which can be applied through a straightforward modification of any scanning probe microscope. The technique is label-free, non-invasive, broadband, and highly sensitive. Moreover, with a simple and rugged metal probe that is always grounded, it can be easily made bio-compatible. Using the iSMM, a live cell in saline solution was imaged, thus the iSMM could potentially broaden the application of SMM beyond the current focus on surface physics and semiconductor technology.

The chapter also explains the conversion of raw iSMM measurements into quantitative sample properties throughout de-embedding procedures. The proposed calibration algorithm for transmission mode takes the advantage of the increased VNA dynamic range in transmission, providing higher measurement accuracy. Additionally, an algorithm previously developed for reflectometric SMM setups has been demonstrated to apply to iSMM operating in reflection mode. The next chapter illustrates the application of these procedures for the experimental characterization of the local electrical conductivity of a Platinum Diselenide ($PtSe_2$) sample, as well as for the measurement of the dielectric constant of a single Jurkat cell.

Chapter 5

Experimental and Quantitative Characterization of Sample Properties

Table of contents

Section 1
Introduction

The inverted Scanning Microwave Microscope (iSMM) presented in the previous chapter here quantifies the local electrical properties of a Platinum Diselenide ($PtSe_2$) sample and a single Jurkat (human lymphocyte) cell. $PtSe_2$ is a transition-metal

dichalcogenide with unique features including sizable bandgap, air stability, and high carrier mobility [96,97] that seems to be among the most relevant competitors of graphene in two-dimensional form. Moreover, it behaves like a semimetal when thicker than a few atomic layers. This facilitates the fabrication of low-resistance ohmic contacts and promotes the application of $PtSe_2$ in electronic devices [98,99]. In this context, Sec. 2 reports the iSMM analysis of the local electrical conductivity of a $PtSe_2$ sample, demonstrating the semi-metal behaviour of the material. Moreover, Sec. 3 shows the quantitative analysis of a single Jurkat cell: the complex local admittance of the cell is extracted and the dielectric constant is estimated to be around 2.6 ± 0.3.

Section 2

Quantitative characterization of Platinum Diselenide electrical conductivity

2.1 Materials, instruments and sensitivity

In this section, the iSMM quantitatively characterizes the conductive properties of some layers of $PtSe_2$, analyzed by using the same iSMM setup already described in Sec. 2.2 of the previous chapter, with the difference that here the Atomic Force Microscopy (AFM) probe is a gold-coated BudgetSensor Tap300GB-G, grounded for iSMM and operating in non-contact mode [2]. Transmission measurements are calibrated throughout the algorithm discussed in Sec. 5.3 of Ch. 4, that takes the advantage of the increased VNA dynamic range providing higher measurement accuracy.

The selected iSMM operating frequency maximizes the Signal-to-noise ratio (SNR) defined in Eq. 1.1. Here is considered the transmission case, thus $S_{21}(z = 0)$ and $S_{21}(z = 3\ \mu\text{m})$ are measured, indicating the transmission coefficients with the probe separated by few nanometres from the slot line and lifted 3 μm in the air, respectively. Each measurement was repeated 500 times and arithmetically averaged to reduce noise. Even if the number of measurements is high, the estimation of SNR takes only a few seconds because the data is taken in a single spatial point. With S_{21} in the vector form in Eq. 1.1, averaging accounts for deviations in both amplitude and phase.

SMM data usually has sufficient quality when the SNR is 15 dB or larger. In the actual setup, Fig. 5.1 shows that $SNR(S_{21})$ peaks at 20 dB around 4.7 GHz, and this frequency was selected in the present S_{21} measurement. Here the bandwidth is

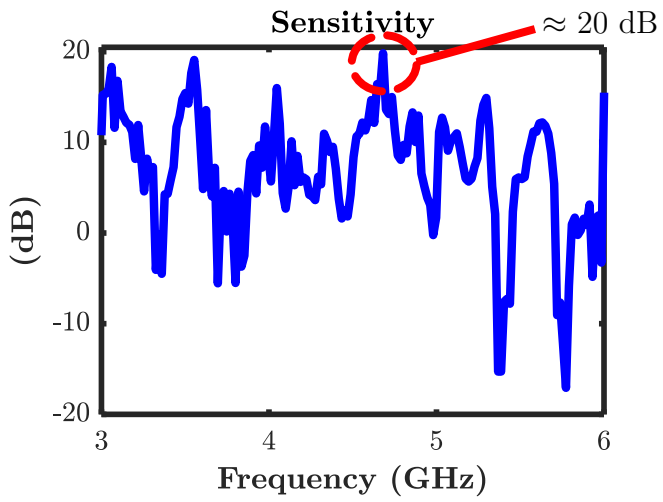

Figure 5.1

Signal-to-noise ratio of inverted Scanning Microwave Microscope operating in transmission mode as a function of frequency.

relatively narrow since, in the present implementation, the slot line was capacitively coupled to the VNA. From the measured S_{21}, the electrical conductivity of a Platinum Diselenide ($PtSe_2$) sample was extracted.

2.2 Transmission images and calibration

$PtSe_2$ was obtained by selenization of sputtered platinum films on a silicon substrate (at 400 °C) [100]. It was then transferred to the iSMM sample holder, agglomerating in flakes of multi-layers $PtSe_2$ on top of the metal substrate (easily recognizable by using the optical microscope, see Fig. 5.2 (a)). Fig. 5.2 shows the raw iSMM S_{21} images at 4.7 GHz (scan area of 13 × 13 μm^2 in 256×256 pixels across two $PtSe_2$ flakes), in terms of amplitude, phase, real, and imaginary part. Fig. 5.2 (b) also shows the simultaneously acquired AFM sample topography: Fig. 5.2 (c) reports a central cross-section and indicates the presence of $PtSe_2$ between x = 8 μm and x = 10 μm. As expected from the sensitivity analysis, the S_{21} images provide good contrast between regions with and without the sample, as also seen in the single line profiles of Fig. 5.2 (f,i).

For calibration, the system acquires the S_{21} approach curve on bare gold without any sample, as seen in Fig. 5.3 (a); the curve is then converted to a capacitance curve, shown in Fig. 5.3 (b), that agrees with the analytical model of a sphere on top of a ground plane (C_{sphere}), including an additional contribution due to the cantilever (C_{stray}). Here, the radius selected for calibration is the nominal value of

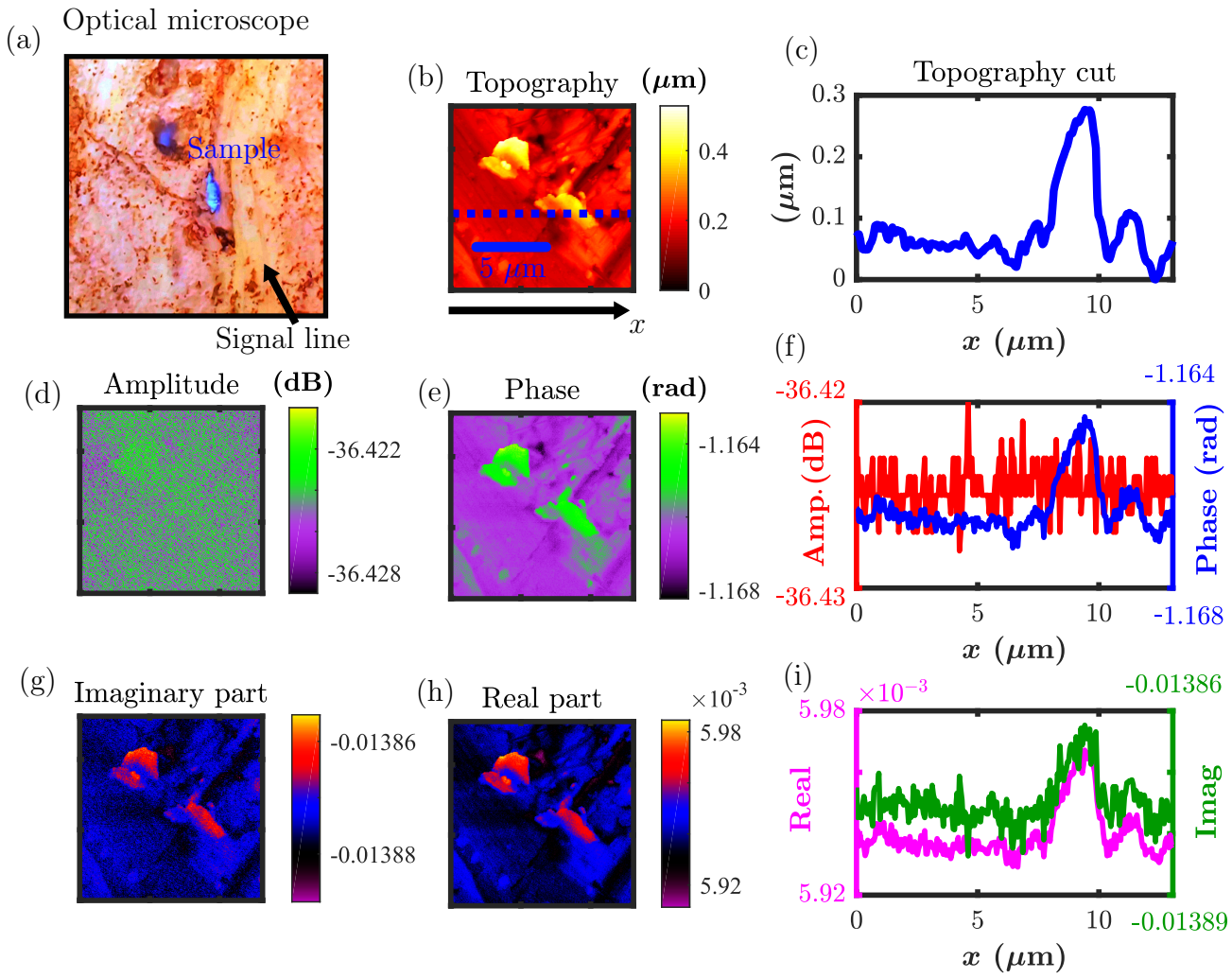

Figure 5.2

(a) Optical micrography of blue-silver Platinum Diselenide ($PtSe_2$) flakes deposited on the high-frequency gold line. (b) Atomic Force Microscope topography of two $PtSe_2$ flakes: yellow regions indicate the presence of the sample and red-black areas correspond to the gold line. (c) Topography cross-section along the dotted line of Fig. 5.2 (b). Corresponding high-frequency data in terms of (d) amplitude, (e) phase, (g) imaginary part, and (h) real part based on S_{21} at 4.7 GHz; the line profiles are shown in Fig. (f) and (i) along the same cross-section as (c).

25 nm from the probe supplier and the stray capacitance fits the approach curve, giving $c_{\text{stray}} = 8\,10^{-13}$ F/m.

The procedure also extracts the α and β error network coefficients to perform the calibration of the whole image of Fig. 5.2. In particular, Fig. 5.4 (a,c) shows the real and imaginary parts (divided by angular frequency) of the calibrated admittance, and Fig. 5.4 (b,d) depicts the corresponding cross-sections along the x-direction. Differential quantities are taken with respect to a spatial point with no sample.

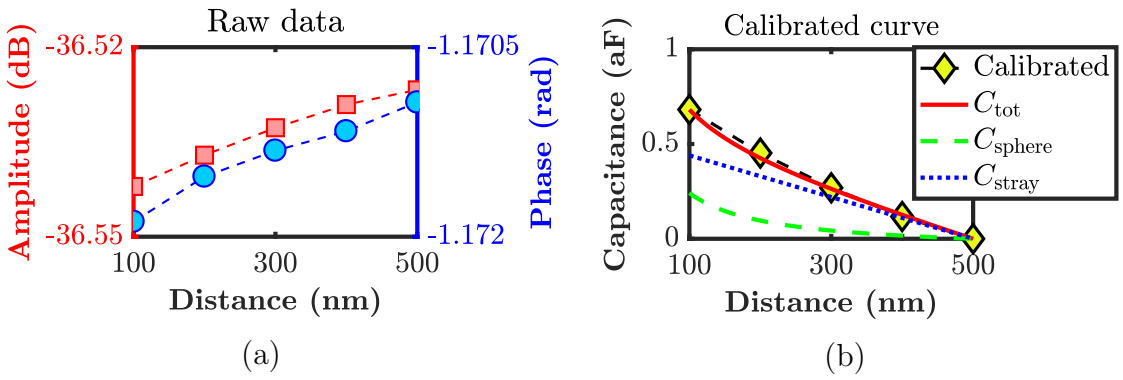

Figure 5.3

(a) Raw S_{21} approach curve on top of the bare gold line at 4.7 GHz (amplitude and phase) and (b) calibrated capacitance curve compared to an analytical model. Single tip and cantilever contributions are also indicated.

The presence of $PtSe_2$ with non-zero electrical conductivity explains the Re(Y) contrast from 8 μm to 10 μm in the results of Fig. 5.4. In fact, the conductive nature of $PtSe_2$ generates the conductance G contribution in the probe-sample equivalent circuit model of Fig. 4.6. Instead, in points with no sample, the Re(Y) approaches zero because only the air separates the tip and the metal substrate (non-contact mode), and in this case G is negligible. On the other hand, the tip vertical movement generates the negative Im(Y)/ω contrast of $PtSe_2$, because the tip-ground distance increases with the presence of the sample.

2.3 Local conductivity of the sample

As done in the simulation results section of the previous chapter, the $PtSe_2$ electrical conductivity is evaluated by comparing the obtained Re(Y) with the two-dimensional finite-element model of the tip-sample system. The simulation provides similar curves to the ones reported in Fig. 4.6 (b,c), in which the tip has nominal parameters from the tip manufacturer ($H = 17$ μm, half cone angle $\varphi = 10°$, tip radius $r = 25$ nm), and Fig. 5.5 depicts the computed Re(Y). The figure graphically compares the measured Re(Y) contrast of around 1-2 nS in presence of the sample with the curve obtained with simulations, providing a conductivity value in the region 10^3–10^4 S/m. The reduced sensitivity of the system for high values of σ generates the large confidence of σ, as seen from the Re(Y) curve flattening, magnified in the inset of Fig. 5.5.

In principle, increasing the excitation frequency reduces the confidence interval, because the Re(Y) curve peak of Fig. 5.5 shifts towards higher σ values. However,

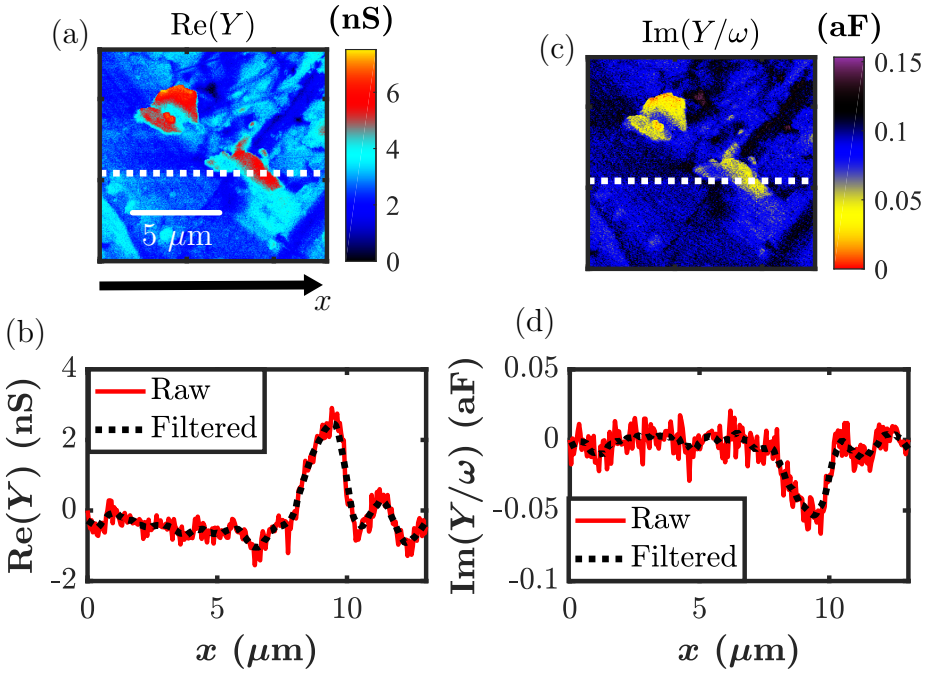

Figure 5.4

Calibrated (a) Re(Y) and (c) Im(Y)/ω image of the Platinum Diselenide flakes of Fig. 5.2. Single line contrast of (b) Re(Y) and (d) Im(Y)/ω across the middle of the image; dotted curves indicate filtered quantities to reduce noise. The image contrast is taken with respect to a point with no sample.

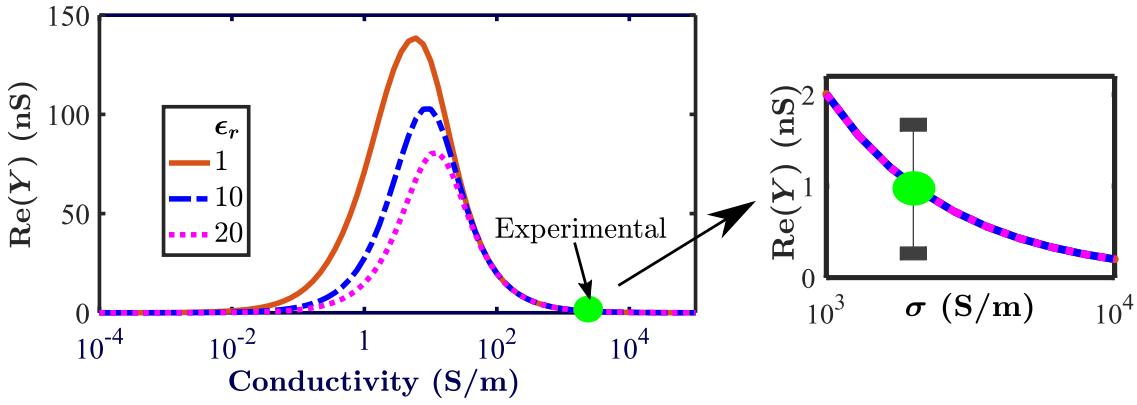

Figure 5.5

The simulated real part of the tip-sample admittance Re(Y) at 4.7 GHz compared to the experimental result on the Platinum Diselenide sample of Fig. 5.4 (b). In the simulation, the tip has height $H = 17$ μm, half cone angle $\varphi = 10°$, and tip radius $r = 25$ nm. Inset: magnification of Re(Y) in the sample conductivity range [10^3 S/m;10^4 S/m].

in the actual setup, to maximize the SNR the bandwidth limits the operating frequency at about 4.7 GHz, as already seen from Fig. 5.1. As pointed out previously, the Re(Y) and Im(Y) are independent of ϵ_r if σ is sufficiently high. The amount

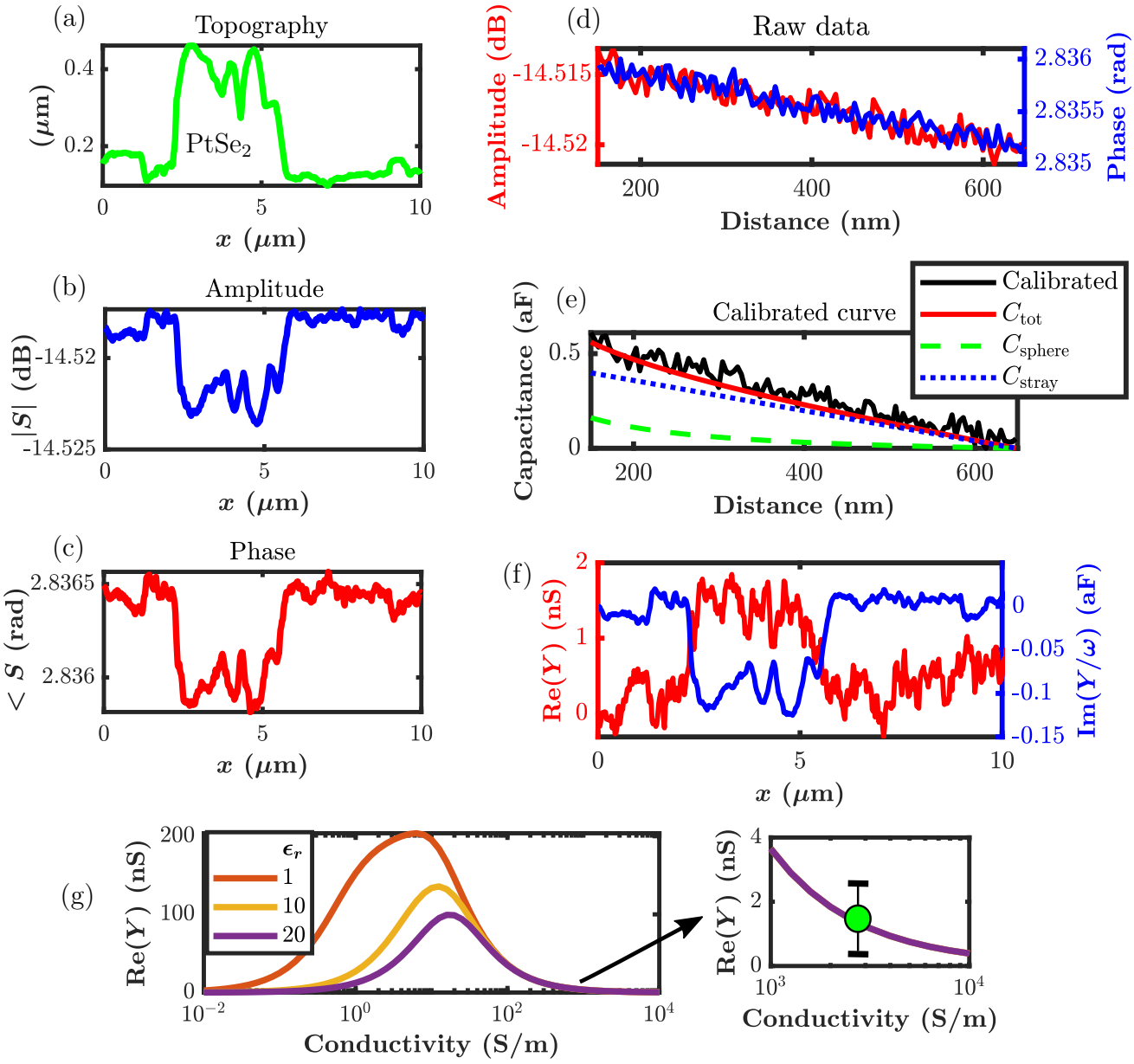

Figure 5.6

(a) Topography cross-section of a $PtSe_2$ flake and corresponding high-frequency data in terms of (b) amplitude and (c) phase of S_{11} at 8.5 GHz. (d) Raw S_{11} approach curve on top of the bare gold line at 8.5 GHz and (e) calibrated capacitance curve compared with the analytical model. (f) Calibrated $\mathrm{Re}(Y)$ and $\mathrm{Im}(Y)/\omega$ cross-sections of the $PtSe_2$ flake. The image contrast is taken with respect to a point with no sample. (g) Simulated $\mathrm{Re}(Y)$ with the same simulation parameters as Fig. 5.5 but at the frequency of 8.5 GHz. Inset: magnification of Re(Y) in the sample conductivity range [10^3 S/m;10^4 S/m] compared to the experimental result of $\mathrm{Re}(Y)$ calibration in Fig. (f), indicating a 1-2 nS contrast in presence of $PtSe_2$.

of sample conductivity required to reach this non-sensitive region depends on the tip-sample geometry as well as the excitation frequency. With the selected tip-sample

parameters, this phenomenon appears around σ =100 S/m at 4.7 GHz, like that of Fig. 4.6 (b,c) and occurs in regions of samples with semiconductor properties. Thus, the sample dielectric properties are indistinguishable beyond this region.

2.4 Reflection mode and calibration

Like in transmission mode, reflection measurements allow quantifying the sample conductivity. Measured reflection data are reported in Fig. 5.6, highlighting a cross-section of the $PtSe_2$ sample topography and the recorded S_{11} (amplitude and phase) at 8.5 GHz. Fig. 5.6 shows the approach curve acquired in a position corresponding to the bare gold line and used to calibrate the data by means of the protocol described in Sec. 4.1 for the reflection case. The curve is converted to a capacitance curve depicted in Fig. 5.6 (e) in good accordance with the analytical model, with the same fitting parameters used in the transmission calibration. Fig. 5.6 (f) represents the calibrated cross-section profiles of the $\mathrm{Re}(Y)$ and $\mathrm{Im}(Y)/\omega$, with a positive contrast for the $\mathrm{Re}(Y)$ and negative for $\mathrm{Im}(Y)/\omega$ in presence of $PtSe_2$, as observed in Fig. 5.4 (d,f). The $\mathrm{Re}(Y)$ contrast in presence of $PtSe_2$ indicates a value around 1-2 nS. This value is compared to the simulation results of the tip-sample admittance at a frequency of 8.5 GHz, again indicating a sample conductivity of around 10^3 – 10^4 S/m in accordance with transmission measurements.

Section 3

Electrical properties of Jurkat cells

This section reports the characterization of Jurkat cells (human lymphocyte cells) by using the iSMM. Consequently, iSMM is here employed and tested in the context of non-invasive and biocompatible microscopy for quantitative sample characterization. In the following sections, reflection data are obtained and calibrated to evaluate the local complex admittance of a single Jurkat cell. Then, the dielectric constant of a Jurkat cell is obtained with an existing analytical model.

3.1 Imaging results

Jurkat cells were prepared following the method already described in Sec. 3.1 of the previous chapter and deposited on the iSMM sample holder. Fig. 5.7 shows the AFM topography and the simultaneously recorded raw iSMM S_{11} images at 4 GHz of a single Jurkat cell. Results are shown in terms of amplitude, phase, real, and imaginary part of the reflection coefficient. Fig. 5.7 (b) shows the topography section

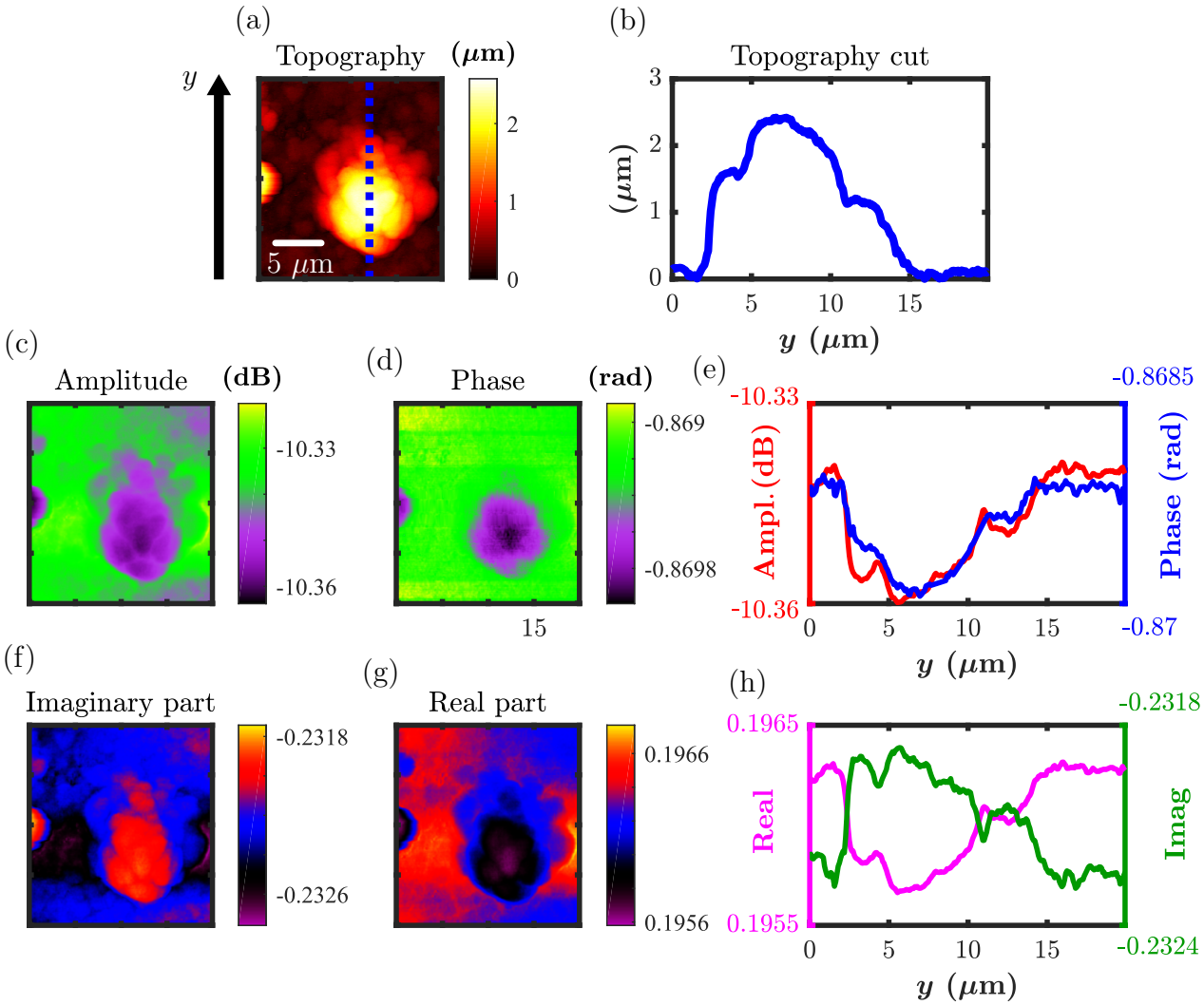

Figure 5.7

(a) Atomic Force Microscopy topography of a Jurkat cell. Yellow regions indicate the presence of the cell, red-black areas correspond to the gold line. (b) Topography cross-section corresponding to the blue dotted line shown in panel (a). Simultaneously acquired high-frequency data in terms of (c) amplitude, (d) phase, (f) imaginary part, and (g) real part based on S_{11} at 4 GHz. Profiles are shown in Fig. (e) and (h) along the same cross-section as (b).

crossing the center of the cell, indicating the presence of the sample between y = 2 μm and y = 16 μm. A good contrast is observed in S_{11} images between regions with and without sample at the selected frequency. Single line profiles for the acquired S_{11} are also shown in Fig. 5.7 (e,h). It can be seen (mostly from single line graphs) that the iSMM images reveal additional features beyond the sample topography. These characteristics are related to the superficial and sub-surface variation of electrical properties.

Despite the image quality is good, a certain number of sample details are likely

missing in the high-frequency data. This is due to the large size of the analysed sample, and in particular, it is expected iSMM to reduce resolution for thick samples. By shrinking the scanned area over a thinner part of the sample, a higher number of sample details would be visible. However, our aim is to characterize the cell entirely, thus a large scan area was preferred. To quantitatively interpret SMM data, raw images are calibrated throughout the reflection mode calibration already described in Sec. 4; the obtained quantities are used to extract intrinsic sample parameters.

3.2 Local admittance of the cell

S_{11} images were calibrated following the algorithm described in [49]. The calibration procedure consists of measuring an S_{11} approach curve on bare gold without any sample, shown in Fig. 5.8 (a) in terms of amplitude and phase. The curve is then converted to a capacitance approach curve depicted in Fig. 5.8 (b). Note that in this case, the resulting calibrated admittance is purely capacitive because the tip and metal plane are separated by air only.

The capacitance approach curve agrees with the analytical model of a sphere on top of a ground plane [95] confirming the accuracy of the calibration. Fig. 5.9 (a,b) shows the calibrated admittance real and imaginary part (divided by angular frequency) of the Jurkat cell. The line contrast across the middle of Fig. 5.9 (a,b) is depicted in Fig. 5.9 (c,d) along the y-direction. Differences are taken with respect to a spatial point in which no sample is present. The $\mathrm{Re}(Y)$ contrast from 2 μm to 16 μm is explained by the presence of the cell with non-zero conductive properties. In fact, the sample conductivity provokes the increase of $\mathrm{Re}(Y)$ w.r.t. points where the sample is not present and in which $\mathrm{Re}(Y) = 0$. On the other hand, the negative $\mathrm{Im}(Y)/\omega$ contrast on the cell is due to the tip vertical movement, increasing the tip-metal substrate distance in presence of the sample (topography crosstalk).

The absolute calibrated values reported in Fig. 5.9 depend not only on the electrical properties of the sample but also on the probe geometry, especially on the effective tip radius r. The value of r may differ from the nominal geometrical radius being an effective parameter, espetially in contact mode. In the present case, the effective radius selected for calibration is 620 nm. This value is obtained by measuring an Electrostatic Force Microscopy (EFM) [101] approach curve on a conductive surface [40]. The force curve is then converted in $\mathrm{d}C/\mathrm{d}z$ curve shown in Fig. 5.8 (c), in which C indicates the tip-metal substrate capacitance and z is the tip-ground separation. The radius is estimated by fitting the measured data with the

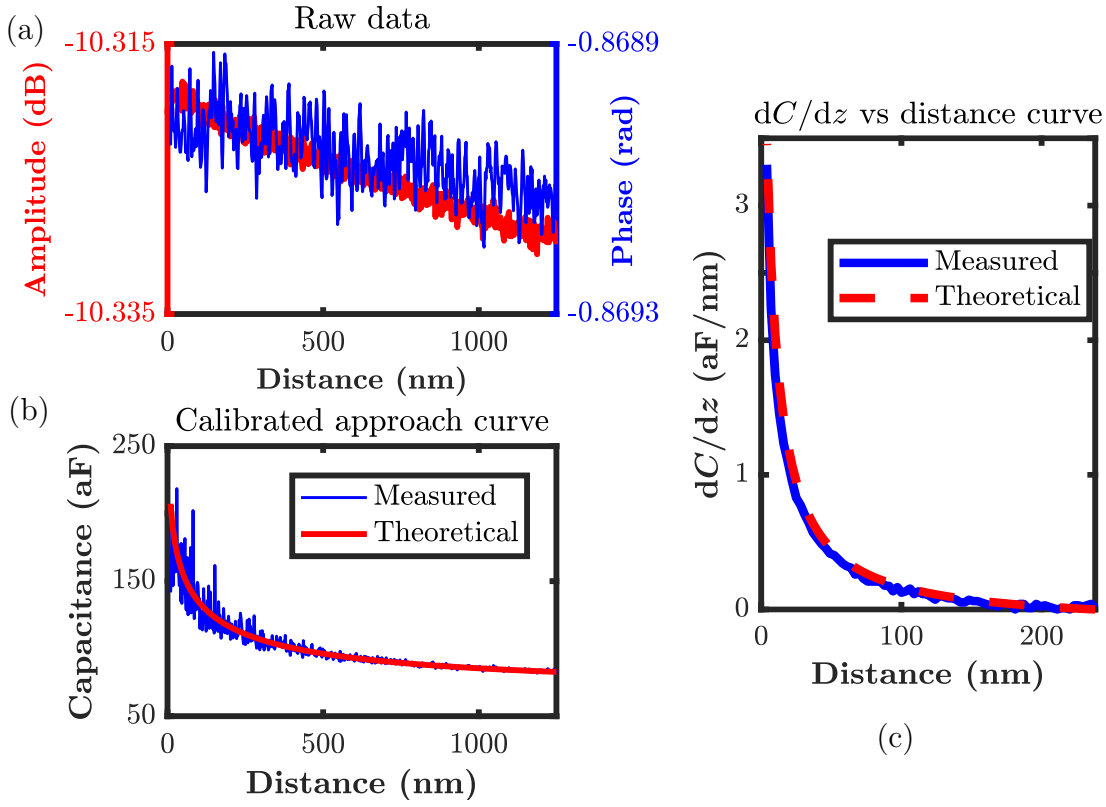

Figure 5.8

(a) Raw approach curve based on S_{11} at 4 GHz (amplitude and phase). (b) Calibrated capacitance curve compared to the analytical model of a sphere on top of a conductive plane [95]. (c) Electrostatic Force Microscopy $\mathrm{d}C/\mathrm{d}z$ curve where C indicates the tip to ground capacitance and z is the distance, compared to the analytical model. The EFM was conducted with an applied voltage of $V = 3$ V at the frequency $f = 1.5$ kHz.

analytical model of the capacitance between the point-ball tip and the conductive reference plane [95].

3.3 Local dielectric constant

Intrinsic sample electrical parameters are derived from the calibrated $\mathrm{Re}(Y)$ and $\mathrm{Im}(Y)/\omega$. In particular, the local dielectric constant is evaluated from $\mathrm{Im}(Y)/\omega$ by properly correcting the effect of topography. The topography crosstalk contribution C_{cross} is again defined as the capacitance between the tip and the ground when their distance corresponds to the sample height. The Jurkat cell dielectric constant can be derived from the difference between the calibrated $\mathrm{Im}(Y)/\omega$ and the topography crosstalk contribution C_{cross} by Eq. 4.12. Fig. 5.10 shows the obtained ϵ_{R} map, indicating an almost homogeneous dielectric constant of around $\epsilon_{\mathrm{r}} = 2.6 \pm 0.3$ in the correspondence of the cell. The estimated nominal value is in general agreement with

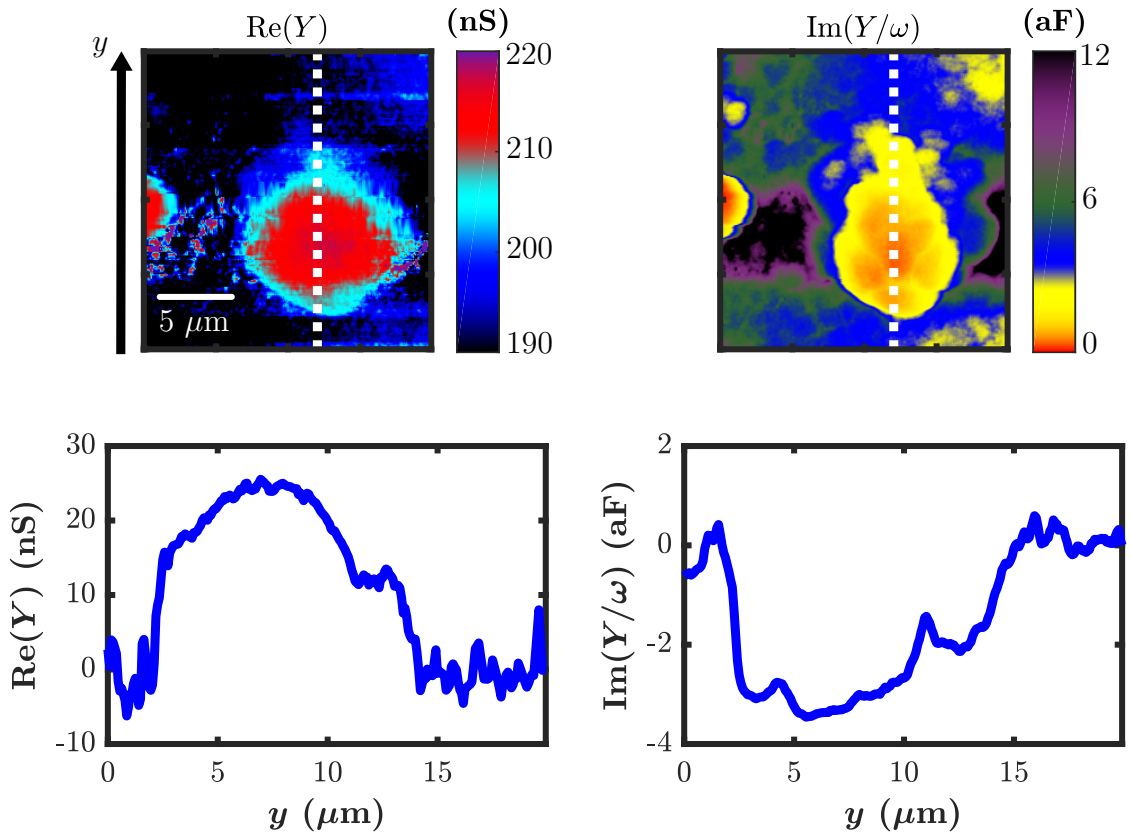

Figure 5.9

Calibrated real part Re(Y) (a) and imaginary part Im(Y)/ω (b) image of the Jurkat cell admittance. The single line contrast for Re(Y) and Im(Y)/ω are respectively shown in Fig. (c) and (d). The contrast is taken with respect to a point with no sample.

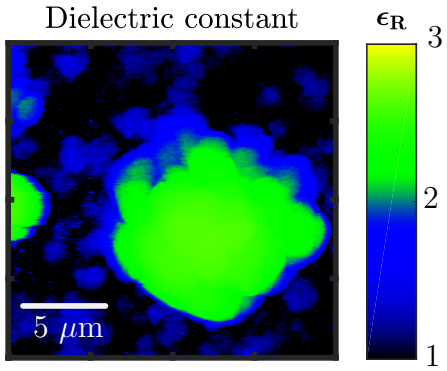

Figure 5.10

Dielectric constant map of the single Jurkat cell. The cell shows homogeneous dielectric properties, indicating a dielectric constant of around 2.6 ± 0.3 nearby its centre.

previous results obtained for dried L6 cells using conventional SMM techniques [25].

Section 4

Conclusion

In this chapter, the so-called inverted Scanning Microwave Microscope (iSMM) characterizes the conductive properties of some layers of $PtSe_2$ throughout transmission and reflection measurements. The iSMM measured an electrical conductivity of $10^3 - 10^4$ S/m, proving the semi-metal behaviour of the sample. Moreover, the microwave imaging and characterization of a single dried Jurkat cell are reported. The measured reflection data show good sensitivity and quality for the sample imaging and enabled us to estimate the complex local admittance of the cell. Finally, the dielectric constant of the sample is mapped and shown to be around 2.6 ± 0.3 and homogeneous along the cell surface. Future iSMM design could take the advantage of an optimized bandwidth to improve the system sensitivity and reduce the confidence interval of the measurement.

General Conclusion

In our work, first we described a fast and effective procedure for the rapid visualization of non-topographic sample properties (such as electromagnetic properties) in real-time in Scanning Microwave Microscopy (SMM). Hypersensitivity to topography may be problematic, masking data variations due to chemical, electrical and magnetic properties of the material. In a few steps, the protocol cancels the effect of topography and retrieves material related variations of the data. The procedure has potential applications in the study of surfaces with high roughness: here topographic contributions may dominate the captured data, and other sample properties could be mostly undetectable without any correction.

Furthermore, we have invented, experimentally demonstrated, and modelled a new microscope configuration called the inverted Scanning Microwave Microscope to image and characterize samples down to the nanometre scale. The technique is low-invasive, broadband, highly sensitive, and can be easily made biocompatible. With this tool, we imaged different biological structures, including a live cell in saline solution and we measured the electrical conductivity of some layers of Platinum Diselenide ($PtSe_2$), proving the semi-metal behaviour of the material. Moreover, we mapped the dielectric constant of a single Jurkat cell, shown to be around 2.6 $\pm$ 0.3 and homogeneous along the cell surface. Future iSMM configuration will have an optimized design, including improved bandwidth and sensitivity: this could ameliorate the tomographic capabilities of the tool and reduce the confidence interval of measurements.

Appendices

Appendix A

Brief Review of Microwave Networks Representation

Measuring voltages or currents at microwave frequencies is not always possible because this requires a clear defined terminal pair to perform the measurement. For transverse electromagnetic (TEM)-type lines, such as microstrip line, stripline, or coaxial cable, a terminal may be available, but does not strictly exist for non-TEM lines, such as rectangular or circular waveguides [11]. Moreover, direct measurements at microwave frequencies involve the magnitude and phase of a travelling wave in a given direction or of a standing wave. Therefore, equivalent voltages and currents, and consequently impedance and admittance matrices, become an abstraction when referring to high-frequency networks.

The scattering matrix gives a more direct representation according to the ideas of the incident, reflected, and transmitted waves, such as in real measurements, and it relates the waves incident on the ports to those reflected from the ports. Like the impedance or admittance matrix for an N-port network, the scattering matrix provides a complete description of the network as seen at its N ports. While the impedance and admittance matrices relate the total voltages and currents at the ports, the scattering matrix relates the voltage waves incident on the ports to those reflected from the ports.

Considering a N-port network, in which V_{n}^{+} indicates the amplitude of the voltage wave incident on port n and V_{n}^{-} is the amplitude of the voltage wave reflected from

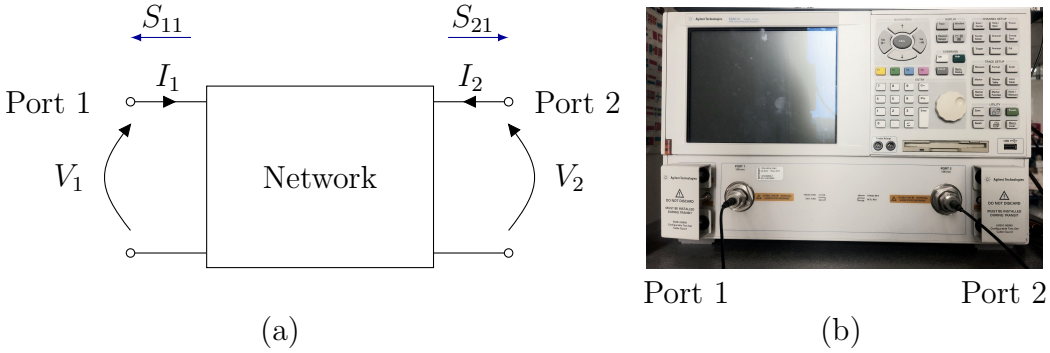

Figure A.1

(a) A two-port microwave network with an indication of input and output voltage and current (V_1, I_1 and V_2, I_2). Reflection in port one (S_{11}) and transmission from port one to port two (S_{21}) are also indicated. (b) The Agilent E8361A Vector Network Analyzer that measures the scattering parameters of RF and microwave networks from 10 MHz to 67 GHz.

port n, the scattering matrix $\overline{\overline{\boldsymbol{S}}}$ is defined as

$$\begin{bmatrix} V_1^- \\ \vdots \\ V_N^- \end{bmatrix} = \begin{bmatrix} S_{11} & \dots & S_{1N} \\ \vdots & \ddots & \vdots \\ S_{N1} & \dots & S_{NN} \end{bmatrix} \begin{bmatrix} V_1^+ \\ \vdots \\ V_N^+ \end{bmatrix} \tag{A.1}$$

or simply $\boldsymbol{V}^- = \overline{\overline{\boldsymbol{S}}}\boldsymbol{V}^+$. The {i,j}-th element of the matrix is computed as

$$S_{\mathrm{ij}} = \left.\frac{V_\mathrm{i}^-}{V_\mathrm{j}^+}\right|_{V_\mathrm{k}^+=0 \text{ for } \mathrm{k}\neq\mathrm{j}} \tag{A.2}$$

S_{ij} is found by driving port j with an incident wave of voltage V_j^+ and measuring the reflected wave amplitude V_i^- from port i . The incident waves on all ports except the j-th port are zero; this means that all the other ports must be terminated in matched loads to avoid reflections. Therefore, S_{ii} indicates the reflection coefficient seen into the port i when all other ports are terminated in matched loads, and S_{ij} refers to the transmission coefficient from port j to port i when all other ports are terminated in matched loads. Fig. A.1 (a) shows an example of a two-port microwave network with an indication of the reflection S_{11} at the first port and transmission S_{21} from the first to the second port.

The scattering parameters of microwave and radio-frequency networks can be measured with a Vector Network Analyzer (VNA), such as the Agilent E8361A VNA

represented in Fig. A.1 (b), which is a two-channel microwave receiver designed to process the magnitude and phase of the transmitted and reflected waves from the connected network.

Many microwave networks, such as the inverted Scanning Microwave Microscope described in Ch. 4, consist of a cascade connection of two or more two-port networks. Here it is convenient to define a 2×2 transmission, or ABCD, matrix, for each two-port network. The ABCD matrix is defined for a two-port network in terms of the total voltages and currents as:

$$\begin{cases} V_1 = AV_2 + BI_2 \\ I_1 = CV_2 + DI_2 \end{cases} \tag{A.3}$$

or in matrix form as

$$\begin{bmatrix} V_1 \\ I_1 \end{bmatrix} = \begin{bmatrix} A & B \\ C & D \end{bmatrix} = \begin{bmatrix} V_2 \\ I_2 \end{bmatrix}. \tag{A.4}$$

With respect to Fig. A.1 (a), I_1 remains the current flowing into port 1, but we now consider I_2 as the current flowing out of port 2 (opposite direction of the I_2 indicated in the figure); thus, in a cascade network I_2 will be the same current that flows into the adjacent network. Following this definition, the ABCD matrix of the cascade connection of two or more two-port networks is the matrix product of the ABCD matrices of the individual two-ports (preserving the multiplication order of the matrix coherent with the order in which the networks are arranged, since matrix multiplication is not, in general, commutative).

List of Publications

1. M. Farina, J. C. M. Hwang, A. Di Donato, E. Pavoni, G. Fabi, A. Morini, F. Piacenza, E. Di Filippo, and T. Pietrangelo, "*Imaging of sub-cellular structures and organelles by an STM-assisted scanning microwave microscope at mm-waves,*" in IEEE MTT-S Int. Microwave Symp. (IMS), Philadelphia, PA, USA, pp. 111-114, Jun. 2018.

2. M. Farina, X. Jin, G. Fabi, E. Pavoni, A. di Donato, D. Mencarelli, A. Morini, F. Piacenza, R. Al Hadi, Y. Zhao, T. Pietrangelo, X. Cheng, Y. Ning, and J. C. M. Hwang, "*Inverted scanning microwave microscope for in vitro imaging and characterization of biological cells,*" Appl. Phys. Lett., vol. 114, no. 9, pp. 093703-1-093703-3, Mar. 2019.

3. X. Jin, M. Farina, X. Wang, G. Fabi, X. Cheng, and J. C. M. Hwang, "*Broadband scanning microwave microscopy of a biological cell with unprecedented image quality and signal-to-noise ratio,*" in IEEE MTT-S Int. Microwave Symp. (IMS), Boston, MA, USA, Jun. 2019, pp. 1-3.

4. G. Fabi, X. Jin, J. C. M. Hwang, C. H. Joseph, E. Pavoni, L. Li, K. Xiong, Y. Ning, D. Mencarelli, A. di Donato, A. Morini, Y. Zhao, R. Al Hadi, and M. Farina, "*Inverted scanning microwave microscopy for nanometer scale imaging and characterization of Platinum Diselenide,*" in IEEE MTT-S Int. Microwave Symp. (IMS), Boston, MA, USA, Jun. 2019, pp. 1-3.

5. X. Jin, M. Farina, X. Wang, G. Fabi, X. Cheng, and J. C. M. Hwang, "*Quantitative Scanning Microwave Microscopy of the Evolution of a Live Biological Cell in a Physiological Buffer,*" IEEE Transactions on Microwave Theory and Techniques, Oct. 2019.

6. E. Pavoni, R. Yivlialin, C. Hardly Joseph, G. Fabi, D. Mencarelli, L. Pierantoni, G. Bussetti, and M. Farina, "*Blisters on graphite surface: a scanning microwave microscopy investigation,*" RSC Advances, vol. 9, pp. 23156-23160, 2019.

7. G. Fabi, C. H. Joseph, X. Jin, T. Pietrangelo, X. Cheng, J. C. M. Hwang, and M. Farina "*Electrical Properties of Jurkat cells: an inverted scanning microwave microscope study,*", in IEEE MTT-S Int. Microwave Symp. (IMS), Los Angeles, CA, USA, Aug. 2020.

8. X. Wang, K. Xiong, L. Li, J. C. M. Hwang, X. Jin, G. Fabi, M. Farina, O. Hartwig, M. Prechtl, G. S. Duesberg, A. Goritz, M. Wietstruck, and M. Kaynak, "*Quantitative Scanning Microwave Microscopy of Few-layer Platinum Diselenide,*" European Microwave Week 2020, Utrecht, Jan. 2021.

9. G. Fabi, X. Jin, E. Pavoni, C. H. Joseph, A. Di Donato, D. Mencarelli, X. Wang, R. Al Hadi, A. Morini, J. C. M. Hwang, and M. Farina,'*Quantitative characterization of Platinum Diselenide electrical conductivity with an Inverted Scanning Microwave Microscope,*" IEEE Transactions on Microwave Theory and Techniques, submitted, Nov. 2020.

10. G. Fabi, C.H. Joseph, E. Pavoni, X. Wang, R. Al Hadi, J. C. M. Hwang, A. Morini, and M. Farina, "*Real-time removal of topographic artefacts in Scanning Microwave Microscopy,*" IEEE Transactions on Microwave Theory and Techniques, accepted for publication, Jan. 2021.

11. A. Di Donato, G. Fabi, D. Mencarelli, L. Pierantoni, A. Morini, and M. Farina, "*Heterodyne Synthetic Optical Holography,*" J. Opt. Soc. Am. A, vol. 38, no. 3, pp. 378-386, Jan. 2021.

Bibliography

[1] G. Binnig, H. Rohrer, C. Gerber, and E. Weibel, "*Surface studies by scanning tunneling microscopy,*" Physical Review Letters, vol. 49, no. 1, pp. 57–61, 1982.

[2] B. Voigtländer, "*Scanning Probe Microscopy – Atomic Force Microscopy and Scanning Tunneling Microscopy,*" Springer-Verlag, Berlin, 2016.

[3] G. Binnig, C. F. Quate, and C. Gerber. "*Atomic Force Microscope,*" Physical Review Letters, vol. 56, no. 9, pp. 930-933, 1986.

[4] E. H. Synge, "*A Suggested Method for Extending Microscopic Resolution into the Ultra- microscopic Region,*" Philosophical Magazine Series 7, vol. 6, no. 35, p. 356, 1928.

[5] C. Bryant C. and J. Gunn, "*Noncontact Technique for the Local Measurement of Semiconductor Resistivity,*" Review of Scientific Instruments, vol. 36, no. 11, pp. 1614–1617, 1965.

[6] E. A. Ash and G. Nicholls, "*Super-resolution aperture scanning microscope,*" Nature, vol. 237, no. 5357, pp. 510-512, 1972.

[7] The Keysight Technologies website. [Online] (2020). Available: http://literature.cdn.keysight.com/litweb/pdf/5989-8881EN.pdf.

[8] J. Lee, C. J. Long, H. Yang, X.- D. Xiang, and I. Takeuchi, "*Atomic Resolution Imaging at 2.5 GHz Using Near- Field Microwave Microscopy,*" Applied Physics Letters, vol. 97, no. 18, p. 183111, Nov. 2010.

[9] C. P. Vlahacos, R. C. Black, S. M. Anlage, A. Amar, and F. C. Wellstood, "*Near-field scanning microwave microscope with 100 μm resolution,*" Applied Physics Letters, vol. 69, no. 21, pp. 3272-3274, 1996.

[10] S. M. Anlage, V. V. Talanov, and A. R. Schwartz, "*Principles of Near-Field Microwave Microscopy,*" in Scanning Probe Microscopy, pp. 215-253, Springer-Verlag, New York, 2007.

[11] D. M. Pozar,"*Microwave engineering,*" Fourth Edition, John Wiley & Sons, 2012.

[12] M. C. Biagi, R. Fabregas, G. Gramse, M. Van Der Hofstadt, A. Juarez, F. Kienberger, L. Fumagalli, and G. Gomila, "*Nanoscale electric permittivity of single bacterial cells at gigahertz frequencies by scanning microwave microscopy,*" ACS Nano, vol. 10, no. 1, pp. 280-288, 2016.

[13] S. S. Tuca, G. Badino, G. Gramse, E. Brinciotti, M. Kasper, Y. J. Oh, R. Zhu, C. Rankl, P. Hinterdorfer, and F. Kienberger, "*Calibrated complex impedance of CHO cells and E. Coli bacteria at GHz frequencies using scanning microwave microscopy,*" Nanotechnology, vol. 27, no. 13, p. 135702, 2016.

[14] B. J. Feenstra, C. P. Vlahacos, A. S. Thanawalla, D. E. Steinhauer, S. K. Dutta, F. C. Wellstood, and S. M. Anlage, "*Near-field scanning microwave microscopy: measuring local microwave properties and electric field distributions,*" IEEE MTT-S International Microwave Symposium Digest, Baltimore, MD, USA, vol. 2, pp. 965-968, 1998.

[15] U. Kemiktarak, T. Ndukum, K. C. Schwab, and K. L. Ekinci, "*Radio-Frequency Scanning Tunneling Microscopy,*" Nature, vol. 450, no. 7166, pp. 85–88, 2007.

[16] C. Plassard, E. Bourillot, J. Rossignol, Y. Lacroute, E. Lepleux, L. Pacheco, and E. Lesniewska, "*Detection of Defects Buried in Metallic Samples by Scanning Microwave Microscopy,*" Physical Review B, vol. 83, no. 12, p. 121409, 2011.

[17] G. Gramse, A. Kölker, T. Lim, T. J. Stock, H. Solanki, S. R. Schofield, E. Brinciotti, G. Aeppli, F. Kienberger, and N. J. Curson, "*Nondestructive imaging of atomically thin nanostructures buried in silicon,*" Science Advances, vol. 3, no. 6, p. 1602586, 2017.

[18] E. Brinciotti, G. Gramse, S. Hommel, T. Schweinboeck, A. Altes, M. A. Fenner, J. Smoliner, M. Kasper, G. Badino, S. S. Tuca, and F. Kienberger, "*Probing resistivity and doping concentration of semiconductors at the nanoscale using scanning microwave microscopy,*" Nanoscale, vol. 7, no. 35, pp. 14715–14722, 2015.

[19] E. Brinciotti, G. Campagnaro, G. Badino, M. Kasper, G. Gramse, S. S. Tuca, J. Smoliner, T. Schweinboeck, S. Hommel, and F. Kienberger, "*Frequency Analysis of Dopant Profiling and Capacitance Spectroscopy Using Scanning Microwave Microscopy,*" IEEE Transactions on Nanotechnology, vol. 16, no. 1, pp. 75-82, Jan. 2017.

[20] E. Brinciotti, G. Badino, M. Knaipp, G. Gramse, J. Smoliner, and F. Kienberger, "*Calibrated Nanoscale Dopant Profiling and Capacitance of a High-Voltage Lateral MOS Transistor at 20 GHz Using Scanning Microwave Microscopy,*" IEEE Transactions on Nanotechnology, vol. 16, no. 2, pp. 245-252, March 2017.

[21] X. Jin, K. Xiong, R. Marstell, N. C. Strandwitz, J. C. M. Hwang, M. Farina, A. Göritz, M. Wietstruck, and M. Kaynak, "*Scanning microwave microscopy of buried CMOS interconnect lines with nanometer resolution,*" Int. J. Microw. Wireless Technol., vol. 10, no. 5–6, pp. 556–561, Jun. 2018.

[22] E. Pavoni, R. Yivlialin, C.H. Joseph, G. Fabi, D. Mencarelli, L. Pierantoni, G. Bussetti, and M. Farina, "*Blisters on graphite surface: a scanning microwave microscopy investigation,*" RSC Advances, vol. 9, no. 40, pp. 23156–23160, 2019.

[23] M. Farina, F. Piacenza, F. De Angelis, D. Mencarelli, A. Morini, G. Venanzoni, T. Pietrangelo, M. Malavolta, A. Basso, M. Provinciali, J.C.M. Hwang, X. Jin, and A. Di Donato, "*Investigation of fullerene exposure of breast cancer cells by time-gated scanning microwave microscopy,*" IEEE Transactions on Microwave Theory and Techniques, vol. 64, no. 12, pp. 4823-4831, Dec. 2016.

[24] M. Farina, X. Jin, G. Fabi, E. Pavoni, A. Di Donato, D. Mencarelli, F. Piacenza, R. Al Hadi, Y. Zhao, Y. Ning, T. Pietrangelo, X. Cheng, and J.C.M. Hwang, "*Inverted scanning microwave microscope for in vitro imaging and characterization of biological cells,*" Applied Physics Letters, vol. 114, no. 9, p. 093703, 2019.

[25] X. Jin, M. Farina, X. Wang, G. Fabi, X. Cheng, and J.C.M. Hwang, "*Quantitative Scanning Microwave Microscopy of the Evolution of a Live Biological Cell in a Physiological Buffer,*" IEEE Transactions on Microwave Theory and Techniques, vol. 67, no. 12, pp. 1-8, Oct. 2019.

[26] X. Jin, M. Farina, X. Wang, G. Fabi, X. Cheng, and J. C. M. Hwang, "*Broadband scanning microwave microscopy of a biological cell with unprecedented*

image quality and signal-to-noise ratio," IEEE MTT-S International Microwave Symposium Digest, pp. 216–219, Jun. 2019.

[27] J. Li, Z. Nemati, K. Haddadi, D. C. Wallace, and P. J. Burke, "*Scanning microwave microscopy of vital mitochondria in respiration buffer,*" IEEE MTT-S International Microwave Symposium Digest, pp. 115–118, Feb. 2018.

[28] M. Farina, D. Mencarelli, A. Morini, L. Pierantoni, X. Jin, and J. C. M. Hwang, "*Developments of microwave microscopy for application to biological samples,*" Proc. Int. Conf. Manipulation, Autom. Robot. Small Scales (MARSS), pp. 1–5, Jul. 2017.

[29] M. Tabib-Azar, J. L. Katz, and LeClair, "*Evanescent microwaves: a novel super-resolution noncontact nondestructive imaging technique for biological applications,*" IEEE Transactions on Instrumentation and Measurement, vol. 48, no. 6, pp. 1111-1116, Dec. 1999.

[30] D. Wu and K. Lai, "*Noninvasive conductivity imaging of 2D materials and devices by microwave impedance microscopy,*" IEEE MTT-S International Microwave Symposium Digest, San Francisco, CA, pp. 1-4, 2016.

[31] P. J. d. Visser, R. Chua, J. O. Island, M. Finkel, A. J. Katan, H. Thierschmann, H. S. J. v. d. Zant, and T. M. Klapwijk, "*Spatial conductivity mapping of unprotected and capped black phosphorus using microwave microscopy,*" 2D Materials, vol. 3, no. 2, p. 021002, 2016.

[32] S. Hussain, K. Xu, S. Ye, L. Lei, X. Liu, R. Xu, L. Xie, and Z. Cheng, "*Local electrical characterization of two-dimensional materials with functional atomic force microscopy,*" Frontiers of Physics, vol. 14, no. 3, p. 33401, 2019.

[33] S. M. Anlage, C. P. Vlahacos, S. Dutta, and F. C. Wellstood, "*Scanning microwave microscopy of active superconducting microwave devices,*" IEEE Transactions on Applied Superconductivity, vol. 7, no. 2, pp.

[34] S. M. Anlage, D. E. Steinhauer, C. P. Vlahacos, B. J. Feenstra, A. S. Thanawalla, Wensheng Hu, S. K. Dutta, and F. C. Wellstood, "*Superconducting material diagnostics using a scanning near-field microwave microscope,*" IEEE Transactions on Applied Superconductivity, vol. 9, no. 2, pp. 4127-4132, June 1999.

[35] A. Tselev, P. Yu, Y. Cao, L. R. Dedon, L. W. Martin, S. V. Kalinin, and P. Maksymovych, "*Microwave a.c. conductivity of domain walls in ferroelectric thin films,*" Nature Communications, vol. 7, no. 1, p. 11630, May 2016.

[36] Y. Lu, T. Wei, F. Duewer, Y. Lu, N. Ming, P. G. Schultz, and X.-D. Xiang, "*Nondestructive Imaging of Dielectric-Constant Profiles and Ferroelectric Domains with a Scanning-Tip Microwave Near-Field Microscope,*" Science, vol. 276, no. 5321, pp. 2004-2006, 1997.

[37] A. Imtiaz and S. M. Anlage, "*A Novel STM- Assisted Microwave Microscope with Capacitance and Loss Imaging Capability,*" Ultramicroscopy, vol. 94, no. 5-6, pp. 209-216, 2003.

[38] M. Tabib-Azar and Y. Wang, "*Design and fabrication of scanning near-field microwave probes compatible with atomic force microscopy to image embedded nanostructures,*" IEEE Transactions on Microwave Theory and Techniques, vol. 52, no. 3, pp. 971-978, 2004.

[39] A. Karbassi, D. Ruf, A. D. Bettermann, C.A. Paulson, Daniel W. van der Weide, H. Tanbakuchi, and R. Stancliff, "*Quantitative scanning near-field microwave microscopy for thin film dielectric constant measurement,*" Review of Scientific Instruments, vol. 79, no. 9, p. 094706, 2008.

[40] G. Gramse, M. Kasper, L. Fumagalli, and G. Gomila, "*Calibrated complex impedance and permittivity measurements with scanning microwave microscopy,*" Nanotechnology, vol. 26, no. 14, p. 145703, 2014.

[41] A. Imtiaz, T. M. Wallis, and P. Kabos, "*Near-field scanning microwave microscopy: An emerging research tool for nanoscale metrology,*" IEEE Microwave Magazine, vol. 15, no.1, pp. 52-64, 2014.

[42] T. M. Wallis and P. Kabos, "*Measurement techniques for radio frequency nanoelectronics,*" Cambridge University Press, 2017.

[43] K. Lee, H. Melikyan, A. Babajanyan, and B. Friedman, "*Near-Field Microwave Microscopy for Nanoscience and Nanotechnology,*" in Scanning Probe Microscopy in Nanoscience and Nanotechnology 2, B. Bhushan, Ed. NanoScience and Technology, pp. 135-171, Springer: Berlin, 2011.

[44] B. T. Rosner and D. W. van der Weide, "*High-Frequency Near-Field Microscopy,*" Review of Scientific Instruments, vol. 73, no. 7, pp. 2505–2525, 2002.

[45] K. Lai, W. Kundhikanjana, M. A. Kelly, and Z.-X. Shen, "*Nanoscale microwave microscopy using shielded cantilever probes,*" Applied Nanoscience, vol. 1, pp. 13–18, 2011.

[46] K. Lai, W. Kundhikanjana, M. Kelly, and Z. X. Shen, "*Modeling and Characterization of Cantilever-Based Near-Field Scanning Microwave Impedance Microscope,*" Review of Scientific Instruments, vol. 79, no. 6, p. 063703, 2008.

[47] D. W. van der Weide, "*Localized picosecond resolution with a near-field microwave/scanning-force microscope,*" Applied Physics Letters, vol. 70, no. 6, pp. 677-679, 1997.

[48] M. C. Biagi, G. Badino, R. Fabregas, G. Gramse, L. Fumagalli, and G. Gomila, "*Direct mapping of the electric permittivity of heterogeneous non-planar thin films at gigahertz frequencies by scanning microwave microscopy,*" Physical Chemistry Chemical Physics, vol. 19, no. 5, pp. 3884-3893, 2017.

[49] M. Farina, D. Mencarelli, A. Di Donato, G. Venanzoni, and A. Morini, "*Calibration Protocol for Broadband Near-Field Microwave Microscopy,*" IEEE Transactions on Microwave Theory and Techniques, vol. 59, no. 10, pp. 2769–2776, Oct. 2011.

[50] M. Farina, A. Lucesoli, T. Pietrangelo, A. Di Donato, S. Fabiani, G. Venanzoni, D. Mencarelli, T. Rozzi, and A. Morini,"*Disentangling time in a near-field approach to scanning probe microscopy,*" Nanoscale, vol. 3, no. 9, pp. 3589–3593, Sept. 2011.

[51] T. Dargent, K. Haddadi, T. Lasri, N. Clément, D. Ducatteau, B. Legrand, H. Tanbakuchi, and D. Theron, "*An interferometric scanning microwave microscope and calibration method for sub-fF microwave measurements,*" Review of Scientific Instruments, vol. 84, no. 12, p. 12370, 2013.

[52] J. Hoffmann, M. Wollensack, M. Zeier, J. Niegemann, H. Huber, and F. Kienberger, "*A calibration algorithm for nearfield scanning microwave microscopes,*" 12th IEEE International Conference on Nanotechnology (IEEE-NANO), Birmingham, pp. 1-4, 2012.

[53] H. P. Huber, M. Moertelmaier, T. M. Wallis, C. J. Chiang, M. Hochleitner, A. Imtiaz, Y. J. Oh, K. Schilcher, M. Dieudonne, J. Smoliner, P. Hinterdorfer, S. J. Rosner, H. Tanbakuchi, P. Kabos, and F. Kienberger, "*Calibrated nanoscale*

capacitance measurements using a scanning microwave microscope," Review of Scientific Instruments, vol. 81, no. 11, p. 113701, Nov 2010.

[54] B. Knoll, F. Keilmann, A. Kramer, and R. Guckenberger, "*Contrast of microwave near-field microscopy,*" Applied Physics Letters, vol. 70, no. 20, pp. 2667-2669, 1997.

[55] The PrimeNano website. [Online] (2020). Available: https://www.primenanoinc.com/.

[56] F. T. Ulaby, E. Michielssen, and U. Ravaioli "*Fundamentals of applied electromagnetics 6e,*" Boston, Massachussetts: Prentice Hall, 2010.

[57] S. E. Miller, "*Integrated optics: An introduction,*" Bell Labs Technical Journal, vol. 48, no. 7, pp. 2059-2069, 1969.

[58] R. G. Hunsperger and R. M. A. Jurgen, "*Integrated optics: theory and technology,*" Applied Optics, vol. 31, no. 3, p. 298, 1992.

[59] G. Lifante "*Integrated photonics: fundamentals,*" J. Wiley. First edition, 2003.

[60] S. Ramo, J. R. Whinnery, and T. Van Duzer, "*Fields and waves in communication electronics,*" John Wiley & Sons, 2008.

[61] The COMSOL Multiphysics website. [Online] (2020). Available: https://www.comsol.com/.

[62] J. C. Weber, P. T. Blanchard, A. W. Sanders, J. C. Gertsch, S. M. George, S. Berweger, A. Imtiaz, K. J. Coakley, T. M. Wallis, K. A. Bertness, N. A. Sanford, P. Kabos, and V. M. Bright, "*GaN Nanowire Coated with Atomic Layer Deposition of Tungsten: A Probe for Near- Field Scanning Microwave Microscopy,*" Nanotechnology, vol. 25, no. 41, p. 415502, 2014.

[63] Y. Q. Wang, A. D. Bettermann, and D. W. van der Weide, "*Process for Scanning Near-Field Microwave Microscope Probes with Integrated Ultratall Coaxial Tips,*" Journal of Vacuum Science & Technology B: Microelectronics and Nanometer Structures Processing, Measurement, and Phenomena, vol. 25, no. 3, pp. 813-816, 2007.

[64] The Rocky Mountain Nanotechnology website. [Online] (2020). Available: https://rmnano.com/tech-data.

[65] V. V. Talanov, A. Scherz, R. L. Moreland, and A. R. Schwarz, "*A Near-Field Scanned Microwave Probe for Spatially Localized Electrical Metrology,*" Applied Physics Letters, vol. 88, no. 13, p. 134106, 2006.

[66] C. Gao and X.-D. Xiang, "*Quantitative microwave near-field microscopy of dielectric properties. Review of scientific instruments,*" Review of Scientific Instruments, 1998, vol. 69, no. 11, pp. 3846-3851, 1998.

[67] A. P. Gregory, J. F. Blackburn, K. Lees, R. N. Clarke, T. E. Hodgetts, S. M. Hanham, and N. Klein, "*A near-field scanning microwave microscope for measurement of the permittivity and loss of high-loss materials,*" 84th ARFTG Microwave Measurement Conference, Boulder, CO, pp. 1-8, 2014.

[68] J. Kim, H. Kim, M. Kim, B. Friedman, and K. Lee, "*Near-Field Scanning Microwave Microscope Using a Dielectric Resonator,*" AIP Conference Proceedings, vol. 657, no. 1, pp. 456-461, 2003.

[69] A. Imtiaz, T. M. Wallis, S.- H. Lim, H. Tanbakuchi, H.-P. Huber, A. Hornung, P. Hinterdorfer, J. Smoliner, F. Kienberger, and P. Kabos, "*Frequency-Selective Contrast on Variably Doped p- type Silicon with a Scanning Microwave Microscope,*" Journal of Applied Physics, vol. 111, no. 9, pp. 093727, 2012.

[70] A. L. Lereu, A. Passian, and Ph. Dumas, "*Near field optical microscopy: a brief review,*" International Journal of Nanotechnology (IJNT), vol. 9, vol. 3-7, pp. 488-501, 2012.

[71] G. Ghione, "*Semiconductor devices for high-speed optoelectronics,*" Cambridge University Press, 2009.

[72] O. Manasreh, "*Semiconductor Heterojunctions and Nanostructures,*" New York: McGraw-Hill, 2005.

[73] G. Ghione, "*Elettronica delle microonde,*" Otto editore, 2002.

[74] G. Ghione, "*Dispositivi per la Microelettronica,*" McGraw-Hill libri Italia, 1998.

[75] G. Ghione and M. Pirola, "*Microwave electronics,*" Cambridge University Press, 2017.

[76] G. Gramse, E. Brinciotti, A. Lucibello, S. B. Patil, M. Kasper, C. Rankl, R. Giridharagopal, P. Hinterdorfer, R. Marcelli, and F. Kienberger. "*Quantitative sub-surface and non-contact imaging using scanning microwave microscopy,*" Nanotechnology, vol. 26, no. 13, p. 135701, 2015.

[77] I. Giaever, "*Energy gap in superconductors measured by electron tunneling,*" Physical Review Letters, vol. 5, no. 4, pp. 147–148, 1960.

[78] E. Schrödinger, "*An undulatory theory of the mechanics of atoms and molecules,*" Physical review, vol. 28, no. 6, p. 1049, 1926.

[79] S. M. Salapaka and M. V. Salapaka, "*Scanning probe microscopy,*" IEEE control systems, vol. 28, no. 2, pp. 65-83, 2008.

[80] B. Bhushan and O. Marti, "*Scanning probe microscopy – principle of operation, instrumentation, and probes,*" Springer Handbook of Nanotechnology, pp. 573-617, Springer, Berlin, Heidelberg, 2010.

[81] V. L. Mironov, "*Fundamentals of scanning probe microscopy,*" Institute for physics of microstructures, The Russian Academy of Sciences, 2014.

[82] M. Farina, J. C. M. Hwang, A. Di Donato, E. Pavoni, G. Fabi, A. Morini, F. Piacenza, E. Di Filippo, and T. Pietrangelo, "*Imaging of sub-cellular structures and organelles by an STM-assisted Scanning Microwave Microscope at mm-Waves,*" IEEE MTT-S International Microwave Symposium Digest, Philadelphia (PA), pp. 111-114, 2018.

[83] P. A. Tipler and G. Mosca, "*Physics for scientists and engineers,*" Macmillan, 2007.

[84] D. Halliday, R. Resnick, and J. Walker, "*Fundamentals of Physics,*" John Wiley & Sons, 10th edition, 2013.

[85] E. Meyer, H. J. Hug, and R. Bennewitz, "*Scanning Probe Microscopy. The lab on a tip,*" Heidelberg, Germany: Springer, 2004.

[86] The NT-MDT Spectrum Instruments website. [Online] (2020). Available: https://www.ntmdt-si.com/.

[87] K. J. Coakley, S. Berweger, T. M. Wallis, and P. Kabos, "*Disentangling topographic contributions to near-field scanning microwave microscopy images,*" Ultramicroscopy, vol. 197, pp. 53-64, 2019.

[88] S. M. Anlage, B. J. Feenstra, and F. E. Steinhauer, "*Disentangling sample topography and physical properties in scanning near-field microwave microscopy,*" U.S. Patent No. 6,376,836. 23 Apr. 2002.

[89] A. L. Kholkin, S. V. Kalinin, A. Roelofs, and A. Gruverman, "*Review of Ferroelectric Domain Imaging by Piezoresponse Force Microscopy,*" in Scanning Probe Microscopy: Electrical and Electromechanical Phenomena at the Nanoscale, Vol. 1, Edited by S. Kalinin, and A. Gruverman, pp. 173–214, Springer, Berlin, 2006.

[90] K. Lai, W. Kundhikanjana, H. Peng, Y. Cui, M. A. Kelly, and Z. X. Shen, "*Tapping mode microwave impedance microscopy,*" Review of Scientific Instruments, vol. 80, no. 4, p. 043707, 2009.

[91] M. Farina and J. C. M. Hwang, "*Scanning Microwave Microscopy for Biological Applications: Introducing the State of the Art and Inverted SMM,*" IEEE Microwave Magazine, vol. 21, no. 10, pp. 52-59, Oct. 2020.

[92] X. Ma, X. Du, H. Li, X. Cheng, and J. C. M. Hwang, "*Ultra-Wideband Impedance Spectroscopy of a Live Biological Cell,*" IEEE Transactions on Microwave Theory and Techniques, vol. 66, no. 8, pp. 3690-3696, Aug. 2018.

[93] A. O. Oladipo, A. Lucibello, M. Kasper, S. Lavdas, G. M. Sardi, E. Proietti, F. Kienberger, R. Marcelli, and N. C. Panoiu, "*Analysis of a transmission mode scanning microwave microscope for subsurface imaging at the nanoscale,*" Applied Physics Letters, vol. 105, no. 13, p. 133112, 2014.

[94] L. Zheng, D. Wu, X. Wu, and K. Lai, "*Visualization of Surface-Acoustic-Wave Potential by Transmission-Mode Microwave Impedance Microscopy,*" Phys. Rev. Applied, vol. 9, no. 6, p. 061002, June 2018.

[95] W. R. Smythe, "*Static and Dynamic Electricity,*" McGraw-Hill, New York, NY, USA, 1950.

[96] Y. Wang, L. Li, W. Yao, S. Song, J. T. Sun, J. Pan, X. Ren, C. Li, E. Okunishi, Y. Wang, E. Wang, Y. Shao, Y. Y. Zhang, H. Yang, E. F. Schwier, H. Iwasawa, K. Shimada, M. Taniguchi, Z. Cheng, S. Zhou, S. Du, S. J. Pennycook, S. T. Pantelides, and H. Ga, "*Monolayer $PtSe_2$, a new semiconducting transition-metal-dichalcogenide, epitaxially grown by direct selenization of Pt,*" Nano Lett., vol. 15, no. 6, pp. 4013–4018, May 2015.

[97] M. Yan, E. Wang, X. Zhou, G. Zhang, H. Zhang, K. Zhang, W. Yao, N. Lu, S. Yang, S. Wu, T. Yoshikawa, K. Miyamoto, T. Okuda, Y. Wu, P. Yu, W. Duan, and S. Zhou, "*High quality atomically thin $PtSe_2$ films grown by molecular beam epitaxy,*" 2D Mater., vol. 4, no. 4, p. 045015, Sep. 2017.

[98] Y. Zhao, J. Qiao, Z. Yu, P. Yu, K. Xu , S. P. Lau, W. Zhou, Z. Liu, X. Wang, W. Ji, and Y. Cha, "*High electron−mobility and air−stable 2D layered PtSe2 FETs,*" Adv. Mater., vol. 29, no. 5, p. 1604230, Feb. 2017.

[99] L. Li, K. Xiong, R. J. Marstell, A. Madjar, N. C. Strandwitz, J. C. M. Hwang, N. McEvoy, J. B. McManus, G. S. Duesberg, A. Goritz, M. Wietstruck, and M. Kaynak, "*Wafer−scale fabrication of recessed−channel $PtSe_2$ MOSFETs with low contact resistance and improved gate control,*" IEEE Trans. Electron Devices, vol. 65, no. 10, pp. 4102-4108, Oct. 2018.

[100] C. Yim, V. Passi, M. C. Lemme, G. S. Duesberg, C. Ó Coileáin, E. Pallecchi, D. Fadil, and N. McEvoy, "*Electrical devices from top-down structured platinum diselenide films,*" 2D Mater. Appl., vol. 2, no. 1, art. no. 5, Feb. 2018.

[101] G. Gramse, A. Dols-Perez, M. A. Edwards, L. Fumagalli, and G. Gomila, "*Nanoscale measurement of the dielectric constant of supported lipid bilayers in aqueous solutions with electrostatic force microscopy,*" Biophysical journal, vol. 104, no. 6, pp. 1257-1262, 2013.